Nonrigid Registration Methods for Multimodal Carotid Artery Imaging

Niet-rigide registratiemethoden voor multimodale beeldvorming van de halsslagader

Proefschrift

ter verkrijging van de graad van doctor aan de
Erasmus Universiteit Rotterdam
op gezag van de
rector magnificus
Prof.dr. H.A.P. Pols
en volgens besluit van het College voor Promoties.
De openbare verdediging zal plaatsvinden op
dinsdag 8 december 2015 om 13:30 uur

door

Diego Dias Bispo Carvalho

geboren te Curitiba, Brazilië

Erasmus University Rotterdam

Erasmus

Promotiecommissie

Promotor:	**Prof.dr. W.J. Niessen**
Overige leden:	**Prof.dr. ir. A.F.W. van der Steen**
	Dr. G.P. Penney
	Prof.dr. J.P.W. Pluim
Copromotor:	**Dr. ir. S. Klein**

Nonrigid registration methods for multimodal carotid artery imaging

Diego Dias Bispo Carvalho

Colophon

This book was typeset by the author using LaTeX2$_\varepsilon$. The main body of the text was set using a 10-points Computer Modern Roman font.

Cover design by the author. The graphics on the cover represent the registration of Ultrasound (US) and Magnectic Resonance Imaging (MRI) of a carotid artery. The back side shows an initial aligment of images obtained with the registration of lumen centerlines. The front side shows sections of MRI and US obtained with the combined registration of centerlines and lumen segmentations. The lumen segmentation obtained from US is highlighted in green and the lumen segmentation obtained from MRI is highlighted in red.

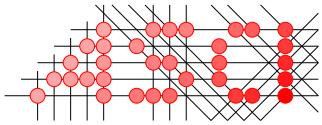

The research described in this thesis was carried out at the Erasmus MC – University Medical Center Rotterdam (Rotterdam, the Netherlands), under the auspices of the Advanced School for Computing and Imaging (ASCI): dissertation series number 342.

This research was performed within the framework of CTMM, the Center for Translational Molecular Medicine (www.ctmm.nl), project PARISk (grant 01C-202), and supported by the Netherlands Heart Foundation.

Financial support for the publication of this thesis was provided from the following organizations:
Department of Radiology of Erasmus MC University Medical Center Rotterdam.
Department of Medical Informatics of Erasmus MC University Medical Center Rotterdam.
Erasmus University Rotterdam, the Netherlands.
ASCI graduate school.

ISBN: 978-94-6299-227-6

Printed by Ridderprint BV

Contents

1 Introduction

1.1 Cardiovascular Diseases

Cardiovascular diseases rank as the major cause of death worldwide [1], and are a leading public health problem in Europe [2]. The risk factors associated with cardiovascular diseases are age, body mass, levels of serum cholesterol [3], smoking [4], and dietary habits [5]. A major percentage of cardiovascular diseases is connected with the process of atherosclerosis, which causes narrowing of the arterial lumen, as illustrated in Fig. 1.1. Atherosclerosis originates from inflammations in the arterial wall, which contribute to the formation of an atherosclerotic plaque. In the event of a plaque rupture, parts of the plaque can enter the blood stream and obstruct vessels, causing ischemic strokes or embolism, see Fig. 1.2. Plaque composition has been known to be related to the vulnerability of plaques, i.e. the risk of plaque rupture [6, 7]. Another factor connected with plaque rupture is the presence of *vasa vasorum*, i.e. intraplaque vascularization [8].
The treatment of atherosclerosis depends on the stage of the disease and the risk of plaque rupture. In the case of low plaque rupture risk, the patient can be treated with medication [9, 10] and undergoes periodical monitoring in which the atherosclerosis state [11–13] is assessed. For patients with a high risk of atherosclerotic plaque rupture, a surgical procedure is advised [14]. The risk of mortality associated with this procedure has led to high interest of the medical community in establishing accurate methods for plaque rupture risk assessment [15].

1.2 Carotid Artery Imaging

In this thesis I focus on atherosclerosis in carotid arteries. The carotid arteries are two blood vessels located at both sides of the neck. The carotid artery is composed of the Common Carotid Artery (CCA) which bifurcates in the External Carotid Artery (ECA), supplying blood to the muscles of the face, and Internal Carotid Artery (ICA), supplying blood to the brain.

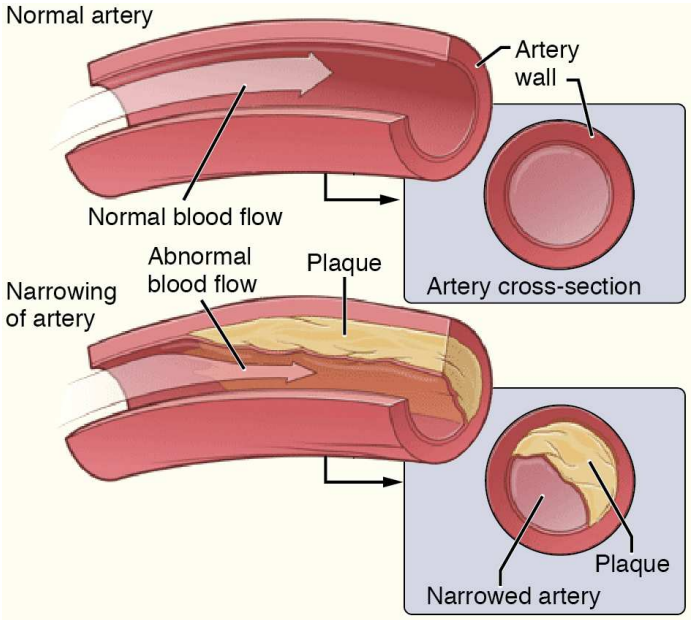

Figure 1.1: Illustration of a normal carotid artery and a carotid artery with atherosclerosis. source: Wikimedia. Author: National Heart Lung and Blood Institute (NIH)

Medical imaging modalities have proven to be valuable tools to visualize the carotid artery wall. Imaging may aid in the differentiation between stable and vulnerable plaques [16, 17]. Different imaging techniques have been employed to inspect the carotid artery and assess atherosclerosis. In this thesis we address images obtained in a non-invasive manner with Magnetic Resonance Imaging (MRI) and Ultrasound (US).

MR image intensities are related to the biophysical response of tissues to an electromagnetic pulse inside a strong magnetic field [18]. Figure 1.3b illustrates the acquisition device. MRI is suitable for visualizing the arterial wall in three dimensions (3D), which can be used to estimate the size of the plaque [19]. Moreover, in MRI it is possible to assess the carotid artery lumen, and the carotid artery plaque composition. MRI has a better differentiation of soft tissues than, e.g., CT, enabling the identification of plaque elements, such as lipid cores, fibrous caps, calcifications, normal media, and adventitia [20].

In an US examination of the carotid artery, a probe in contact with the patient's neck emits an acoustic pulse wave, see Fig. 1.3a. The pixel intensities in US images are related to the quantity of energy reflected back to the probe. When the pulse wave emitted by the probe reaches an interface between two tissues, a certain quantity of energy is reflected back [21]. Plaque vulnerability predictors can also be inspected with US, e.g. stenosis degree, plaque surface irregularity, echolucence and texture [22]. US images can be two-dimensional (2D) or 3D. US probes that generate volumetric information are composed of an array of 2D transducer elements [23]. US volumetric

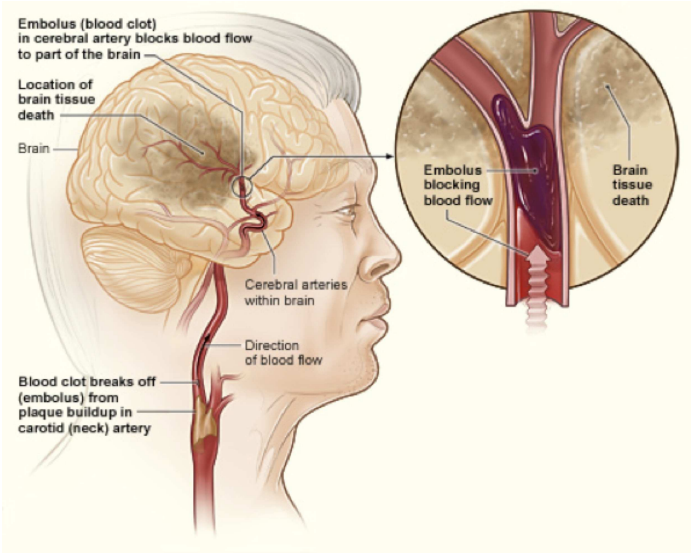

Figure 1.2: Example illustration of a cerebrovascular acident. source: Wikimedia. Author: National Heart Lung and Blood Institute (NIH)

information can also be gathered by using an external device alongside a 2D probe [23]. The probe can be manipulated by a mechanically assisted device [24], or free-hand (manipulated by a clinician) by using a tracking device attached to the probe. The tracking device provides spatial coordinates which are correlated with the images allowing volumetric reconstruction [25, 26]. Both 2D and 3D US supply valuable information about the artery, being each suitable for different applications. Whereas 3D US images tend to be used for inspecting arterial morphology and quantifying the plaque volume [27], 2D US images are being used to inspect the arterial layers of the carotid artery [28]. The study of US images across time also enables the estimation of plaque motion [29, 30], which may also be an indicator of plaque vulnerability. A novel US technique, Contrast Enhanced US (CEUS), produces images with improved visualization of the blood flow. An example CEUS image is shown in Fig. 1.6. In this modality a contrast agent injected in the patient responds differently to the echo. CEUS images can be used to monitor the arterial lumen, but they can also provide information regarding the presence of *vasa vasorum* [31, 32].

The complementary information provided by different imaging modalities has resulted in the interest in investigating both, in combination, in order to enable a more complete assessment of carotid plaque vulnerability. MRI generally produces images that are less noisy and speckled than US, and therefore easier to interpret, while US images have a higher resolution and operate at higher temporal frequencies. Fig. 1.4 shows US and MR images of the same patient. The difference in image intensity patterns, the lower resolution of the MRI and the fact that part of the arterial wall is not visible in US can be noticed.

The possibility to evaluate multiple carotid artery properties associated with atheroscle-

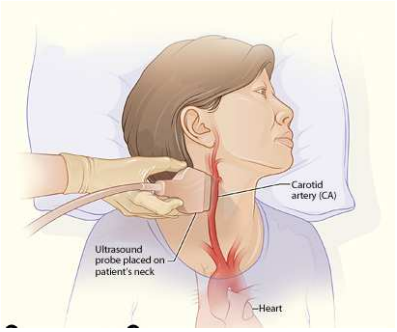

(a) source: Adapted from Wikimedia. Author: National Heart Lung and Blood Insitute (NIH)

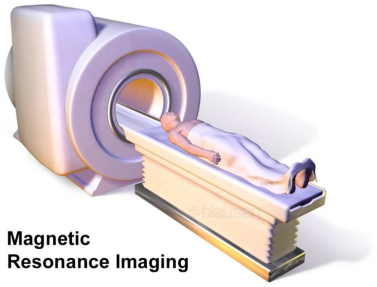

(b) source: Wikimedia. Author: Blausen Medical Communications, Inc.

Figure 1.3: Position of the patient's neck during US (left) and MR (right) scanning.

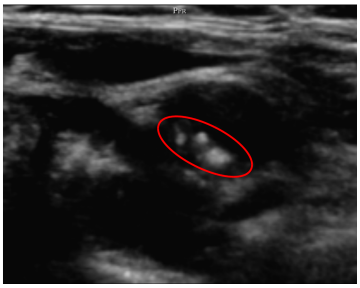

(a) US

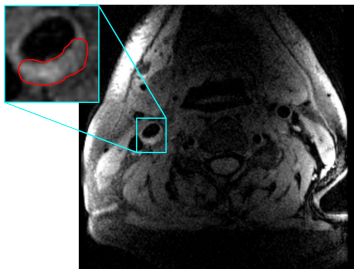

(b) MRI

Figure 1.4: US and MRI of the same carotid artery plaque, the plaque highlighted in red.

rotic disease processes may allow the clinician to better assess the risk of plaque rupture [16, 33]. According to [34] the development of a tool to spatially correlate different modalities would be beneficial for the study of the carotid artery and for further assessment of atherosclerosis. This thesis presents methodologies to perform multimodal registration of imaging modalities to inspect the carotid artery. The global objective of this thesis is to develop and evaluate new image analysis tools to facilitate novel research on the quantification of plaque rupture risk.

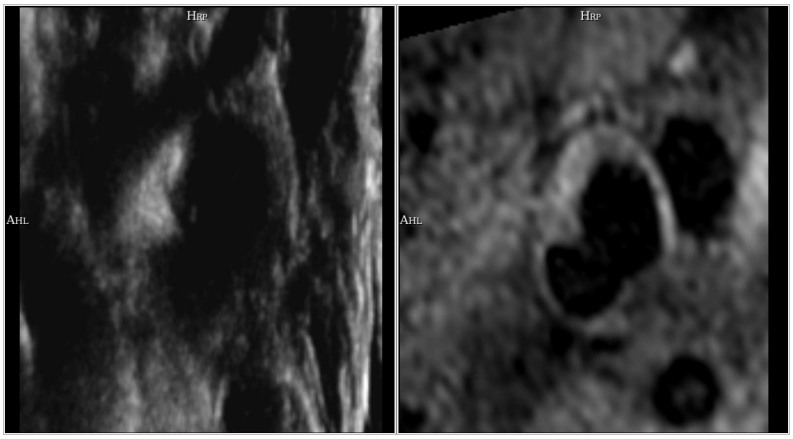

Figure 1.5: Left: US image; right: MRI after registration with US.

1.3 Image Registration

Image registration is the process to determine a transformation that spatially relates coordinates from one image space to another [35]. Registration applications range from mapping images from different subjects, to providing image guidance during interventions, to identifying morphology changes in images of the same patient at different time points, to correlating images of the same patient that were obtained with different modalities [36].
Registration is achieved by identifying characteristics observable in both images. These characteristics can be classified as extrinsic or intrinsic [37]. Extrinsic registration relies on correlation of external objects attached to patient, which appear in the image space. Intrinsic registration, which is the focus of this thesis, relies purely on the image data of the patient him-/herself.
In order to calculate a transformation to properly register the images, a measure is used to evaluate the dissimilarity between images. The matching can be based directly on the voxel intensities ("intensity-based registration") or on landmarks extracted by hand or by image processing ("feature- or point-based registration"). In intensity-based methods the image matching and feature detection are merged in a single step [38], whereas in feature-based methods the features are provided as inputs to the registration algorithm.
The dissimilarity measure is used in an iterative process, called optimization, which aims to find an optimal transformation. At each iteration, an optimizer estimates a transformation to match the *moving image* to the *fixed image*. It is a minimization process, which aims to obtain a better transformation in each iteration so as to minimize the dissimilarity measure [36]. The registration process stops when a minimum in the dissimilarity function is found, resulting in a transformation that correlates the moving image to the fixed image.
Registrations can be classified as rigid or non-rigid [39]. Differently from rigid registrations, which are obtained through translations, rotation or affine transformations;

nonrigid registrations involve deformations in the images.
In this thesis, image registration methods are developed to i) correlate images of different modality (US and MRI), and ii) compensate motion that occurs over time within dynamic US image series. In the first application, the main difficulties are the difference in resolution, image intensities, and anatomical positions during scanning. In the second application, a main challenge is the low signal-to-noise ratio.

1.4 Thesis Overview

The aim of my work is to develop and evaluate new methods for registration of carotid artery images enabling i) combination of different imaging modalities, and ii) tracking of motion in a dynamic series of carotid artery images. This thesis is divided in two parts according to these two sub-aims. Although the specific objectives differ between **Part I** and **II**, the main objective of all research described in this thesis is to establish correspondences between images of the same patient, with the final aim to enable a more comprehensive analysis of the atherosclerotic plaque for improved assessment of rupture risk.
In **Part I (Chapters 2-4)**, the hypothesis is that a better assessment of the arterial morphology can be used to improve 3D US and MRI registration, presenting advantages over purely intensity based registration.
In **Part II (Chapters 5-6)**, the hypothesis is that nonrigid registration of 2D images across time (2D+t) has the potential to generate BMUS (B-Mode US) and CEUS (Contrast Enhanced US) images with improved signal-to-noise ratio, allowing to better assess the lumen morphology in order to provide fused information for posterior vessel analysis.
Chapter 7 summarizes the achievements of this thesis, and provides recommendations for future work.

1.4.1 Part I: US-MRI Registration

Part I of the thesis covers the registration of Magnetic Resonance Imaging (MRI) and free-hand sweep three-dimensional (3D) Ultrasound (US). Example images which represent transversal planes of the carotid artery are shown in Fig. 1.4. The challenges for accurate MRI-US registration are the difference in image intensities, the visibility of different structures, and the position of the patient's neck during scanning. In MRI the patient's neck remains in a natural position, whereas in US the patient's neck is bent and twist to a small degree, and the US probe is moderately pressed against the neck, see Fig. 1.3. Therefore, in US images, soft tissues are slightly deformed in comparison to MRI; which can be noticed in the images. In **Chapter 2** a method for the extraction of the lumen centerlines in US is proposed. This centerline will serve as an important input for subsequent image registration. The method's assumption is that planar cross sections of the arterial lumen in US have an elliptical shape. An algorithm to fit ellipses onto the lumen borders is presented, which enables robust extraction of lumen centerlines in US images. In **Chapter 3** a method to register US and MRI of the carotid artery is introduced. The algorithm initially aligns the

centerlines extracted in each modality and then performs a joint intensity-and-point based nonrigid registration of the images. The validation is performed by computing the overlap between segmentations of the lumen in US and registered segmentations of lumen in MRI. On MRI, the segmentation was performed with a pre-existing semi-automated method and on US it was performed manually. It was observed that, although the registration method achieved reasonable accuracy, it could be improved by the use of image segmentations instead of image intensities. However, the US segmentations used in this chapter were obtained by manual delineation, which would not be feasible in practice. Therefore, in **Chapter 4**, an automated method to register the US and MRI images through geometrical features is presented. The method makes use of lumen centerlines and segmentations as geometrical features in both modalities. The segmentation are extracted by an automatic algorithm which takes the centerline as an initializer. The results of the achieved registration presented a significant improvement in comparison to the results of **Chapter 3**. Fig. 1.5 shows an example of US-MRI registration of an atherosclerotic carotid artery.

1.4.2 Part II: 2D+t US and CEUS Registration

Part II of this thesis addresses image registration in the temporal domain as a tool to compensate non-rigid motion. Registration of images in the temporal domain enables the quantification of motion related properties, and the generation of an image in which the effect of noise is attenuated. The chapters in **Part II** cover the processing of longitudinal US images of the carotid artery. The images we focus on are series of side-by-side, simultaneously acquired and naturally registered longitudinal B-mode US (BMUS) and Contrast Enhanced US (CEUS) images, shown in Fig. 1.6. To compensate for the motion of the carotid artery, registration in the temporal domain is performed by estimating the deformations that minimize the pixel variance across the frames. The motion-compensated BMUS and CEUS images are subsequently averaged, leading to "epitome" images with improved signal-to-noise ratio. These epitome images are the basis of all further analyses. **Chapter 5** presents a method to segment one branch of the lumen in US images. The epitome image is used to roughly classify the background, artifacts, lumen and shadows. After this classification, a dynamic programming technique is applied to refine the lumen segmentation. As an application of the method, we present an estimation of the lumen distensibility. In **Chapter 6**, after the classification of the epitome image, a dual layer dynamic programming is applied to segment the lumen–intima and the media–adventitia layers. This method is also able to automatically detect more than one branch of the carotid artery. In both chapters of the second part of this thesis, nonrigid registration enabled the construction of the epitome images, facilitating subsequent segmentations of the lumen and the lumen–intima and media–adventitia layers. Combining these segmentations with the motion estimates obtained by registration allows analysis of the moving carotid artery geometry over time. Fig. 1.7 shows average images of a CEUS-BMUS series before and after the registration. We can observe that the epitome image constructed after registration provides a sharper representation of the anatomical structures of interest.

Figure 1.6: Side-by-side CEUS and BMUS. An atherosclerotic plaque is highlighted by the ellipse.

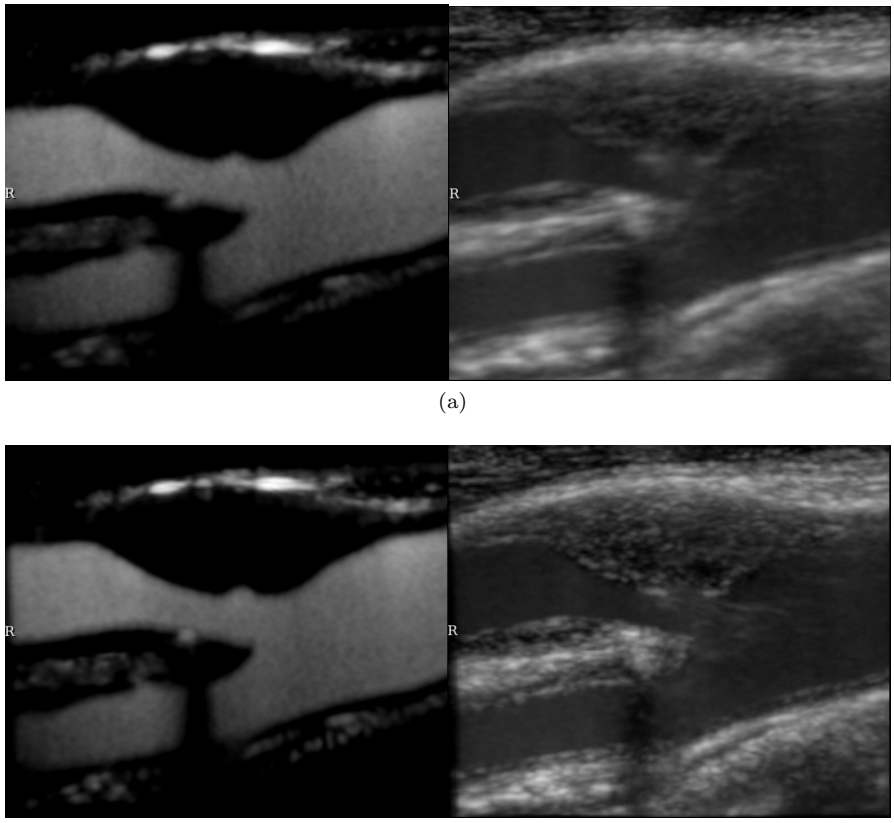

(a)

(b)

Figure 1.7: Side-by-side CEUS and BMUS "epitome" images, based on averaging the original images (a) and on averaging the registered, motion-compensated images (b).

I

US-MRI Registration of Carotid Artery

2

Estimating 3D Lumen Centerlines of Carotid Arteries in Free-hand Acquisition Ultrasound

Abstract: The purpose of this paper is to present a methodology to estimate the carotid artery lumen centerlines in ultrasound (US) images obtained in a free-hand examination. Challenging aspects here are speckle noise in US images, artifacts, and the lack of contrast in the direction orthogonal to the US beam direction. An algorithm based on a rough lumen segmentation obtained by robust ellipse fitting was developed to deal with these conditions and estimate the lumen center in 2D B-mode scans. In a free-hand sweep examination, continuous image acquisitions are performed through time when the radiologist moves the probe on the patient's neck. The result is a series of images that show 2D cross-sections of the carotid's morphology. A tracking sensor (Flock of Birds) was attached to the probe and both were connected to a PC executing the Stradwin software, which relates spatial information to the acquisition data of the US probe. The spatial information was combined with the 2D lumen center estimates to provide a centerline in 3D. For validation, 19 carotid scans from 15 different patients were scanned, their centerlines calculated by the algorithm and compared with results acquired by manual annotations. The average Euclidean distance between both among all the examinations was 0.82 mm. For each examination, the percentage of these Euclidean distances below 2 mm was calculated; the average over all examinations was 92%. Automated 3D estimation of carotid artery lumen centerlines in free-hand real-time ultrasound is feasible and can be performed with high accuracy. The algorithm is robust enough to keep the centerlines inside the vessel, even in the absence of contrast in parts of the vessel wall.

Based upon: **Diego D. B. Carvalho**, Stefan Klein, Zeynettin Akkus, Gerrit L. ten Kate, Arend F. L. Schinkel, Johan G. Bosch, Aad van der Lugt, Wiro J. Niessen ,"Estimating 3D Lumen Centerline of Carotid Arteries in Free-hand Acquisition Ultrasound", published in *International Journal of Computer Assisted Radiology and Surgery*

2.1 Introduction

Medical imaging studies of the carotid artery generally aim to observe the presence of atherosclerotic plaque and the effect on the geometry of the vessel lumen. Both atherosclerotic plaque, as well as luminal stenosis are related to cerebrovascular diseases [40]. Several imaging modalities are used, such as magnetic resonance imaging (MRI), computed tomography angiography (CTA), and ultrasound (US), each having their own advantages and disadvantages. MRI has good soft-tissue contrast allowing plaque composition analysis in 3D, but the resolution of the images is often limited, especially in the slice direction. CTA visualizes the 3D lumen geometry with high resolution and clearly shows calcifications, but other plaque components (lipids, fibrous tissue, hemorrhage) are hard to distinguish. US provides 2D images with high in-plane resolution allowing intima-media thickness measurements, it has high temporal resolution enabling motion analysis to measure the distensibility of the artery, but may present speckles, noise and a lack of contrast in the direction perpendicular to the beam direction. A good scenario could be to combine the information from MRI, CTA, and US by an integrated analysis, in order to extract plaque characteristics that cannot be identified using a single modality. For such a multimodal analysis, co-registration of the different modalities would be helpful. There are several issues that make the registration of US with MRI/CTA challenging. Firstly, the US scans are mostly acquired in a 2D mode; slices are acquired instead of volumes. Secondly, the imaging characteristics are completely different, which complicates the use of purely intensity-based registration methods (for example, using mutual information). Thirdly, the initial alignment between MRI/CTA and US is rather arbitrary (it depends on the scanner's coordinate system and the position of the US probe). The lumen centerline seems a good candidate for a geometrical landmark that can be extracted reliably in each modality, based on which a robust initial alignment procedure can be developed.

In this work, we present a method to track 3D lumen centerlines of the common, internal, and external carotid artery, from 2D B-mode US scans obtained in a free-hand acquisition, where the probe is gradually moved along the neck of the patient, imaging transverse sections. Each individual ultrasound image in this 2D free-hand acquisition represents a plane cut of a volumetric area (in our case, a region of the patient's neck), but with unknown information about the plane orientation and its position in a three-dimensional space. An attached tracking device is necessary to record the probe's position and orientation during the acquisition. There are also 3D ultrasound techniques, in which 2D images are acquired from a known position through mechanical displacement of the probe [23]. However, 2D probes are more widely used, because they have a higher temporal resolution. Intima-media thickness (IMT) is usually measured in longitudinal sections of the carotid [41]. The observation of the carotid from that perspective also allows to quantify the extension of the atherosclerotic plaque and to analyze the behavior of the wall's motion, but it does not provide enough data to build a good three-dimensional representation of the vessel. The extraction of centerlines from tubular structures in other modalities, than free-hand ultrasound, has been addressed in different works [42–46]. Schaap et al. [47] give an extensive survey of the literature and present an experimental comparison

of algorithms to extract centerlines of coronary arteries. Hameeteman et al. [48] performed a comparison of different algorithms to extract carotid arteries in CTA. Noble and Boukeroui [49] present a survey of different techniques for the segmentation of B-mode US images, including vessels.
The publications most related to our research are from Abolmaesumi and Sirouspour [50], Golemati et al. [51], Hammer et al. [52], and Wang et al. [53, 54]. Abolmaesumi & Sirouspour developed a technique to extract boundaries for cavities in ultrasound images. Their method identifies the boundaries by tracing equispaced radii from a given seed point that lies inside the cavity; visually well-defined borders are assumed. Golemati et al. employed the Hough transform to segment arterial sections during wall motion analysis of the carotid in transverse and longitudinal sections. The difficulty in applying this technique on a free-hand sweep lies in choosing the appropriate parameters. Due to the probe position and the anatomy of the carotid artery, the artery can be represented on the images in elliptical shapes of different radii across the same series. Hammer et al. presented a methodology to build 3D representations of the carotid and femoral arteries from free-hand US acquisitions (using a tracking device) by semi-automated vessel segmentation. Wang et al. developed an algorithm to track the area of the CCA and jugular vein in transversal sections. In their technique, the ray casting method is employed to identify the vessels boundaries and an ellipse is fitted using the end points of the rays. In other to achieve a better adjusted ellipse, there is an intermediate step in which outliers rays are pruned before the fitting.
In this paper, an algorithm inspired by Wang's Spoke Ellipse algorithm [53, 54] is proposed to semi-automate the calculation of centroids of the common, internal, and external carotid in each 2D scan. Our method requires only three manually placed seed points, indicating the common (CCA), internal (ICA), and external (ECA) carotid arteries. The algorithm is designed to be robust against missing edge information in parts of the carotid wall, due to the lack of contrast in directions orthogonal to the US beam direction. A magnetic tracking device called Flock of Birds (FOB) (Ascension Technology, Burlington, VT, USA) was attached to the US probe, to register the displacements during the acquisitions. To synchronize the sensor information with the images, we used the publicly available Stradwin software [25]. The next section presents the algorithm for the centerline extraction.

2.2 Method

To estimate a 3D lumen centerline of the carotid arteries, based on 2D transversal free-hand US acquisitions, the lumen centroid must be identified in each 2D image. Using the data from the tracking device, the centroids can be expressed in 3D coordinates, which allows construction of a smooth 3D center line.
In 2D B-mode US images, the carotid's lumen is represented by a relatively low intensity, and the vessel wall has a higher intensity. In transverse sections, the vessel wall is visible as an (approximately) ellipsoid structure. Part of the vessel wall is often missing though (see for example Fig. 2.1), due to the lack of contrast in the direction perpendicular to the US beam direction. We developed a robust ellipse

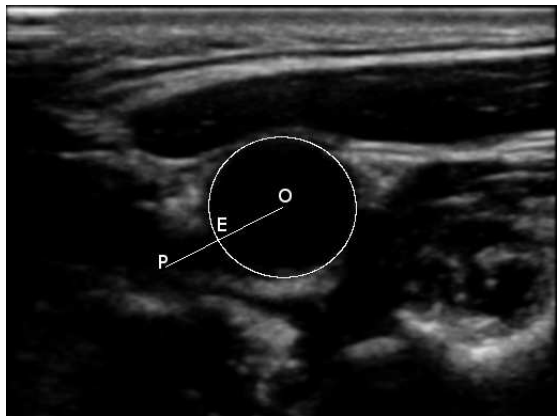

Figure 2.2: Points O, E and P.

fitting algorithm that can deal with this situation.

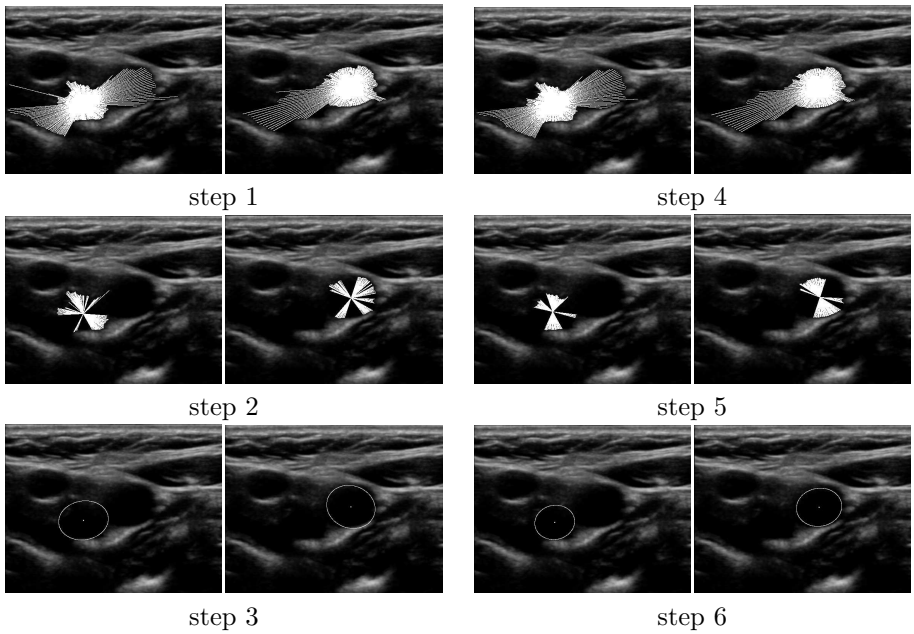

Figure 2.1: Images registering the outputs of each one of the six steps of the algorithm for both ICA and ECA in the same slice.

Step 1: The algorithm starts by tracing rays in many directions from a seed point (*Point O* in Fig. 2.2) that is known to be inside the vessel. The angle between two rays is defined by dividing 360^o by the number of rays that will be traced. In our experiment, we used 256 rays. The length of each ray is limited by the position where

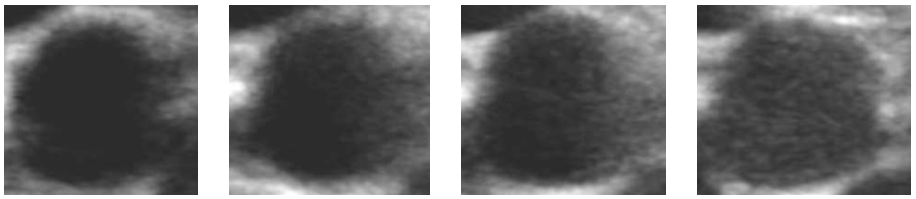

Figure 2.3: Variation of the area of the speckles inside the lumen.

it reaches a pixel with intensity above a certain threshold (τ), indicating that the vessel wall is being crossed *(Point P)*.

Step 2: Since we expect the vessel's cross-section to have a more or less circular shape, we expect a similar length among the rays. Outliers are indicative of missing edges (causing very long rays) or noise within the lumen (causing very short rays). In order to discard the outlier rays, a given percentage (ρ) of the rays that have smallest length and the same percentage of the rays that have longest length are pruned.

Step 3: An ellipse is fitted to the extreme points of each remaining ray. The method presented in the OpenCV library is used to fit the ellipse [55].

Step 4: A new set of rays is traced using the center of the ellipse as the initial point (*Point O*).

Step 5: A second fine-pruning step is performed. For each ray, the distance is calculated between the end Point P and the point where it has intersected the previously fitted ellipse (*Point E*). The standard deviation and mean of the *EP* length are calculated. If for a given ray, the length of the line segment *OP* is bigger than the length of *OE* and its *EP* length is one standard deviation away from the mean of other *EP* lengths, the *Point P* is disconsidered and *Point E* is used. If *OE* is larger than *OP*, the ray is always preserved. By discarding only points that are outside the ellipse, we introduce a bias to shorten rays to increase the chance that the centerpoint remains within the lumen in cases where large points of the lumen boundary are missing. This step is necessary in cases where the edge information in a large part of the lumen boundary is missing.

Step 6: By the last, the remaining rays are used to fit a second ellipse which the centerpoint is saved.

This centerpoint is used as the seed point in the next image in the series and then these 6 steps are repeated. We are initializing the algorithm with three seed points, one at each extreme of the carotid. The algorithm starts at the points in the internal and external carotid and traverses through the scans while calculating both centroids, until they are $1\,mm$ away, at which point the bifurcation is assumed to be located. Then the algorithm starts in the seed of the common carotid and stops when it reaches the slice where the seed points of the bifurcation were located. This approach is invariant to the direction (from the patient's shoulders to head, or viceversa) that the free-hand acquisition was performed alongside the neck. In the end, the resulting centerpoints are smoothed (Gaussian kernel with standard deviation of $1\,mm$) and interpolated by three spline curves, using 3rd order polynomial splines: one for CCA, one for the ICA, and one for ECA.

Since the lumen and vessel wall intensity distributions may vary between images (even of the same series), we developed a procedure to determine τ based on the intensity distribution around the three initial seed points. Before starting tracing rays, a kernel of size $1 \times 1\,mm^2$ is created around each of the three seed points. The mean (μ) and the standard deviation (σ) of the pixel intensities in the kernel are calculated. The threshold value is then set to $\tau = \mu + 2.5\sigma$, assuming a Gaussian distribution of the lumen intensities. A user defined minimum standard deviation (σ_{min}) is enforced to assure that even if the kernel is located in an area with no variation in pixel intensities, the threshold will have a higher value than the pixel at the seed point.

If point O is located at a position where all surrounding pixels have an intensity higher than τ , the algorithm fails. This situation may occur when there is a large variation of intensities along the lumen, due to local variations in the amount of speckle noise, as shown in Fig. 2.3. Figure 2.4 displays the mean pixel intensities along manually annotated centerlines in two different patients. It shows that the μ and σ values estimated from the three initial seed points are not always representative for the entire sequence. We experimented with several standard denoising methods (e.g., bilateral filtering, median filtering), but these did not solve the problem, since it is not only the standard deviation of the noise that increases, but also the mean intensity.

If the algorithm arrives at a slice where all neighbor points of point O have a value larger than τ, it leads to rays with a zero length during the raycasting in Step 1. In case of such an exception, the algorithm tries to restart from the other end of the centerline. Five cases are distinguished, depending on where the exception occurs (Fig. 2.5).

The case that the algorithm succeeded in reconstructing the centerline without presenting failures in any slice is labeled **Case A.**

If the algorithm fails in the common carotid, the bifurcation point is used as a new seed point **(Case B)**. Eventually the algorithm will not be able to calculate all the centerpoints from this direction either, as the region with speckles will be encountered from that side as well. The centerpoints in the intermediate slices with speckles will be defined after interpolating the calculated points with the spline curve.

If the centerpoint cannot be estimated in a slice in the ICA or ECA, the initial seed point in the common carotid is used as a seed point and it stops when the specific slice is reached **(Case C)**. In this case, the algorithm will not find the bifurcation, but there will be at least one landmark (centerpoint) per slice.

If case C occurs, but the centerline cannot be estimated completely in the CCA either, the last centerpoint of the vessel in which the centerline was successfully estimated is used as a reference **(Case D)**; i.e., if the problem occurred in the ECA, the last centerpoint in the ICA is used to match the remaining path of the CCA.

If in the last step of case D, the centerline cannot be estimated again, the algorithm stops **(Case E)**.

The algorithm was fully written in C++, the code is compliant with the GCC compiler and it was stored in a static library. The library was loaded in a MeVisLab (http://www.mevislab.de/) module. In the MeVisLab environment, the GUI interface was handled. At the end of the process, the shape of the centerline in 3D can be observed with the help of rendering tools see Fig. 2.6.

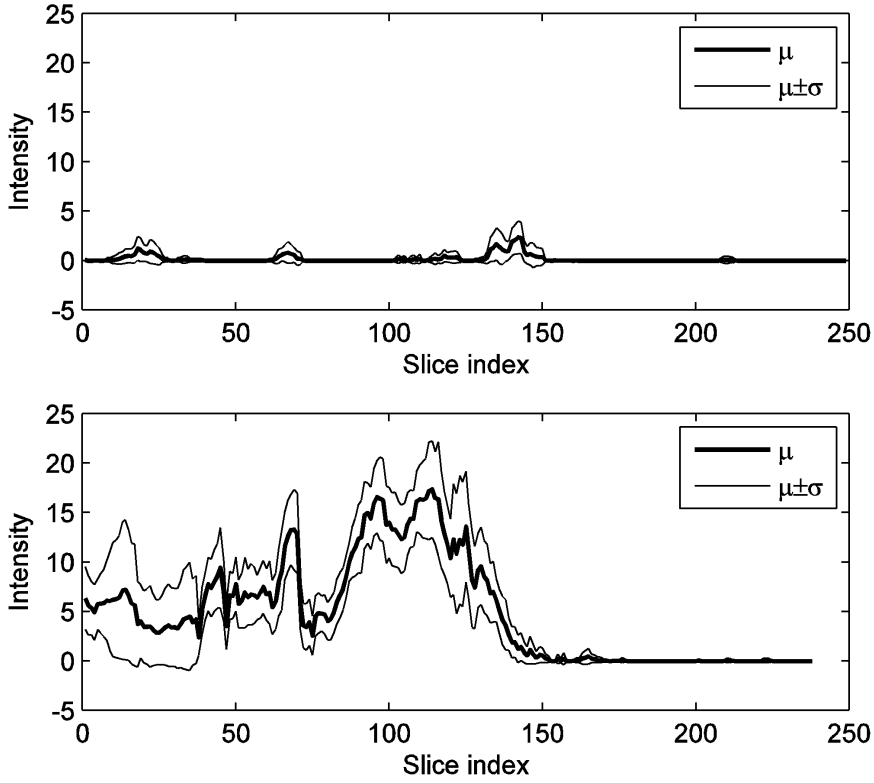

Figure 2.4: The graphs show the variation of the pixel intensity in $1 \times 1\, mm^2$ region around the manual annotated lumen centerlines. The first graph is from a sequence which almost does not suffer from speckles inside the lumen. The second sequence shows a more difficult case

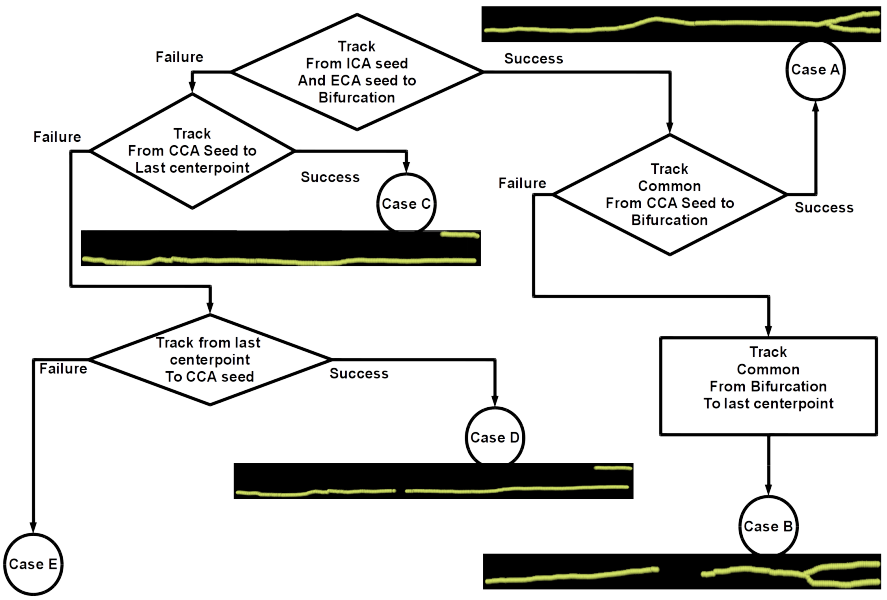

Figure 2.5: Cases flow chart. The centerpoints are represented in 3D. The z coordinate corresponds to the slice index of the images sequence in the ultrasound acquisition. All the centerlines are represented before the spline interpolation.

2.3 Experiments

2.3.1 Motion tracking and 3D centerline construction

We attached a magnetic tracking sensor, Flock of Birds (FOB), to the US probe to register the motion during the free-hand acquisition. The sensor was attached using a custom-made tool. The FOB sensor provides the difference in orientation and position between its own position in relation to a transmitter. Since the transmitter remains fixed during the acquisition, the sensor movements allow us to track the probe displacement.

We used the Stradwin software to register the spatial coordinates with a specific image. It gathers the images of a video stream provided by a video grabber that is connected to the video output of the US machine. In the end of the scanning, the information is stored in two different files, the first containing the raw data of each acquired image and the second the information related to the position sensor and the whole software calibration. The transformation to world coordinates can be read from these files, and applied to the 2D centroids to obtain a 3D centerline. Figure 2.6 shows an example performed on data gathered from a volunteer.

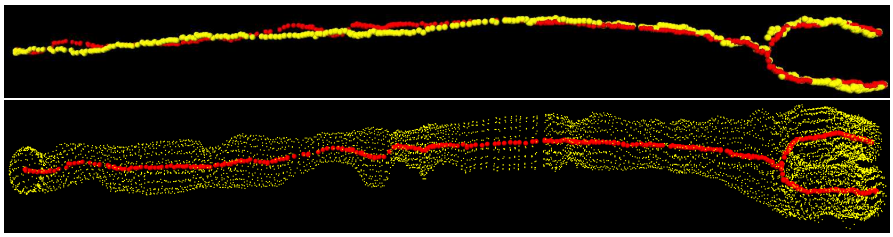

Figure 2.6: representation of the carotid artery's center points after the transformation to 3D coordinate system using the Stradwin information. The image above shows the manual annotation (yellow) and the results obtained with the algorithm (red). The image bellow shows a cloud point representing the borders of the ellipses calculated after the step 6.

2.3.2 Evaluation on patient data

2.3.2.1 Subjects

We evaluated the method by comparing the centerpoints estimated by the algorithm with centerpoints estimated by human manual annotation in every single slice. Nineteen different clinical examinations from 15 patients were tested. The exams 1 and 2 belong to one patient, exams 4 and 5 belong to a second patient, and exams 17, 18, and 19 belong to a third patient. The remaining examinations are from different patients. All the examinations were performed with a Philips iU22 system, using the Philips L9-3 probe. The pixel spacings were in a range between 0.064 × 0.064 and 0.095 × 0.095 mm2. Number of slices in each sequence varied from 215 to 249.
The FOB tracking system was not yet used in these studies, since we were aiming to evaluate the results of the algorithm taking in consideration only the issues related to the ultrasound image, such as missing borders and sensitivity to noise. A subjective quality examination was performed on all images classifying the images according to certain characteristics. The result of this examination is shown in Table 2.1.

2.3.2.2 Algorithm evaluation

Figure 2.7 shows box plots of the Euclidean distances between the manual and calculated centerpoints for each examination. In cases where the algorithm could not find the bifurcation due to speckles, the slices where no centerpoints were found in the ECA or in the ICA were not compared. This happened in exams 13, 14, and in exam 16 using the second set of seed points. The average Euclidean distance between manual annotations and the algorithm results among all the examinations was 0.82 mm. For each examination, the percentage of these Euclidean distances below 2 mm was calculated; the average over all examinations was 92%. In this experiment, the parameters σ_{min} and ϱ were manually tuned by checking visually the results with different values. The best results were achieved with $\sigma_{min} = 4$ and $\varrho = 30\%$.
In every measurement, the manual and calculated markers indicated a different position of the beginning of the bifurcation. The algorithm defines the bifurcation as the point where the internal and external centerpoints are less than 1 mm away from

Exam nr.	1	2	3	4	5	6	7	8	9	10	11	12	13	14	15	16	17	18	19
A	x	x			x	x		x	x			x		x	x		x	x	x
B			x								x		x	x		x			
C	x	x	x	x	x	x	x	x	x	x		x	x	x	x	x	x		
D	L	R	L	L	R	L	L	L	L	L	R	L	L	L	L	R	L	R	R
E	Y	Y	Y	Y	Y	Y	Y	Y	Y	N	Y	Y	Y	Y	Y	Y	Y	N	N

Table 2.1: Classification of examinations from 1 to 19. Rows: (A) Mild speckles in at least one slice, (B) Speckles in the whole lumen in at least one slice, (C) Missing Borders, (D) the side of the carotid: L-left or R-right, (E) presence of plaque Yes-Y, N-No.

each other. In these specific slices, the closer of the two centerpoints is chosen to be compared with the common centerpoint in the other annotation. When the algorithm finds the bifurcation in a different slice than in the manual annotation this distance can be considerable, like in exams 3, 6, and 7. The centerpoint is not located outside the lumen, but it lies between the manually annotated centerpoints.
To evaluate the robustness with respect to the choice of the initial seed points, each dataset was evaluated with two different seed point sets and the results were compared for every examination. Figure 2.7 shows for each examination, a box plot of the Euclidean distance between the centerpoints produced by the algorithm with two different sets of seed points. In the exam 16, the median had a value bigger than 1 mm because using the second set of seed points, the algorithm was not able to find the bifurcation.

2.3.2.3 Parameters testing

To demonstrate the impact of parameter values, we applied different sets of parameters and calculate the euclidean distance with the manual annotated points. On each subject, we used five different configurations of parameters sets, varying the σ_{min} and ρ. Table 2 summarizes the results.

	$a(\sigma_{min} = 2, \rho = 30\%)$	$b(\sigma_{min} = 4, \rho = 30\%)$	$c(\sigma_{min} = 8, \rho = 30\%)$
Average Mean (mm)	0.955	0.817	1.105
Average StdDev (mm)	0.744	0.620	1.253
Bifurcation Found	13	16	12
Diverged	4	0	5
	$d(\sigma_{min} = 4, \rho = 20\%)$	$b(\sigma_{min} = 4, \rho = 30\%)$	$e(\sigma_{min} = 4, \rho = 40\%)$
Average Mean (mm)	1.316	0.817	3.841
Average StdDev (mm)	3.805	0.620	8.747
Bifurcation Found	16	16	7
Diverged	3	0	5

Table 2.2: The label bifurcation found indicates the number of cases (out of 19) in which the bifurcation was found (which corresponds to cases A and B in Fig. 2.5). The label diverged expresses the number of cases in which at least one centerpoint was marked outside the lumen

The execution of the algorithm with configuration 'b' resulted in centerlines with all points inside the lumen. In configuration 'a', the algorithm characterizes wrongly some noise pixels inside the lumen as the vessel wall. With configuration 'c', the real boundaries of the lumen were sometimes missed, due to a higher threshold. In configuration 'd', less outlier rays were pruned, leading to wider ellipses and, consequently, sometimes divergence. The results of configuration 'e' were affected by the exclusion of too many rays, generating ellipses that poorly represented the lumen. It should be noted that the optimal choice of σ_{min} depends on the intensity range of the US images, which all were normalized to [0–255] in our case.

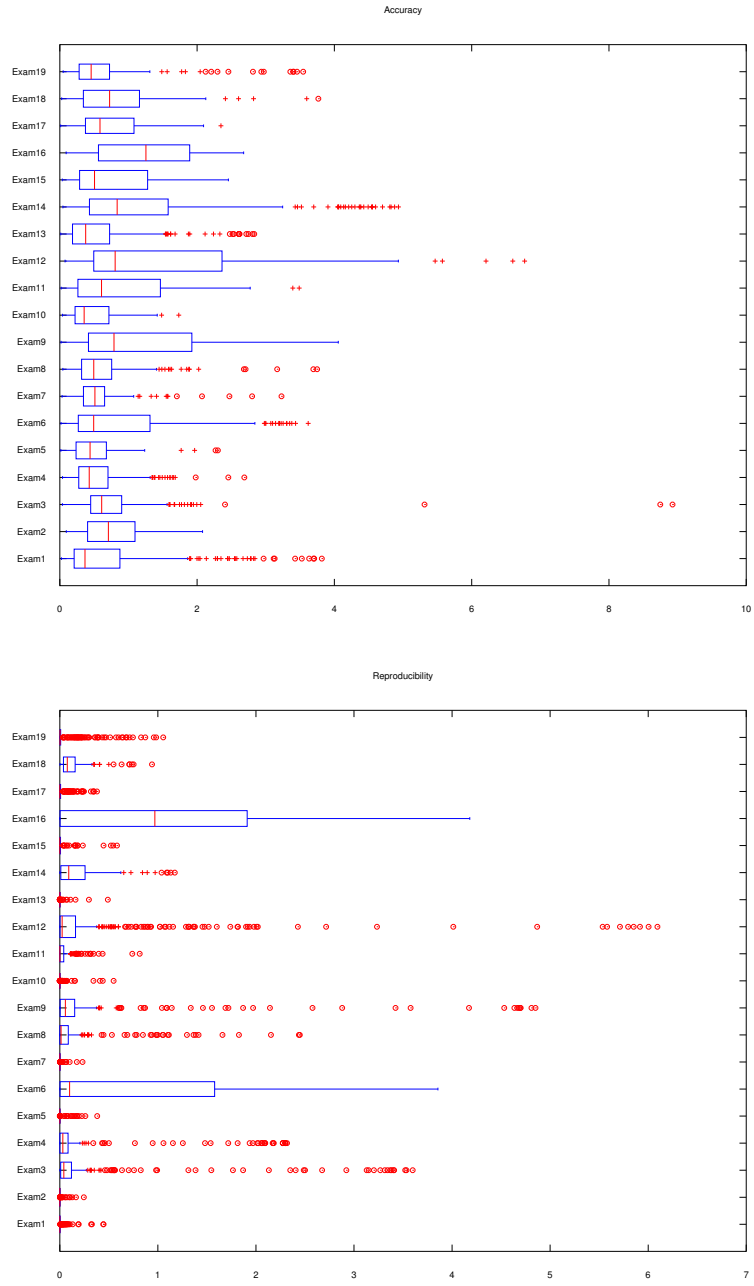

Figure 2.7: Euclidean distance of the algorithm center points and the center points chosen manually in mm (top). Euclidean distance of the algorithm center points in the first and second set of seed points in mm (bottom). Symbol for the points that lie outside 3 times the interquartile range is 'o', default symbol for points between 1.5 and 3 times the interquartile range is '+'.

The algorithm in configuration 'b' was executed again on a set of 8 new image sequences, to verify if we did not overtrain our method on the 19 datasets that were used in all other experiments (since we did not perform a leave-one-out crossvalidation). The 8 new datasets originate from 4 patients (L/R artery) and had similar characteristics as the other 19 datasets. The results were visually inspected. It was verified that in all of the 8 cases, the centerline remained inside the lumen and the bifurcation was found in 6 cases.

2.4 Future Work and Discussion

This paper presents a methodology to estimate the 3D lumen centerline of carotid arteries scanned with free-hand 2D US. The algorithm's main objective is to calculate the vessel's centerline even if the image does not provide full information of its boundaries due to limitations in the US examination. The algorithm is robust enough to keep the centerlines inside the vessel in the absence of visible edges in the region that represents the lumen. The sensitivity to the choice of σ_{min} and ϱ was assessed by testing five different sets of parameters. The execution time of the algorithm varied from 9 to 12 s depending on the number of slices and centerpoints in the examination. The whole process considering the disk access and the Gaussian smoothing took between 19 and 23 s. All experiments were performed on an Intel(R) Xeon(R) CPU E5520 with 12 gigabytes of RAM.

The definition of the threshold for the detection of lumen boundaries is currently based on the intensity distributions around the three initial seed points. This approach may fail when the noise characteristics in the lumen change along the image series. An adaptive procedure, which updates the threshold in every scan, may be beneficial in such cases.

As a future work, we aim to use this centerline estimate to register the US scans to MRI and CTA, by matching the centerlines. Despite the initial intention of acquiring a geometrical landmark of an US acquisition to match the images to other modalities such as MRI and CTA, the extracted lumen centerline could be useful on its own right. Geometrical characteristics that might be relevant for risk assessment of plaque development can be extracted from the US-based centerline, without the need for performing an additional (expensive) MRI or CTA. According to [56], it is possible to characterize the curvature, torsion, and tortuosity by applying classical differential geometry of curves on the line segments that compose the centerline. Lee et al. [57] investigated the carotid geometry and its impact in the blood flow. The exposure to the so-called "disturbed" flow may be a risk factor for atherosclerosis. Lee et al. considered that tortuosity is among the features that influence the hemodynamic disturbance. Analysis of more examinations and comparisons with centerlines extracted from other modalities will allow us to check the potential of the algorithm in identifying these biomarkers.

3

Joint Intensity-and-Point Based Registration of Free-hand B-Mode Ultrasound and MRI of the Carotid Artery

Purpose: To introduce a semi-automatic algorithm to perform the registration of free-hand B-Mode ultrasound (US) and magnetic resonance imaging (MRI) of the carotid artery. **Methods:** Our approach combines geometrical features and intensity information. The only user interaction consists of placing three seed points in US and MRI. First, the lumen centerlines are used as landmarks for point based registration. Subsequently, in a joint optimization the distance between centerlines and the dissimilarity of the image intensities is minimized. Evaluation is performed in left and right carotids from six healthy volunteers and five patients with atherosclerosis. For the validation we measure the Dice similarity coefficient (DSC) and the mean surface distance (MSD) between carotid lumen segmentations in US and MRI after registration. The effect of several design parameters on the registration accuracy is investigated by an exhaustive search on a training set of five volunteers and three patients. The optimum configuration is validated on the remaining images of one volunteer and two patients. **Results:** On the training set we achieve an average DSC of 0.74 and a MSD of 0.66 mm on volunteer data. For the patient data we obtain a DSC of 0.77 and a MSD of 0.69 mm. In the independent set composed of patient and volunteer data the DSC is 0.69 and the MSD is 0.87 mm. The experiments with different design parameters show that nonrigid registration outperforms rigid registration, and that the combination of intensity and point information is superior to approaches that use intensity or points only. **Conclusions:** The proposed method achieves an accurate registration of US and MRI, and may thus enable multimodal analysis of the carotid plaque.

Based upon: **Diego D.B. Carvalho,** Stefan Klein, Zeynettin Akkus, Anouk C. van Dijk, Hui Tang, Mariana Selwaness, Arend F.L. Schinkel, Johan G. Bosch, Aad van der Lugt, Wiro J. Niessen, "Joint intensity-and-point based registration of free-hand B-mode ultrasound and MRI of the carotid artery", published in *Medical Physics*

3.1 Introduction

The carotid arteries are blood vessels responsible for transporting blood and oxygen to the brain and the facial muscles. Atherosclerosis is a chronic inflammatory condition which causes a narrowing of the arterial lumen due to plaque formation. The interaction between blood elements, disturbed flow, arterial wall morphology and processes such as lipid accumulation, necrosis and calcification play a role in the formation of an arterial plaque [58]. It was shown that atherosclerosis risk factors are more strongly associated with carotid plaque size than with carotid stenosis [59]. The rupture of plaques is associated with the occurrence of ischemic strokes [60]. The risk of rupture is related to the composition and the morphology of the atherosclerotic plaque [61]. Atherosclerotic plaques can be visualized with different imaging modalities, such as ultrasound (US), magnetic resonance imaging (MRI) and Computed Tomography Angiography (CTA) and plaque components can be quantified [62]. However, not all the plaque characteristics can be observed in a single modality [33]. In this work we investigate the registration between free-hand B-mode US and black-blood MRI of the carotid artery. This registration will facilitate the correlation of plaque characteristics observed in different imaging modalities.

Besides the differences between US and MRI, regarding voxel intensities, resolution and image appearance, there are also differences in the geometry of the carotid artery during scanning due to the nature of the examination procedures. During the MRI examination the neck of the patient remains in a natural position. In free-hand US the neck of the patient is slightly bent and twisted and the probe is pressed against the skin, which causes a compression of the involved tissues. The volume of coverage also varies in both modalities. In US it is not possible to observe details which are located underneath the mandible. Registration should be sufficiently robust to cope with these aspects.

Previous works have addressed US-MRI registration. Slomka et al. [63] performed registration of carotid 3D free-hand power doppler US and Magnetic Resonance Angiography (MRA) data. These modalities clearly visualize the vessel lumen, which was exploited to perform the registration. The use of power doppler US would only permit an indirect registration between B-Mode US and black-blood MRI. Their method was based on maximization of mutual information, using a rigid transformation model, and was evaluated on a data set of six patients. Nanayakkara et al. [64,65] performed registration of 3D US and MRI with a constrained nonrigid registration approach, using a 'twisting and bending' transformation model. In their work, an initial rigid registration was performed considering landmarks, followed by a nonrigid registration which takes into account the normalized mutual information between the images. The 3D US volumes were composed of a sequence of images of B-Mode US acquired with a probe displaced by a motorized device. Images from six patients were used for evaluation. Chiu et al. [66] performed the registration between 3D US acquired with a volumetric linear transducer and MRI on data obtained from three patients. Their technique consists of registering points representing the arterial outer wall, which is extracted by a manual segmentation of the MRI and a semi-automated segmentation of the US. After an initial alignment considering the bifurcation point, the point sets are registered rigidly with the Iterative Closest Point (ICP) algorithm [67]. After-

wards, a slice-by-slice manual registration is performed. The method was evaluated on three patients. Previous research on the registration of free-hand US and MRI of other anatomical regions includes the work by Penney et al. [68] on liver images. The US probe position was estimated with the use of an external optical device and the registration was based on the alignment of probabilistic lumen segmentations. Registration of brain vascular structures (not carotid) from freehand US and MRA has been presented by Reinertsen et al. [69]. This method is based on the alignment of centerlines using the ICP algorithm. In the field of image-guided interventions, much research has focused on the registration of 2D digital subtraction angiography (DSA) with preoperative MRI or CTA, e.g. Jomier et al [70], and Groher et al [71, 72]. Jomier et al. [70] presented an algorithm to perform rigid 2D-3D registration of bi-plane DSA images with a 3D model of the liver vasculature extracted from MRI. The method minimizes a weighted sum of intensities around the MRI centerlines projected in the 2D planes. Groher et al. [71] introduced a nonrigid 2D-3D registration approach, applied to liver images. The method assumes that centerline models of the liver vasculature have been extracted previously from the 2D DSA and from the 3D CTA or MRI. These 2D and 3D models were aligned using an enhanced version of ICP that takes into account regularization terms constraining the length of vessel segments and the smoothness of the displacements. In follow-up work by the same group [72], a model-to-image approach was adopted. A 3D model of the liver vasculature was obtained from a preoperative CTA or an intraoperative cone-beam reconstruction, by region growing. A vessel-enhancement filter was applied to the 2D DSA image to enhance tubular structures. The deformation was estimated by maximizing the average intensity in the vessel-enhanced DSA in circular regions around the projected 3D centerline, while constraining the lengths of vessel segments. While the projective (2D) nature of DSA makes accurate registration in these applications a very challenging task, the multiple bifurcations in the liver vasculature aid in establishing correspondence. In contrast, carotid artery US images typically show only one bifurcation. Moreover, the vessels are more clearly identifiable on liver DSA than on carotid free-hand B-mode US, which is suffering from reduced contrast at edges parallel to the US beam direction. Therefore these 2D-3D approaches may not be directly applicable to the considered problem of registering B-mode US with black-blood MRI of the carotid artery.Based on this literature survey, we identified the following shortcomings and open issues: 1) The need for many manual interventions [66]. 2) In 3D freehand B-mode US the lumen boundary of the carotid artery is not always well-defined (especially at edges parallel to the US beam direction); therefore, approaches that rely on a clear lumen representation [63,68] are less suitable. 3) Some approaches are based on geometric landmarks, and some use an intensity-based approach [64, 65]; it remains to be investigated which approach is more successful, and if the two approaches could be combined in order to improve the accuracy and robustness.

In this work, we propose a joint intensity-and-point based registration framework to perform rigid and nonrigid registration of US and MRI of the carotid artery. The only required user input in our method consists of three seed points in the carotid lumen, both in US and MRI. The method was evaluated on images from six healthy volunteers and five patients with atherosclerotic plaque, using both left and right arteries.

Two measures of registration accuracy based on overlap of ground truth lumen segmentations were used. An extensive evaluation of design parameters was performed in a training set composed of images from five volunteers and three patients. In order to investigate the relative importance of the intensity-based and point-based terms, we varied the weighting of these terms, and evaluated the resulting registrations. Hereby, the extreme cases of purely point based and purely intensity based approaches were naturally included. To evaluate the impact of the transformation model, rigid registration was compared against nonrigid registration with different degrees of deformation. We also implemented and evaluated a reference approach, which uses the ground truth manual lumen segmentations for the registration, and thus provides insight in the maximum achievable registration accuracy. Based on the results of these experiments, the optimal parameters for the method were selected. To verify the robustness of these parameter settings, we performed an additional evaluation on the previously unseen data of two patients and one volunteer. A preliminary version of this work was presented on a conference [73]. Compared with our previous work, the method has been automated to a larger extent, and the evaluation has been extended substantially.
Summarizing, the contribution of this work is fivefold: 1) We introduce a customized joint intensity-and-point based registration method for registration of carotid US and MRI. 2) The method is semi-automatic, requiring the user to select only three seed points in each imaging modality. 3) The relative importance of the intensity-based and point-based terms is extensively evaluated to gain insight in their contributions to the registration accuracy. 4) The influence of the deformation model (rigid vs. various degrees of nonrigid) is evaluated. 5) The method with optimal parameter settings is validated on an independent test set composed of previously unseen images.

3.2 Method

3.2.1 Registration Framework

The objective is to find a transformation T that registers the MRI volume M to the ultrasound volume U. Besides the image intensities, we use points on the MRI and US lumen centerlines m and u. The proposed method starts by extracting the lumen centerlines m and u in both modalities, using two previously validated centerline tracking algorithms [74,75]. The centerline points are then registered, resulting in an initial transformation. Subsequently, a joint intensity-and-point based registration is performed, in which rigid and nonrigid transformations are estimated by minimizing both the distance between centerlines and the dissimilarity between image intensities. The transformation T is composed of sub-transformations, which originate from the initial point-based centerline registration and from the joint intensity-and-point based registration. Figure 3.1 schematically represents the registration framework. The transformations T_{init} and $T_{centerline}$ are calculated in the initial centerline registration stage and are described in Section 3.2.2. The joint intensity-and-point based optimization criterion employed to calculate the subsequent rigid (T_{rigid}) and nonrigid ($T_{nonrigid}$) transformations is defined in detail in Section 3.2.3. Section 3.2.4

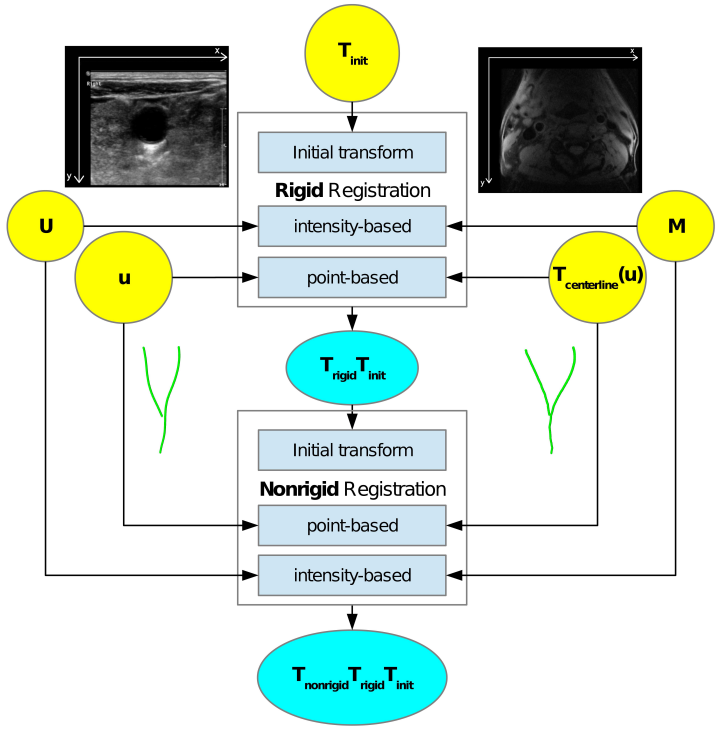

Figure 3.1: Flowchart of the joint intensity-and-point based registration method. U and M are the 3D US and MRI images, respectively, and u represents the carotid lumen centerline in US. T_{init} and $T_{centerline}$ are input transformations that result from an initial point-based registration of lumen centerlines. The output of the registration is a transformation T that is composed by the initial global (rigid) transformation T_{init}, a refined rigid transformation T_{rigid} (estimated in the first registration stage), and a nonrigid B-spline transformation $T_{nonrigid}$ (estimated in the second registration stage).

provides implementation details.

3.2.2 Centerline Registration

In this section we describe the semi-automatic extraction of the centerlines and their subsequent registration. Figure 3.2 shows a flowchart of the point-based centerline registration, consisting of three stages. The three sub-transformation T_0,T_1, and T_2 will be defined in this section.

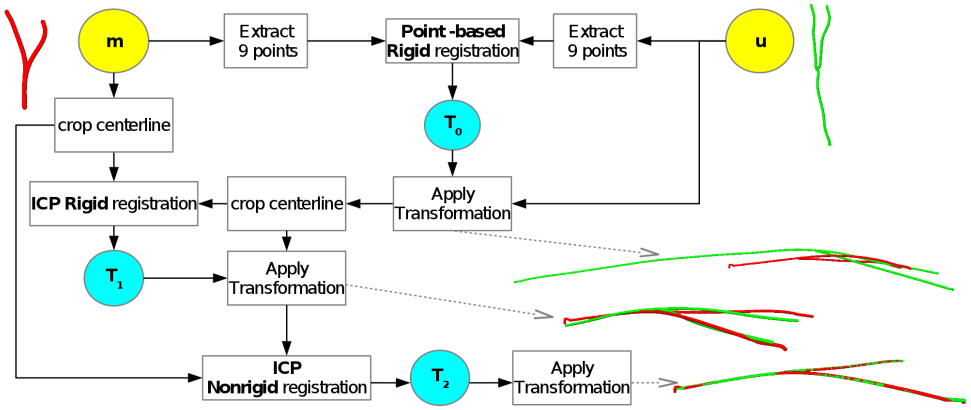

Figure 3.2: Flowchart of the initial point-based registration of lumen centerlines. u and m represent the US centerline (green) and the MRI centerline (red), respectively. The centerlines are registered in three stages: 1) point-based rigid registration using 9 corresponding landmarks, 2) rigid registration with the iterative closest point (ICP) algorithm, 3) nonrigid registration with a thin-plate spline based ICP algorithm. The outputs of this centerline registration are a rigid transformation T_{init} and a nonrigid transformation $T_{centerline}$, which are used as initialization and constraint, respectively, in the joint intensity-and-point based registration (Figure 3.1).

3.2.2.1 Centerline Extraction

First, the centerline is extracted in both images. We use different algorithms to track the centerline in MRI and US. Both algorithms are initialized with three seed points. Seed points should be located in the lumen, in the CCA, ICA and ECA. Seed point selection is the only interaction required in the entire registration procedure. The algorithm does not require the user to identify which centerline is ICA or ECA. Nevertheless, we use the terms ICA and ECA in the method's description in order to address the bifurcations with the standard nomenclature.

The MRI centerline algorithm employed [74] tracks the minimum cost path between the seed point in the CCA and other the two other seed points. The costs assigned to a centerline for passing through a particular voxel are computed based on the local intensity and medialness [76]. The minimum cost path algorithm is iteratively applied after curved multi-planar reformatting to avoid large deviations of the true vessel centerline in curved regions. The method results in one centerline connecting the CCA point to the ICA point, and one centerline connecting the CCA point to the ECA point.

The US centerline extraction algorithm is an improved version of a previously developed method [75]. The algorithm assumes that planar cross-sections of the lumen have an approximate ellipse shape. The method estimates the centerline by fitting ellipses in lumen cross-sections. In order to fit the ellipses, points are localized in the lumen border, by casting a set of rays from a given seed point inside the lumen, up to a position outside the lumen. Whereas in the original method [75] a threshold on

the pixel intensities was used to identify the position where the rays intersected the lumen boundary, in the current work we used a more robust edge detection based on directional gradients in each cross section. The threshold is calculated by taking the third quartile of the directional image gradients within a circle with radius of $2\,cm$ around the seed point. Pixels outside this range would not contribute to the border identification; mainly they would be outside the ultrasound image field of view. It was visually confirmed that this extension increases the method's robustness against noise and intensity variations in the arterial lumen between slices. The algorithm can deal with noise inside the lumen, and partially missing border information in the US data.
A post-processing step follows the centerline extraction. The MRI and US centerlines are smoothed and resampled to a resolution of $0.1\,mm$ (slightly smaller than the voxel spacing of the US image data), resulting in point sets u and m. Thereafter, the bifurcation point P_B is defined as the point where the distance between ICA and ECA becomes larger than 1 mm. Based on P_B, the centerlines are subdivided in parts representing the common, internal and external carotid artery.

3.2.2.2 Point-Based Rigid Registration

The first step of the alignment is a rigid registration based on a set of corresponding points from both centerlines. Point selection is based on geometrical considerations. The corresponding points are selected around P_B. In order to define corresponding points which lie inside the field of view of the images, two spheres S_5 and S_{10}, with radius of $5\,mm$ and $10\,mm$, and P_B as their center are defined (Figures 3.3c and 3.3d). The choice of a maximum radius of $10\,mm$ is related to the image acquisition. The closest points to the sphere borders on each of the CCA, ECA and ICA centerlines are calculated. Since we do not assume knowledge on which vessel is ICA and which one is ECA, and since the carotid artery bifurcation is (more or less) symmetric about its longitudinal axis, a misregistration of 180° may very well occur if we would only use these points on the centerlines for alignment. To resolve this ambiguity, we also define a vector $\overrightarrow{v_{skin}}$ which originates in P_B and points towards the skin of the patient. The two points where this vector intersects S_5 and S_{10} are used as additional landmarks, making 9 landmarks in total. In US images, the position of the skin is always on the top and parallel to the X-axis. For MRI, if the vessel is located on the left half of the image, the vector should point to the left, otherwise to the right. The vector $\overrightarrow{v_{skin}}$ is defined as the cross-product between vectors $\overrightarrow{P_BP_{ECA}}$ and $\overrightarrow{P_BP_{ICA}}$: $\overrightarrow{v_{skin}} = \pm\overrightarrow{P_BP_{ECA}} \times \overrightarrow{P_BP_{ICA}}$, where the points P_{ECA} and P_{ICA} are the most distant points from P_B in the ECA and ICA centerlines, respectively, and where the sign is determined such that the vector points upwards in the US image and left or right in MRI according to the side of the artery**.** Commonly, the positional relationship of ICA and ECA is parallel to the skin and this definition is a robust estimator of the skin direction. We define this condition as anatomical configuration 1, shown in Fig. 3.3a and Fig. 3.3c. However, in a small percentage of the cases, the positional relationship of ICA and ECA is orthogonal to the skin, a position defined as *medial* [77]. To detect these cases, we calculate the angle ϕ between $\overrightarrow{v_{skin}}$ and the X-axis in the US image. In the case of ϕ smaller than 15°, we consider that a more robust estimation

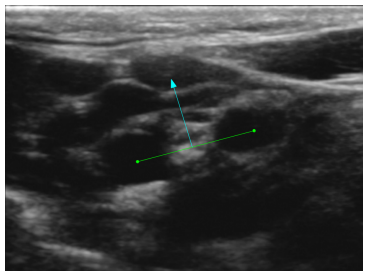

(a) Anatomical configuration 1 as seen on US.

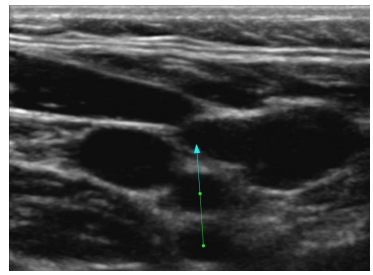

(b) Anatomical configuration 2 as seen on US.

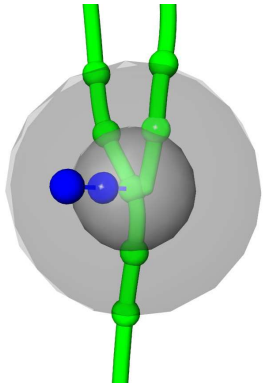

(c) Geometry for anatomical configuration 1.

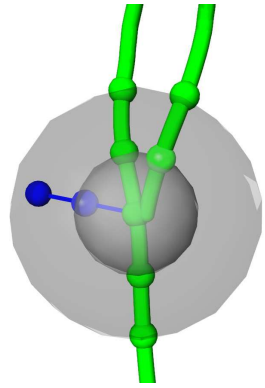

(d) Geometry for anatomical configuration 2.

Figure 3.3: Illustration of the two anatomical configurations of the carotid artery, which differ in the orientation of ICA and ECA relative to the skin (more parallel or more perpendicular, respectively). The blue line represents the vector $\overrightarrow{v_{skin}}$, the green dots are points in ICA and ECA, and the gray spheres are S_5 (inner) and S_{10} (outer).

of the skin direction is: $\overrightarrow{v_{skin}} = \pm\overrightarrow{P_{ICA}P_{ECA}}$. We call this anatomical configuration 2, which is shown in Fig. 3.3b and Fig. 3.3d.

A point-based rigid registration is performed with the above defined 9 pairs of corresponding landmarks. This point-based registration minimizes the sum of squared Euclidean distances between corresponding points. The output transformation is called T_0 and it is applied to u. Following this registration, the point sets u and m are cropped automatically such that the maximum distances before/after the bifurcation in the one set are equal to those in the other set.

3.2.2.3 Iterative Closest Point Registration: Rigid and Nonrigid

Following the point-based rigid registration, the point set u is registered to m by an Iterative Closest Point (ICP) rigid registration [67], resulting in transformation T_1; followed by a nonrigid thin-plate-spline (TPS) based ICP registration, leading to transformation T_2. The composition of the three transformations T_0, T_1 and T_2 is defined as $T_{centerline}$ and is applied to the centerline to the centerline u, yielding a deformed centerline $\tilde{u}$ that closely matches m:

$$T_{centerline} = T_2(T_1(T_0)) \quad , \quad \tilde{u} = T_{centerline}(u) \tag{3.1}$$

This transformation will be used in the next joint intensity-and-point based registration stage as a constraint. The transformations T_0 and T_1 are rigid transformations and thus will most likely provide a reasonable alignment of the entire image. The nonrigid transformation T_2 is only reliable for points on the centerline. Therefore, to globally initialize the joint intensity-and-point based registration in the next phase, we use:

$$T_{init} = T_1(T_0) \tag{3.2}$$

3.2.3 Joint Intensity-and-Point Based Registration

Prior to the joint intensity-and-point based registration, some preprocessing operations are performed on the images. Two masks are created using the centerline points for each modality. Every point in the centerline is taken as the center of a circle with a radius of $10\,mm$. The interpolation of these circles, leads to volumetric masks which are used in the registration. The goal of the mask is to exclude information which does not belong to the carotid artery. The images are cropped around the axis-aligned bounding boxes of the masks. Finally, we apply the N4 bias correction [78] to the cropped MRI in order to increase homogeneity.
In the joint intensity-and-point based registration, an image transformation T is estimated by minimizing a cost function C:

$$C(T) = \omega_1 D\left(T|U, M\right) + \omega_2 E\left(T|u, \tilde{u}\right) \tag{3.3}$$

The cost function is a function of the transformation T, and is defined as a weighted sum of the image intensity dissimilarity D and the distance between the lumen centerlines E. By minimizing C, the registration converges to a better alignment. The E term serves as a soft constraint that keeps the deformation of the lumen centerlines close to the result $\tilde{u} = T_{centerline}(u))$ of the initial point-based registration, thus preventing unfeasible transformations that may result from intensity-based registration alone. The terms ω_1 and ω_2 are user-defined weighting factors.
The optimization is performed in two stages: rigid and nonrigid. The final output transformation is composed by the initial global (rigid) transformation T_{init} (as defined in Equation 3.2), a refined rigid transformation T_{rigid} (estimated in the first registration stage), and a nonrigid B-spline transformation $T_{nonrigid}$ (estimated in the second registration stage):

$$T = T_{nonrigid}(T_{rigid}(T_{init})) \tag{3.4}$$

The image-based term D in Equation 3.3 measures the dissimilarity between the original US image and the deformed MRI. We consider two metrics for D: the Correlation Ratio (CR) and the Mutual Information (MI). Mutual Information [79,80] is known to be able to handle images from different modalities. It is based on the joint histogram of intensities in the images to be registered. In MRI, the anatomical structures tend to have a homogeneous image intensity. In US, the intensities are brighter in the transitions between tissues, consequently, the US images highlight the contours of the structures [81]. Therefore, there may not be a clear relation between the voxel intensity distributions of US and MRI. The Correlation Ratio was proposed in [81] to address this issue. It allows to incorporate both intensity and gradient magnitude information from the MR image, and estimates a transfer function from MRI to US using linear regression. Both CR and MI are evaluated in our work (Section 3.3).
The point-based term E in Equation 3.3 is defined as the average of the Euclidean distances between the corresponding point pairs in $T(u)$ and $\tilde{u}$, in equation 3.5 with u_i a point on the centerline u. The inclusion of E in the cost function C thus acts as a constraint that penalizes large deviations from the initial $T_{centerline}$ transformation at the points on the US centerline.

$$E = 1/N \sum_{i=1}^{N} \|T(u_i) - \tilde{u}_i\| \tag{3.5}$$

We also define a non-automated reference method, which uses the lumen segmentations for the registration instead of the original images. These lumen segmentations were made manually for US and semi-automatically for MRI (see Subsection 3.3.2). In this case we define D as the mean squared difference between the binary images that represent the segmentations. The goal of these experiments was to determine the maximum achievable registration accuracy. We refer to this method as "MAX". Since MAX uses the manually annotated ground truth as input, it is expected that it outperforms the other methods.
In the joint intensity-and-point based method, the weighting factors ω_1 and ω_2 control the trade-off between intensity-based and point-based information. In Section III, we test a range of values for these parameters.

3.2.4 Framework Implementation

We use the publicly available GMMREG [82] implementation to calculate T_1, using the TPS-RPM algorithm developed by Chui and Rangarajan [83] for the thin-plate spline registration (T_2). Points at $\delta = 1\,mm$ intervals sampled on the MRI centerline are used as thin-plate spline control points. In the rigid registration, for the scale parameters of Gaussian mixtures, we use values of σ of 0.5 and $0.1\,mm$, from coarse to fine. In the nonrigid registration, we use as input parameters: $r = 0.90$ (annealing rate, for the annealing schedule of the energy minimization), and $\lambda = 1$ (regularization parameter).

The joint intensity-and-point registration is implemented using the open source Elastix software [84]. A stochastic gradient descent optimization method [85], using 2000 iterations is employed to find T_{rigid} and $T_{nonrigid}$ that minimize the cost function. A 3-level hierarchical strategy is employed to avoid local minima: the amount of image smoothing (Gaussian kernel standard deviation) and the isotropic control point spacing of the B-spline transformation are gradually decreased (by factors of 2). The spacing between control points at the finest level is a user-defined parameter, β, for which a range of values was tested (see Section 3.3). To compute the mutual information, a 32×32 joint histogram is estimated using a Parzen windowing approach [86], based on 2000 image samples randomly selected in every iteration [85]. Linear interpolation is used to evaluate the MR image intensities at non-grid positions.
The user interaction and interface between the software packages is handled by MeVisLab. The code is written in Python, C++ and Unix Shell.

3.3 Experiments

3.3.1 Data

US and MR images of both carotid arteries of 6 healthy volunteers and 5 diseased patients patients were acquired. All scannings were performed with subjects' consent. Both left and right artery were scanned. For the US examinations a Philips iU22 machine was used with a Philips L9-3 probe. In order to obtain a three-dimensional US image of the carotid artery, an external tracking sensor was attached to the probe during the examination and a third party software called Stradwin [87] was used to perform the volumetric reconstruction with images obtained from the video signal output of the US machine.
For the volunteer MRI examinations, a $1.5T$ GE Medical System Signa Excite MRI machine was used, with a proton-density-weighted fast spin echo (PDw-FSE), black-blood sequence. The patient MRI data were acquired on a $3.0T$ GE Medical Systems Discovery MR750, using a a T2-weighted double inversion recovery fast spin echo (T2w-DIR-FSE), black-blood sequence. We separate our subjects in a training and a test set, to evaluate the robustness and accuracy of the algorithm in an independent data set. Specifications of the image characteristics are in Tab. 3.1.

3.3.2 Evaluation Measures

For validation, we applied the output transformations of the registrations to segmentations of the lumen in MRI and measured their similarity with manually delineated segmentations of the lumen in US. For the MRI segmentations we used the algorithm of Tang et al. [88]. As this algorithm expected approximately isotropic image resolution, we resampled the MRI with a cubic B-spline interpolation leading to isotropic voxels with spacing $0.55 \times 0.55 \times 0.55\, mm^3$. On the US, the lumen was manually delineated by making annotations on 2D slices. At every five to ten slices, one slice was selected and the lumen was annotated. A B-spline surface was constructed from these annotations. In order to quantify the registration accuracy we computed the overlap between the registered segmentations using the Dice similarity coefficient (DSC) [89]

	US Field of View	US Voxel Resolution	MRI Voxel Resolution	MRI Sequence
1 patient	$38 \times 40\,mm^2$	$0.21 \times 0.21 \times 0.21\,mm^3$	$0.55 \times 0.55 \times 2.0\,mm^3$	T2w-DIR-FSE
2 patients	$38 \times 30\,mm^2$	$0.16 \times 0.16 \times 0.16\,mm^3$	$0.55 \times 0.55 \times 2.0\,mm^3$	T2w-DIR-FSE
5 volunteers	$38 \times 30\,mm^2$	$0.16 \times 0.16 \times 0.16\,mm^3$	$0.5 \times 0.5 \times 0.9\,mm^3$	PDw-FSE

(a) Training Set

	US Field of View	US Voxel Resolution	MRI Voxel Resolution	MRI Sequence
2 patients	$38 \times 40\,mm^2$	$0.21 \times 0.21 \times 0.21\,mm^3$	$0.55 \times 0.55 \times 2.0\,mm^3$	T2w-DIR-FSE
1 volunteer	$38 \times 30\,mm^2$	$0.16 \times 0.16 \times 0.16\,mm^3$	$0.5 \times 0.5 \times 0.9\,mm^3$	PDw-FSE

(b) Test set

Table 3.1: Data specification

and the mean shortest distance between surface points (mean surface distance, MSD), which are often used measures for evaluating image registration methods, see for example [90].

3.3.3 Evaluation Procedure

For the volunteers and patients in the training set, a large number of registrations were performed, extensively evaluating different configurations of the method:

- All experiments were performed both with MI and CR as image dissimilarity measure, and using the reference approach MAX.

- To investigate the relative importance of the image-based and point-based terms D and E, we varied the weight ω_1 while keeping $\omega_2 = 1$ (as only the ratio ω_1/ω_2 is of importance). We varied the weight factor ω_1 in a power of 10 scale. With MI the weight varied from 0.0001 to 10, whereas with CR and in the MAX method the weight varied from 1 to 10000, since the typical metric value with MI was smaller than with CR and MAX (as observed in initial trial-and-error experiments). We also evaluated the extreme values $\omega_1 = 0$ (ignoring the image-based term) and $\omega_1 = \infty \Leftrightarrow \omega_2 = 0$ (ignoring the point-based term).

- Different degrees of freedom of the transformation model were evaluated. We tested both rigid registration (limiting the joint intensity-and-point based registration to the first stage estimating only T_{rigid}) and nonrigid registration (employing the proposed two-stage approach estimating first T_{rigid} and then $T_{nonrigid}$). The B-spline control point spacing β determines the freedom of deformation in the nonrigid registration; we tested β values of 40, 32, 16, 8 and $4\,mm$.

Paired t-tests were performed to assess the statistical significance of differences between the results of the optimal configuration and the other configurations.
Finally, to evaluate the robustness of the algorithm, the best performing method on the training set was evaluated on the previously unseen test set.

3.4 Results

Figures 3.4 and 3.5 visualize the registration accuracies for different parameter configurations of the method using CR (left), MI (middle), and using the reference method MAX (right). Figure 3.4 presents the results in terms of DSC and Figure 3.5 in terms of MSD. The colors of the bars indicate if the registration was rigid or nonrigid with B-spline control point spacing β. The results of configurations that led to the highest DSC and the smallest MSD are reported in Tables 3.2a and 3.2b.

The proposed method achieved an average DSC of 0.74 (CR) and average MSD of $0.66\,mm$ (CR) on the volunteers set. On the patients set, the best average DSC was 0.77 (MI) and the average MSD was $0.69\,mm$ for both CR and MI. The best configuration with CR in the volunteers set ($\omega_1 = 10000, \beta = 8\,mm$) scored an average DSC of 0.74, however the same configurations performed poorly in the patients set considering its DSC of 0.68 and MSD of $1.34\,mm$. With a larger grid spacing $\beta = 32\,mm$ the results were more stable. The best configuration with MI in both volunteer and patient sets was also obtained with $\beta = 32\,mm$. Both in the volunteer and patient set, the initial point-based registration provided a robust initial alignment. The subsequent joint intensity-and-point based approach in its best configuration resulted in a modest, but consistent improvement on the initial alignment. For CR, the best weight ω_1 was 10000. For MI, the best weight was between 1 and 10. Both with CR and MI, the joint intensity-and-point based approach thus outperformed the extreme configurations $\omega_1 = 0$ (ignoring the image-based term) and $\omega_2 = 0$ (ignoring the point-based term). For further experiments, we select the configuration with CR, $w_1 = 10000$, and $\beta = 32\,mm$ as the optimal method, as it gives consistently good results.

The MAX approach, which uses the segmentations instead of the original images, reached an average DSC of 0.91 and an average MSD of $0.23\,mm$ on the volunteer set and a DSC of 0.91 and MSD of $0.21\,mm$ on the patient set, indicating the maximum theoretically achievable accuracies. These results were obtained with the smallest investigated B-spline grid spacing of $4mm$ and with $\omega_1 \geq 1000$.

Figure 3.6 show the contours of the segmentations in an example slice for the proposed method with CR and MI, and for the reference method MAX. Figure 3.7 shows three-dimensional examples of US and MRI lumen surfaces overlaid after registration.

Paired t-tests were performed to assess the DSC and MSD differences between the optimum configuration and the other settings. CR was used in all experiments as dissimilarity measure. In the first experiment ω_1 was fixed to 10000 and the results with different settings of β were compared with the optimum $\beta = 32\,mm$. In the second experiment, β was fixed to $32\,mm$, and the results with different settings of ω_1 were compared with the optimum $\omega_1 = 10000$. In these tests, we pooled the results of patients and volunteers. Figure 3.8 shows the results. Statistically significant ($p < 0.05$) differences were found with respect to rigid registration, highly nonrigid registration ($\beta \leq 8mm$), and purely intensity based registration ($\omega_1 = \infty$).

The experiments on the test set use the optimal configuration and are shown in Tab. 3.3. These results are similar to results on the training set.

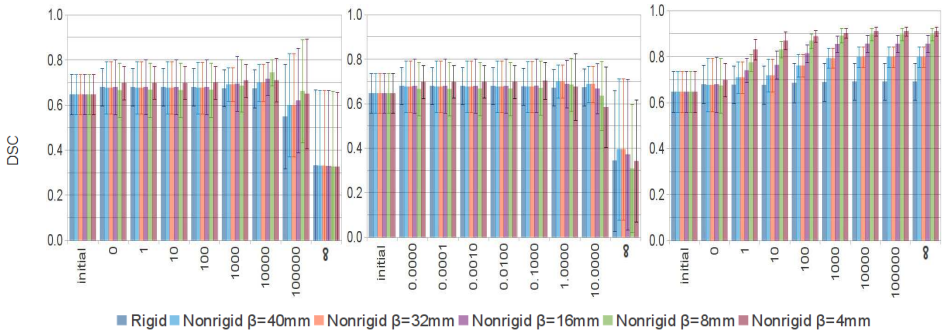

(a) CR, MI and MAX. Volunteer dataset.

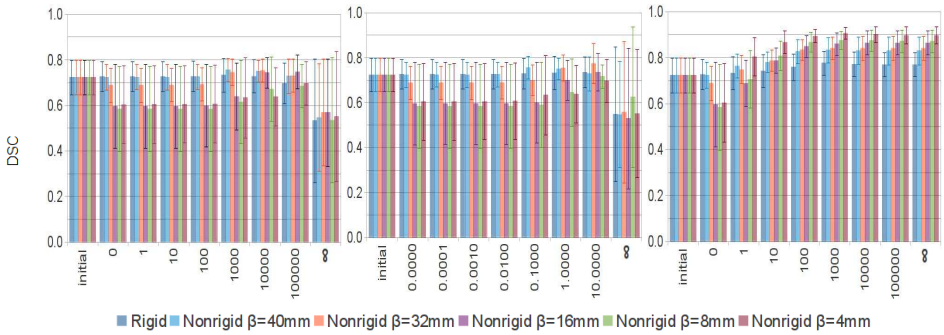

(b) CR, MI and MAX. Patient dataset.

Figure 3.4: Registration accuracies evaluated with the Dice Similarity Coefficient, using CR (left), MI (middle), and using the reference method MAX (right). The label *initial* on the X-axis means that only the transformation T_{init} was applied; the following values correspond to ω_1. The colors represent the different transformation models: rigid or nonrigid with control point spacings β of 40, 32, 16, 8 and 4 mm.

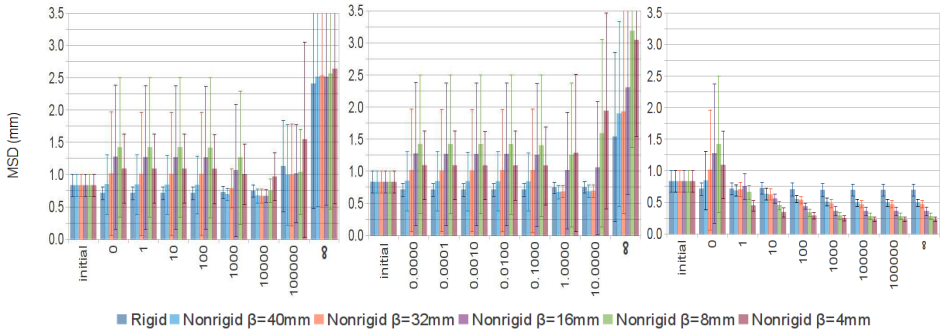

(a) CR, MI and MAX. Volunteer dataset.

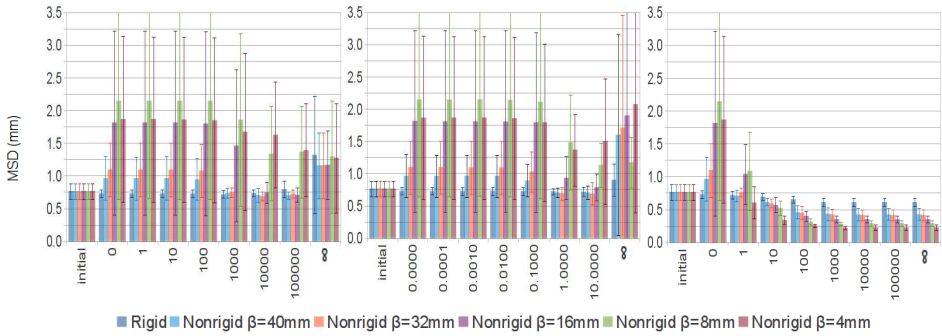

(b) CR, MI and MAX. Patient dataset.

Figure 3.5: Registration accuracies evaluated with the Mean Surface Distance (in mm), using CR (left), MI (middle), and using the reference method MAX (right). The label *initial* on the X-axis means that only the transformation T_{init} was applied; the following values correspond to ω_1. The colors represent the different transformation models: rigid or nonrigid with control point spacings β of 40, 32, 16, 8 and 4 mm.

	DSC	MSD
CR	$0.74\pm0.06, \omega_1 = 10000, \beta = 8\,mm$	$0.66\pm0.11\,mm, \omega_1 = 10000, \beta = 32\,mm$
MI	$0.70\pm0.07, \omega_1 = 1, \beta = 32\,mm$	$0.68\pm0.10\,mm, \omega_1 = 1, \beta = 32\,mm$
MAX	$0.91\pm0.02, \omega_1 = \infty, \beta = 4\,mm$	$0.23\pm0.04\,mm, \omega_1 = \infty, \beta = 4\,mm$

(a) Volunteer dataset.

	DSC	MSD
CR	$0.75\pm0.05, \omega_1 = 10000, \beta = 32\,mm$	$0.69\pm0.07\,mm, \omega_1 = 10000, \beta = 32\,mm$
MI	$0.77\pm0.09, \omega_1 = 10, \beta = 32\,mm$	$0.69\pm0.10\,mm, \omega_1 = 1, \beta = 32\,mm$
MAX	$0.91\pm0.03, \omega_1 = 1000, \beta = 4\,mm$	$0.21\pm0.02\,mm, \omega_1 = 1000, \beta = 4\,mm$

(b) Patient dataset.

Table 3.2: Best registration results for both evaluation criteria.

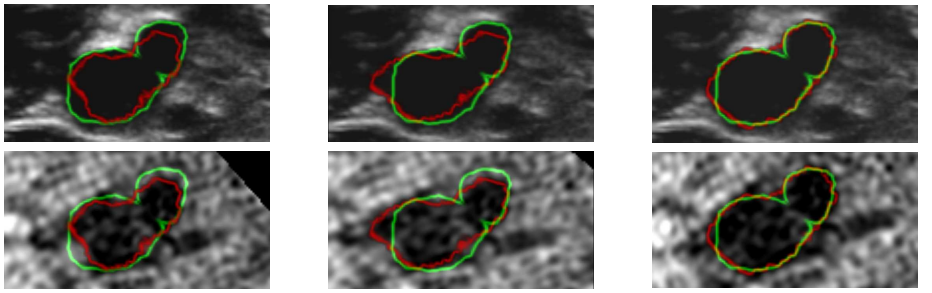

(a) CR, $\omega_1 = 10000$, $\beta = 32\,mm$ (b) MI, $\omega_1 = 10$, $\beta = 32\,mm$ (c) MAX, $\omega_1 = 1000$, $\beta = 8\,mm$

Figure 3.6: US slice (top) and MRI slice (bottom) of the left carotid after registration. The areas delineated by the red line represent the MRI segmentation after the transformation. The areas in green represent the US manual segmentation.

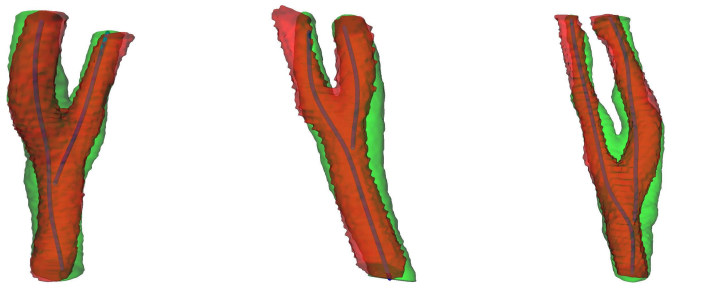

(a) Volunteer A, left (b) Volunteer C, right (c) Volunteer E, left

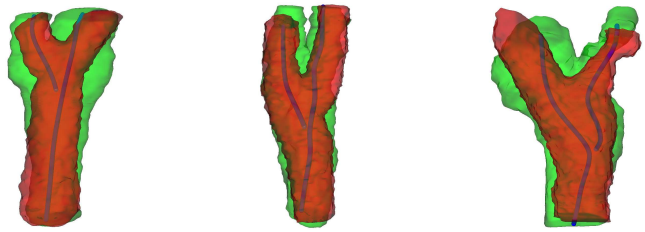

(d) Patient A, left (e) Patient B, right (f) Patient C, left

Figure 3.7: Example isosurfaces of the lumen segmentations, obtained with CR as similarity metric, $\omega_1 = 10000$, $\omega_2 = 1$ and $\beta = 32\,mm$. Green: US segmentation; red: transformed MRI segmentation; blue: US centerline.

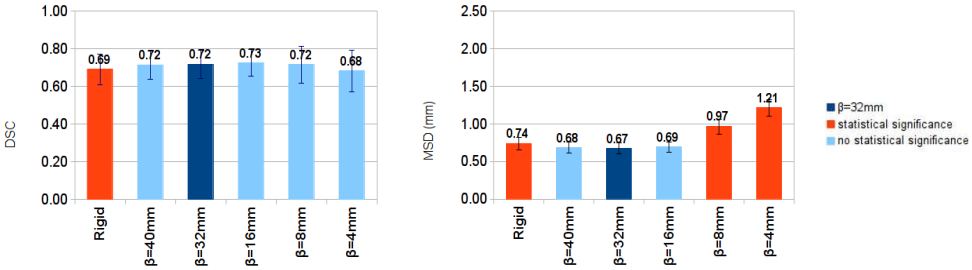

(a) The configuration CR, $\beta = 32\,mm$, $\omega_1 = 10000$, $\omega_2 = 1$ was compared against the other values assumed by β and against the rigid registrations.

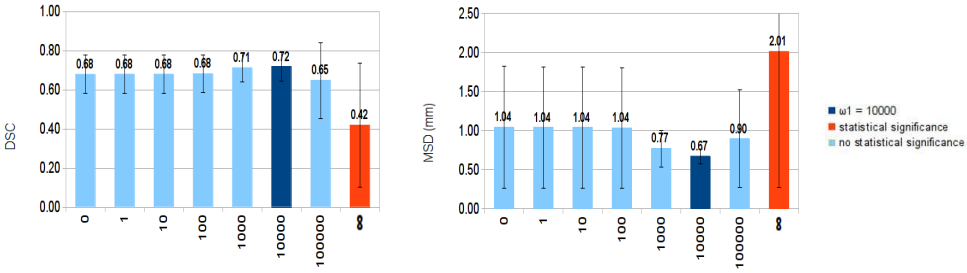

(b) The configuration CR, $\beta = 32\,mm$, $\omega_1 = 10000$, $\omega_2 = 1$ was compared against the other values assumed by ω_1 and ω_2.

Figure 3.8: Results of statistical analysis on the training set, pooling patient and volunteer data. The graph color indicates statistically significant ($p < 0.05$) differences with respect to the optimal configuration, CR, $\beta = 32\,mm$, $\omega_1 = 10000$, $\omega_2 = 1$. a) The effect of the transformation model is investigated; b) the effect of $\omega_1 = 10000$ is investigated. Results are shown in terms of DSC (left) and MSD (right).

	DSC	MSD (mm)
Patient D, left	0.84	0.95
Patient D, right	0.66	0.86
Patient E, left	0.64	1.25
Patient E, right	0.61	0.92
Volunteer F, left	0.67	0.75
Volunteer F, right	0.73	0.49
Average	0.69±0.08	0.87±0.25

Table 3.3: Results on the test set using the optimal configuration CR, $\omega_1 = 10000$, $\omega_2 = 1$ and $\beta = 32\,mm$.

3.5 Discussion and Conclusion

This work presented a semi-automatic method for the registration of US and MRI data of the carotid artery. The joint intensity-and-point based registration minimizes a cost function that considers the dissimilarity of pixel intensities and the distance between extracted lumen centerlines. Rigid and nonrigid registration are applied. The only required manual inputs are the three seed points on each image modality for the centerline extraction. Two evaluation criteria were employed to assess the registration accuracy and a (non-automated) reference approach was implemented in order to verify what would be the maximum achievable registration accuracy. The influence of several important parameters was studied: we investigated the relative importance of the image-based and point-based terms in the framework, evaluated the required degrees of freedom for the transformation model, and compared two image similarity measures that were previously proposed for multimodal image registration. Finally, the method in its optimum configuration was evaluated on an independent test set.

3.5.1 Joint Intensity-and-Point Based Registration

The role of geometrical landmarks appeared to be essential for obtaining an accurate registration. The initial point-based registration achieved a reasonable initial alignment in all cases, without prior knowledge about which of the vessels is ICA or ECA. In the subsequent joint intensity-and-point based registration, the combination of image intensity information and point correspondence led to better registrations than purely point-based ($\omega_1 = 0$) or purely intensity-based ($\omega_2 = 0$) approaches. The two evaluated image similarity terms CR and MI resulted in similar registration accuracies. The use of nonrigid registration improved the registration accuracy in comparison with the rigid registrations. A relatively coarse B-spline control point grid spacing of $\beta = 32\,mm$ gave accurate yet robust results, allowing to compensate for the differences in the positions of the neck during US and MRI examination.

3.5.2 Maximum Achievable Registration Accuracy

In the MAX experiments, the use of the lumen segmentations clearly improved the registration accuracy. However, such approach is biased, since it uses information (ground truth lumen segmentations) that was also used in the evaluation criterion. The results of the MAX experiments thus provide an upper bound for the accuracy that may be obtained. The difference in performance between this experiment and the other experiment indicates that there is still room for improvement. Using automated lumen segmentations on US and MRI would be an interesting research direction. Robust automated lumen segmentation on 3D B-mode US will be the main challenge in such an approach.

3.5.3 Comparing with Results in Literature

The method of Chiu et al. [66] was reported to yield an average error between $0.33\,mm$ and $0.87\,mm$ on data acquired from 3 patients. The registration accuracy was computed by calculating the average distance between closest points on the outer-wall surfaces of the MRI and registered US. This evaluation measure is comparable to the MSD, used in our experiments. The method of Nanayakkara et al. [65] resulted in an average registration error of $1.4 \pm 0.3\,mm$ for $1.5\,T$ MR and $1.5 \pm 0.4\,mm$ for $3.0\,T$ MR on data acquired from 6 patients. The evaluation measure was the average distance between corresponding pairs of points selected in radial sections on the outer-wall surfaces of the US and registered MRI. This measure will tend to generate larger error values than surface distance measures based on closest points. Our method provides competitive results regarding the methods in the literature, with an average registration accuracy of $0.69\,mm$ for the patients in the training set and $0.87\,mm$ in the test set. However, the three methods were applied to different datasets with slightly different measures to calculate the registration accuracy. Therefore the comparisons have to be interpreted with care.

3.5.4 Conclusion

Semi-automatic registration of US and MRI carotid artery data was achieved with an average DSC of around 0.75 and an MSD around $0.8mm$. The performance was consistent across healthy volunteers and atherosclerotic patients, and results on the training set could be reproduced on an independent test set. We used imaging data with different specifications, acquired with two MRI scanners and with the beam of the US probe adjusted to two different depths. The method proved to be robust regardless these different scanning conditions. Two conclusions can be drawn from the experiments on the training set: 1) The use of nonrigid registration yields better results than rigid registration. 2) Joint intensity-and-point based registration generates better results than registration with intensity or points only. These conclusions hold both in volunteer and patient data. There is room for improvement as the registration performed directly on the ground truth lumen segmentations still performed better. Still, we feel our work provides the foundations for an automated US - MRI carotid registration allowing multimodal analysis of the atherosclerotic carotid plaque.

4

Automated Registration of Free-hand B-mode Ultrasound and MRI of the Carotid Arteries Based on Geometrical Features

Abstract: In this work an automated method to register B-mode Ultrasound (US) and Magnetic Resonance Imaging (MRI) of the carotid arteries is proposed. The registration uses geometrical features, namely lumen centerlines and lumen segmentations, which are extracted fully automatically from the images after manual annotation of three seed points in US and MRI. The registration procedure starts with aligning the lumen centerlines using a point based registration algorithm. The resulting rigid transformation is used to initialize a rigid and subsequent nonrigid registration procedure that jointly aligns centerlines and segmentations, by minimizing a weighted sum of the Euclidean distance between centerlines and the dissimilarity between segmentations. The method was evaluated in 28 carotid arteries, from 8 patients and 6 healthy volunteers. We first validated and optimized the automated US lumen segmentation method in a cross-validation experiment. Next we evaluated the effect of two important design parameters of the registration method. Finally, the proposed registration method was evaluated in comparison to the intensity-and-point based method that was proposed in Chapter 3. Registration accuracy was measured in terms of the mean surface distance (MSD) between manual US segmentations and the registered MRI segmentations. The average (± std.dev.) MSD was $0.78 \pm 0.34\,mm$ for all subjects, $0.65 \pm 0.09\,mm$ for healthy volunteers, and $0.87 \pm 0.42\,mm$ for patients. The results on the complete set were significantly better (Wilcoxon test, $p < 0.01$) than the results of the intensity-and-point based method. We conclude that the proposed method can robustly and accurately register US and MR images of the carotid artery, allowing multimodal analysis of the carotid plaque in order to improve plaque assessment.

Based upon: **Diego D.B. Carvalho***, Andrés M.A. Lorza*, Wiro J. Niessen, Marleen de Bruijne, Stefan Klein, "Automated Registration of Free-hand B-mode Ultrasound and MRI of the Carotid Arteries Based on Geometrical Features", submitted
*both authors contributed equally to this research

4.1 Introduction

Cerebrovascular disease ranks as the third worldwide leading cause of death [91]. The brain and muscles of the face are supplied with blood by a pair of vessels called the carotid arteries which are located in the neck. Atherosclerosis in the carotid arteries is one of the conditions that can cause cerebrovascular disease. Atherosclerosis is a process of inflammation in the arterial wall, leading to the formation of a plaque. Rupture of atherosclerotic plaques in the carotid artery can cause vessel obstruction and distal propagation of a thrombus [92] which may result in an ischemic stroke [60]. The risk of plaque rupture is associated with plaque composition and morphology [61]. Imaging thus could play a key role in estimation of plaque rupture risk.
Different imaging modalities supply complementary information on the carotid artery wall and plaque therein, leading to interest in multimodal imaging studies on the assessment of atherosclerosis and plaque vulnerability [33, 34, 93]. Even though most imaging modalities show the lumen and artery wall, each one emphasizes different properties: angiography is especially useful to visualize the stenosis severity; Computed Tomography (CT) visualizes plaque calcifications well; Magnetic Resonance (MR) shows intra-plaque haemorrhage, and necrotic cores; Ultrasound (US) shows echolucency and ulceration. US and MRI modalities are of special interest, since they do not involve any ionizing radiation, and US is a relatively low-cost modality. Fig. 4.1 shows example slices of a free-hand transversal B-mode US scan and an MRI scan of the same patient.

Comprehensive multi-modal image analysis and side-by-side visualization of different imaging modalities is hampered by the lack of spatial correspondence between images, as depicted in Fig. 4.1. Besides global differences due to different image resolution, field-of-view, and orientation, there may even be changes in the artery geometry due to bending and twisting of the neck (as is typically required for US acquisition). Differences in patient's neck position in US and MRI can be appreciated from Fig. 4.2. Image registration is therefore required, to align the carotid arteries and compensate for deformations. Since US and MRI have very different image appearance, the registration of these images is a highly challenging problem.

MRI-US registration of the carotid artery has been addressed in previous works [63, 65, 66, 94]. Slomka et al. [63] presented the registration of 3D reconstruction of free-hand power doppler US (3D-US) and Magnetic Resonance Angiography (MRA) images. The vessel lumen is clearly visible in both modalities, and therefore it was used to drive the registration. The method uses a rigid transformation model, and is based on maximization of mutual information. The method was evaluated on data of six patients. Nanayakkara et al. [65] used a constrained nonrigid transformation model to register 3D-US and MRI. First an initial registration was performed based on geometrical landmarks; subsequently the images were registered using normalized mutual information as registration metric. 3D US acquisition was performed with a motorized device attached to the probe, which generated a sequence of 2D B-Mode US images. They evaluated the registration method on images from six patients. Chiu et al. [66] performed registration using points on the arterial outer wall. These points were extracted from a manual segmentation in MRI and a semi-automated

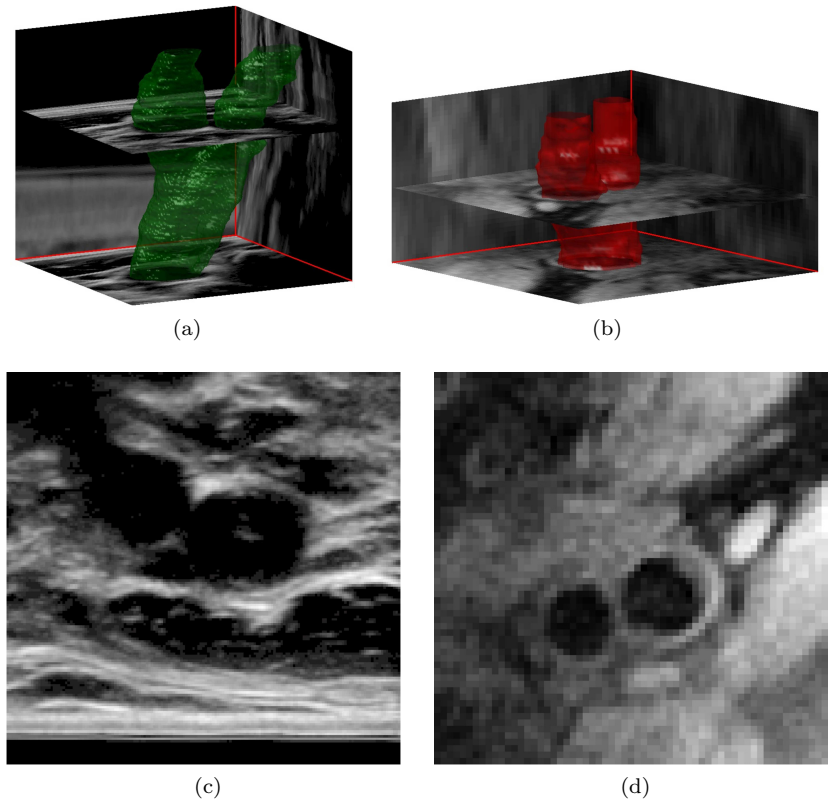

Figure 4.1: Multimodal carotid artery imaging. A 3D reconstruction of a free-hand transversal B-mode US scan is shown in (a), and an MRI scan of the carotid artery of the same patient is shown in (b) The green and red volumes represent the artery in both modalities. 2D slices intersecting the arteries taken at similar positions close to the bifurcation on both images are shown in (c) and (d).

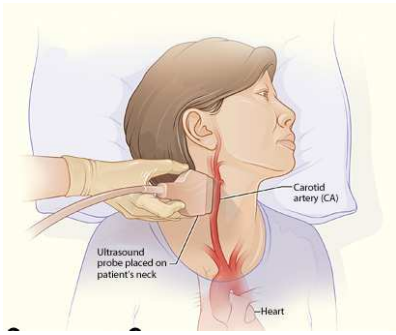

(a) source: Adapted from Wikimedia. Author: National Heart Lung and Blood Insitute (NIH)

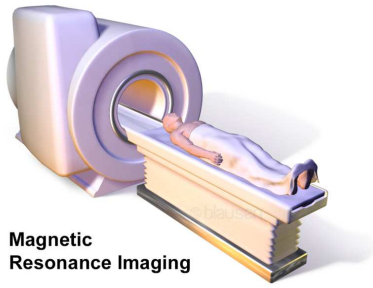

(b) source: Wikimedia. Author: Blausen Medical Communications, Inc.

Figure 4.2: Position of the patient's neck during US (left) and MR (right) scanning.

segmentation in US. The artery bifurcation point was used to obtain an initial alignment, which was followed by a rigid registration of the outer wall point sets using the Iterative Closest Point (ICP) algorithm [67]. Subsequently, a slice-by-slice manual registration refinement was performed. The method was evaluated on 3D US acquired using a volumetric linear transducer and MRI data of three patients. In our previous work [94], a framework was introduced to perform US-MRI registration using a joint intensity-and-point based registration of free-hand B-mode ultrasound and MRI data of the carotid artery. An initial registration using geometrical landmarks on the lumen centerlines was performed. Subsequently, a joint intensity-and-point based dissimilarity measure was minimized, solving both for rigid and nonrigid transformations. We showed that this registration approach combining geometrical information (lumen centerlines) and image information (US and MRI intensities) resulted in better registrations compared to intensity-only or point-only approaches. However, we also observed that even better registrations could be achieved if more geometrical information, such as carotid artery lumen segmentations, would be exploited.

In this work, we propose a novel automated method for registering US and MRI images of the carotid artery. The method is an extension of [94] and adds geometric information in the form of lumen segmentations, to improve registration performance.

Our approach thus requires segmentation of the lumen both in 3D US and MRI. Manual segmentation of the carotid lumen in 3D US and MRI images is a time consuming and difficult process. US image segmentation is challenging owing to characteristics such as noise, shadows and speckles inside the lumen. Moreover, in situations were the US beam is parallel to the vessel wall, the wall is not clearly visible. This makes it difficult to differentiate the carotid artery lumen from other structures. To facilitate carotid lumen segmentation in 3D US, several automatic and semi-automatic methods have been proposed [95–98]. A semiautomatic method for carotid segmentation in 3D US using level sets was presented by Ukwatta et al. [95]. The segmentation results were good, however the method requires substantial user interaction as anchor points

on transverse slices need to be selected which are intercepted by an evolving curve. Additionally, the method is limited to the segmentation of the common carotid artery. Another method that uses a level-set based approach for carotid artery segmentation was presented by Hossain et al. [96]. This method also requires considerable user interaction to initialize boundary points for every slice. Liu et al. [97] proposed a very robust method to track the arteries, however it is limited to generating circles per slice. In previous work [98], we applied an optimal-surface graph method to segment the lumen in 3D US. Good results were obtained on volunteer data, and fair results on patient data. Segmenting the lumen in MRI is easier compared to US because lumen contrast in MRI is generally good. However, it is also a time consuming process if performed manually. Several automatic methods to segment the lumen in MRI that achieved good results have been presented, e.g. [88, 99, 100]. In [88] a level-set evolution approach starting from an automatically detected centerline was used. Arias et al. [99] proposed an optimal-surface graph segmentation method which requires a coarse approximation of the lumen as initialization. Finally, in [100] a 3D deformable vessel model approach with a learning-based post-processing step was used.
In our US-MRI registration method, we choose to use lumen segmentation based on optimal surface graphs as presented for US in [98], and for MRI in [99]. The method is described in detail in Section 4.2.2. For MRI, the segmentation method was already extensively evaluated in [99]. For US, only a preliminary evaluation was presented in [98]. In this work, we include a thorough evaluation of the US segmentation method, to assess its feasibility for use as a reliable geometrical marker for image registration. The complete registration method is subsequently evaluated on 28 carotid artery data sets.

4.2 Method

In Section 4.2.1 we present the registration framework, and in Section 4.2.2 we describe the automated US lumen segmentation in detail.

4.2.1 US-MRI Registration Framework

Multimodal image registration is performed using geometrical features extracted from the US (I_U) and MR (I_M) images. The registration aligns the features of a *moving* image to the features of a *fixed* image by applying geometrical transformations. These transformations can be rigid or nonrigid and are determined by optimizing a cost function, which estimates the dissimilarity between the fixed image and the features of the transformed moving image. In this work we choose I_U as the fixed image because of its higher resolution.
The lumen centerlines and the segmentations are extracted from each modality and serve as input features for the registration. In the first stage of the registration procedure, the centerlines are used to obtain an initial transformation ($\boldsymbol{T}_{init}$) to align the images. Subsequently, both the centerlines and the segmentations are employed in finding the optimal transformation. An overview of the method's steps is shown in Fig. 4.3.

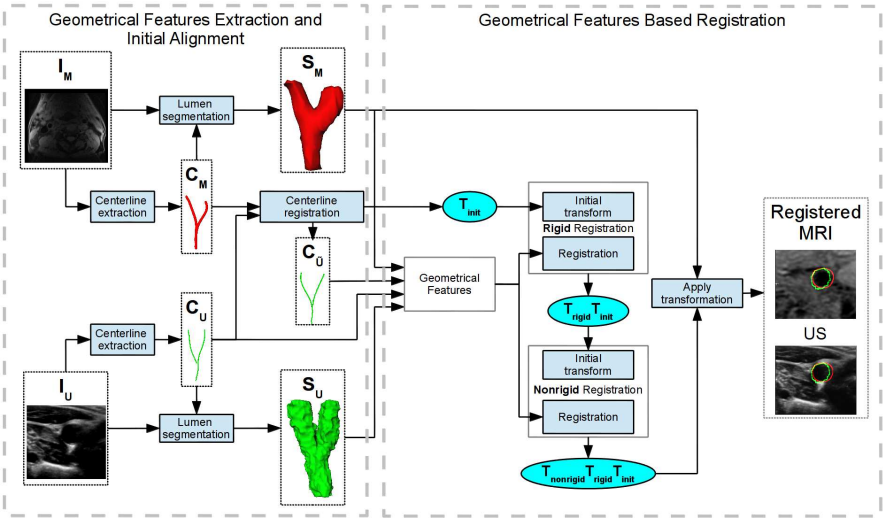

Figure 4.3: Flowchart with a schematic overview of the US and MRI registration steps.

4.2.1.1 Centerline Extraction

The centerline in US is extracted with the method of Carvalho et al. [75, 94] and the centerline of MRI is extracted with the method of Tang et al. [74].

In the centerline extraction on the US data, we assume that planar cross-sections of the lumen have elliptical shapes. The union of the center points of the ellipses in each cross-section results in the centerline. The ellipses are fitted to points on the lumen border. These border points are automatically detected by analyzing the intensity gradient magnitude in rays traced from a given seed point inside the lumen. The initial inputs of the algorithm are three seed points located at the common carotid artery (CCA), external carotid artery (ECA) and internal carotid artery (ICA). The algorithm seed point for the next planar cross-session is the center of the ellipse extracted from the previous planar cross-section.

The centerline in MRI is extracted by finding the minimum cost path between a seed point in the CCA and seed points in the ECA and ICA. This cost is computed based on a combination of a local intensity similarity metric and a medialness filter [76]. To avoid large deviations of the true vessel centerline in curved regions, a multi-planar reformatting is performed and the minimum cost path algorithm is iteratively applied.

We denote the obtained centerlines as C_U (US centerline) and C_M (MRI centerline), where C_U and C_M are sets of 3D points. The centerlines are used both for centerline registration (Section 4.2.1.2) and to initialize the lumen segmentations in US and MRI (Section 4.2.2).

4.2.1.2 Centerline Registration

To obtain a robust initial alignment, the centerlines C_U and C_M are registered. The steps for the centerline registration are the same as in [94] and are briefly summarized here for completeness.
First, the MRI and US centerlines are smoothed and resampled to a resolution of $0.1\,mm$ (slightly smaller than the voxel spacing of the US image data). Subsequently, reference points around the bifurcation point are automatically selected in each centerline. A point-based rigid registration is performed with these pairs of corresponding landmarks. This point-based registration minimizes the root sum of squared Euclidean distances between corresponding points. The output transformation is called $\boldsymbol{T}_0$ and is applied to C_U. Following this registration, the point sets C_U and C_M are cropped automatically such that the maximum distances before/after the bifurcation in both sets are equal. This registration is followed by a rigid ICP registration between the centerlines, resulting in a second rigid transformation $\boldsymbol{T}_1$. Next, the centerlines are registered with a nonrigid registration. The nonrigid transformation is applied to the US centerline, yielding a deformed centerline $C_{\tilde{U}}$ which matches the original MRI centerline C_M.
The composition of transformations $\boldsymbol{T}_0$ and $\boldsymbol{T}_1$ is used to globally initialize the geometrical features based registration: $\boldsymbol{T}_{init} = \boldsymbol{T}_1(\boldsymbol{T}_0)$. The deformed centerline $C_{\tilde{U}}$ is used as a constraint.

4.2.1.3 Geometrical Features Based Registration

In this stage of the registration, alignment is performed using both centerlines and segmentations. The lumen segmentations (S_U) and (S_M) are functions that map any coordinate $\mathbf{x} \in R^3$ to a binary value 0 or 1, $S_{\{U,M\}} : \mathbb{R}^3 \rightarrow \{0,1\}$, where we assume that some interpolation method is used to make this function valid for all $\mathbf{x}$, and not just at voxel center locations. The registration is performed by estimating a transformation $\boldsymbol{T}$, which minimizes a cost function. The geometrical features are registered with a rigid transformation $\boldsymbol{T}_{rigid}$ and a subsequent nonrigid transformation $\boldsymbol{T}_{nonrigid}$. The cost function $\mathcal{C}$ is a dissimilarity measure between the lumen segmentations S_U and S_M, and between centerlines $C_{\tilde{U}}$ and C_U:

$$\mathcal{C}(\boldsymbol{T}) = \omega\mathcal{D}(S_U, W_{\boldsymbol{T}}(S_M)) + \mathcal{E}(\boldsymbol{T}(C_U), C_{\tilde{U}}) \tag{4.1}$$

This function is a weighted sum of the segmentation dissimilarity $\mathcal{D}$ and the Euclidean distance between centerlines C_U and $C_{\tilde{U}}$, denoted by $\mathcal{E}$. The term $W_{\boldsymbol{T}}$ represents an operator that warps S_M using coordinate transformation $\boldsymbol{T}$, i.e., $(W_{\boldsymbol{T}}(S_M))(\mathbf{x}) = S_M(\boldsymbol{T}(\mathbf{x}))$. The chosen metric $\mathcal{D}$ is the sum of square differences. The Euclidean distance $\mathcal{E}$ between C_U and $C_{\tilde{U}}$ is used as a penalizer to prevent unfeasible transformations that may occur due to inconsistencies in the automated segmentations S_U and S_M. The term ω is a weighting factor.
To minimize $\mathcal{C}$, an adaptive stochastic gradient descent method [85] was applied using 2000 image coordinates randomly selected in every iteration. To model the nonrigid

transformation, a B-spline parametrization [101] was used, with a control point spacing of β. In order to avoid local minima, a 3-level hierarchical strategy was employed: the amount of image smoothing (Gaussian kernel standard deviation) and β are gradually decreased (by factors of 2). The geometrical features based registration was implemented in the Elastix software [84].

4.2.2 Optimal-surface graph method for lumen segmentation

The optimal surface graph method as proposed by Wu and Chen [102] allows segmentation of multiple surfaces, while incorporating topology constraints and prior information on shape. The optimal-surface graph method aims to minimize a cost function defined as the sum of graph edge costs, which is achieved using a minimum cut. The graph $G = (V, E)$ is composed of vertices V and edges E. V includes the vertices associated with positions in the image, and the vertices s and t which denote the source and sink points of the graph. The edges E connect the vertices of the graph, and represent the association strength between vertices. Edges that connect vertices from the same region are associated with high costs, whereas vertices connecting different regions are associated with low costs. The segmentation solution is defined by the minimum cut that separates the graph in two parts: source part $V_s \subseteq V$ (foreground region) and sink part $V_t \subseteq V$ (background region), such that $V_t = V \backslash V_s, s \in V_s, t \in V_t$. The minimum cut minimizes the total cost of the edges that are being cut [103], and is found by applying a min-cut/max-flow optimization algorithm [104] .

We use the graph construction approach as presented by Arias et al. [98] to segment the lumen in 3D US and MRI. The graph is constructed starting from a coarse initial segmentation of the lumen as depicted in Fig. 4.4. The coarse initial segmentation is obtained by a $2\,mm$ diameter spherical dilation of the automatically extracted dilation of the centerline C_U or C_M. The vertices are grouped by non-intersecting graph columns starting from this initial segmentation. These non-intersecting graph columns enable the segmentation of high curvature areas [105]. Non-intersecting graph columns are guaranteed if these are defined on the trajectory of flow lines obtained by Gaussian smoothing (with scale σ) of the coarse initial segmentation, see Fig. 4.4. Given the flow lines $\boldsymbol{f}_i : \mathbb{Z} \rightarrow \mathbb{R}^3$ where $i \in \{1, ..., Q\}$ with Q the number of voxels on the initial segmentation's surface, the graph vertex $v_{i,k} \in V$ is associated with the image position $\boldsymbol{f}_i(k)$. The graph columns are defined by the set of vertices $V_i = \{ v_{i,k} | \, k = -I_i, -I_i + 1, \ldots, O_i - 1, O_i \}$ where the uniform separation distance between vertices is given by $\delta = \| \boldsymbol{f}_i(k+1) - \boldsymbol{f}_i(k) \|$. Here $v_{i,-I_i}$ and v_{i,O_i} represent the innermost and outermost vertices of column V_i, and $v_{i,0}$ is at the initialization surface. Several edges are defined in the graph: First, the edges $v_{i,k} \overset{w_{i,k}}{\rightarrow} v_{i,k+1}$ within a graph column indicate the relation between foreground and background such that $w_{i,k}$ should be as low as possible at the position of the surfaces. Second, the smoothing penalty edges between neighboring graph columns, $v_{i,k} \overset{p}{\leftrightarrow} v_{j,k}$, penalize each vertex displacement in the graph cut by a value p. Third, the topological constraint edges within a graph column, $v_{i,k+1} \overset{\infty}{\rightarrow} v_{i,k}$, guarantee that the graph columns are cut only once. Finally, the vertex s is connected to all innermost vertices, and t to all outermost vertices.

The graph construction approach is illustrated in Fig. 4.4.

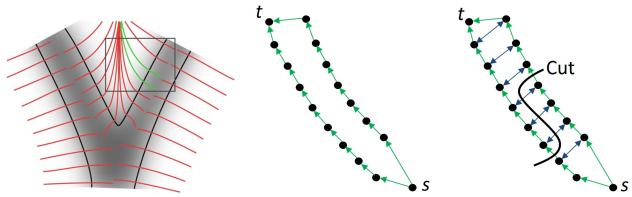

Figure 4.4: Graph construction method [98]. The non-intersecting graph columns starting from the coarse initial segmentation (gray sketch) are depicted by red curves in (a). Two graph columns are selected, depicted by green curves, to show their vertices (black dots) and intra-column edges (green arrows) in (a). The smoothing penalty edges between neighboring columns are depicted by blue arrows in (b). Additionally, an example of a graph cut is shown in (b).

To achieve a minimum value for likely $w_{i,k}$ at positions of the lumen boundary, this cost is inversely proportional to the first order derivative of the image intensity along the graph column trajectory $\boldsymbol{f}_i$. To make small adjustments to the position of the minimum (mainly caused by partial volume effects), the second order derivative is added. Thus, the edge cost $w_{i,k}$ is defined by:

$$w_{i,k} \propto \left| \alpha \frac{\partial^2 I(\boldsymbol{f}(k))}{\partial k^2} + (1 - |\alpha|) \frac{\partial I(\boldsymbol{f}_i(k))}{\partial k} \right|^{-1}, \tag{4.2}$$

where $I(\boldsymbol{f}_i(k))$ is the image intensity at the position $\boldsymbol{f}_i(k)$, and $\alpha \in [-1, 1]$ is a parameter that weights the contribution of the second derivative term.
Since the initial coarse segmentation may contain irregularities, and may be too far from the true lumen boundary, the estimated optimal surface may contain errors. To address this, the optimal surface graph method is iterated N times. The result of iteration n is used to create a new graph in iteration $n + 1$.
The segmentation method is applied to both US and MRI. The automatic segmentations S_U and S_M are used jointly with the centerlines C_U and C_M in the registration framework as explained in section 4.2.1.3.

4.3 Experiments

4.3.1 Data

We evaluated our method on data from 8 patients and 6 healthy volunteers. The patients were selected within the scope of the Plaque At Risk (PARISK) study [93]. The PARISK study is a prospective multicenter cohort study of patients with recent neurological symptoms due to ischemia in the territory of the carotid artery and < 70% ipsilateral carotid artery stenosis who are not scheduled for carotid endarterectomy

or stenting [93]. Volunteers were healthy and had no plaque. Left and right carotid were scanned in all subjects. All scannings were performed with subjects' consent.
The US images were acquired with the Philips probe L9-3 and a Philips iU22 system. The probe signal was adjusted to $4cm$ depth for 4 patients and to $3cm$ depth for 4 patients and 6 volunteers. Each US examination generates a stack of transversal 2D images. In order to obtain 3D US images, we used the Stradwin software [25] that correlates the 2D images and the position of a magnetic sensor attached to the US probe. After exporting the data to a volumetric representation, the voxels dimensions are $0.16 \times 0.16 \times 0.16\,mm^3$ for probe a depth of 3cm, and $0.21 \times 0.21 \times 0.21\,mm^3$ for a probe depth of 4cm.
The patient MRI data were acquired on a $3.0T$ GE Medical Systems Discovery MR750, using a T2-weighted double inversion recovery fast spin echo (T2w-DIR-FSE), black-blood sequence. The original voxel spacing of MRI on the patient data was $0.55 \times 0.55 \times 2.0\,mm^3$. We resampled the MRI with a cubic B-spline interpolation leading to isotropic voxels with spacing $0.55 \times 0.55 \times 0.55\,mm^3$. For the volunteer data, the voxel spacing of the MRI was $0.5 \times 0.5 \times 0.9\,mm^3$. The images were acquired using a $1.5T$ GE Medical System Signa Excite MRI machine with a proton-density-weighted fast spin echo (PDw-FSE), black-blood sequence.

4.3.2 MRI Lumen Segmentation

Lumen segmentation in MRI using the optimal-surface graph cut method was already extensively evaluated [99] on similar MRI data as used in the current study. Therefore, we used the optimized segmentation parameters from [99], which are: $\delta = 0.35\,mm$, $\sigma = 2.19\,mm$, $p = 26274$, $\alpha = 0.038$, and $N = 1$. Prior to segmentation, the N4 bias field correction method [78] was employed to correct for MRI intensity inhomogeneities within the neck area.

4.3.3 US Lumen Segmentation

Since in [98] only a preliminary evaluation of the US segmentation method was presented, we performed a cross-validation experiment to establish the optimum parameter settings on data independent of the test set. Since left and right carotids of a single subject may have similar characteristics, a leave-two-out cross-validation design was used, in which we left both vessels of a subject out of the training set. On the training set, the optimum parameter settings were determined by exhaustive grid search. As an evaluation criterion, we used the mean surface distances (MSD) (averaged over all carotids in the training set) between the resulting segmentations and the manual segmentations. The manual segmentations were performed by annotating the lumen at each five to ten 2D slices of each US image sequence. Thereafter, the lumen surface was interpolated based on these contours. The evaluated parameters of the method were: the smoothing scaling σ, the weighting parameter α, the edge capacity p determining the smoothness of the solution, and the number of iterations N. The vertex distance δ was fixed to the voxel spacing. In the optimization step, we considered the following range of parameters:

- $\sigma \in \{20, 30, 40\}$

- $\alpha \in \{-1.0, -0.5, 0.0, 0.5, 1.0\}$
- $p \in \{1000, 10000, 25000, 50000, 75000, 100000\}$
- $N \in \{1, 2, 3, 4, 5\}$

The entire 4D search space was evaluated and the selected optimum parameter configuration in each leave-two-out fold was recorded. The resulting segmentations S_U were used in further registration experiments.
In order to visualize the impact of each parameter on the segmentation results, we chose the most frequently selected parameter configuration as a base configuration and individually varied one of the parameters while computing the MSD on the entire dataset. Thus obtained MSD values are slightly overtrained, but are useful to gain insight in the effect of each parameter.

4.3.4 Evaluation of registration accuracy

In this series of experiments we evaluated the registration accuracy and compared the results with existing methods.
First, the effect of important registration parameters was investigated. We tested both rigid and nonrigid registration. For the B-spline transformation model in the nonrigid registration, we tested isotropic grid spacings $\beta \in 8, 16, 32\,mm$. For the weighting value that balances the $\mathcal{D}$ and $\mathcal{E}$ cost function terms, we tested $\omega \in 1, 2, 4, 8, 16$. The MSD between the manual US segmentation and the transformed automatic MRI segmentation was used as a measure of registration accuracy. The combination of β and ω that yielded highest accuracy was used in all further evaluations.
Second, we compared the proposed registration to three other methods. We adopt the acronym **GEO** to refer to our registration method based on geometrical features. The other methods were:

Initial Registration are obtained with the transformation T_{init}.

IP The intensity-and-point based registration [94] is used.

MAX Registrations are performed between the manual US segmentation and the automated MRI segmentation. Since exactly these segmentations are used to compute the MSD for evaluation, this "overtrained" method will indicate what is the maximum achievable accuracy of any registration method [94].

The parameters β and ω used in the methods IP and MAX were selected according to their best values defined in [94].

4.4 Results

4.4.1 US Lumen Segmentation

Tab. 4.1 displays the result of the leave-two-out evaluation for the US segmentation experiments. In this table, it can be observed that the most frequent best configuration was ($\sigma = 40, \alpha = 0.0, p = 50000, N = 5$), since the best MSD was obtained with

Subject	σ	α	p	N	Train MSD (mm)	Test MSD (mm)	
						Left Carotid	Right Carotid
P1	40	0	50000	3	0.68 ± 0.24	0.38	0.87
P2	30	0	50000	3	0.69 ± 0.24	0.69	0.49
P3	40	0	50000	3	0.69 ± 0.24	0.51	0.65
P4	40	0	50000	3	0.68 ± 0.25	0.60	0.79
P5	40	0	50000	3	0.69 ± 0.24	0.44	0.71
P6	40	0	50000	3	0.69 ± 0.24	0.55	0.61
P7	40	0	50000	3	0.69 ± 0.24	0.52	0.50
P8	20	0	50000	2	0.66 ± 0.19	0.81	1.63
V1	40	0	50000	3	0.70 ± 0.23	0.49	0.36
V2	40	0	50000	3	0.64 ± 0.19	1.34	1.05
V3	40	0	50000	3	0.69 ± 0.24	0.46	0.67
V4	40	0	50000	3	0.68 ± 0.25	0.65	0.67
V5	30	0	50000	3	0.65 ± 0.21	1.06	1.19
V6	40	0	50000	3	0.67 ± 0.25	0.72	0.78

Table 4.1: Results of leave-two-out cross-validation of the US lumen segmentation provided for each patient ($P\#$) and volunteer ($V\#$). MSD (Average±std.dev.) on the training set, and the MSD on the left and right carotid of the left-out subject are listed.

this configuration in 11 out of the 14 subjects. Fig. 4.5 summarises the segmentation results for the 28 carotids with their respective best configuration selected in the leave-two-out evaluation. The median error is around $0.6\,mm$.

In order to visualize the impact of each parameter on the segmentation results, we chose the most frequently selected parameter configuration as a base configuration and individually varied one of the parameters while computing the MSD on the entire dataset. The effect of each parameter on the segmentation accuracy can be seen in Fig. 4.6. The smoothness parameter σ had a small effect on the end results. The parameters p and α showed a clear minimum within the selected range. A value of $\alpha = 0$ means that the edge is sharp so only the first derivative suffices to localize it. The improvement caused by the number of iterations N peaked at 3 iterations (see Figure 4.7 for an illustration).

4.4.2 Evaluation of registration accuracy

Fig. 4.8 displays the overview of the combination of β and ω, containing the average results for all configurations on 28 carotids. Nonrigid registrations using $\beta = 32mm$ generally outperformed rigid registration, except for $\omega = 1$. Smaller values of β did not further improve registration accuracy: more freedom of deformation did not result in better registrations. For ω, we observe a strong improvement in registration accuracy from $\omega = 1...4$. After that, for $\omega \geq 8$, the result stabilizes. The best parameter configuration for the registration using geometrical features was $\beta = 32\,mm$ and ω=16.

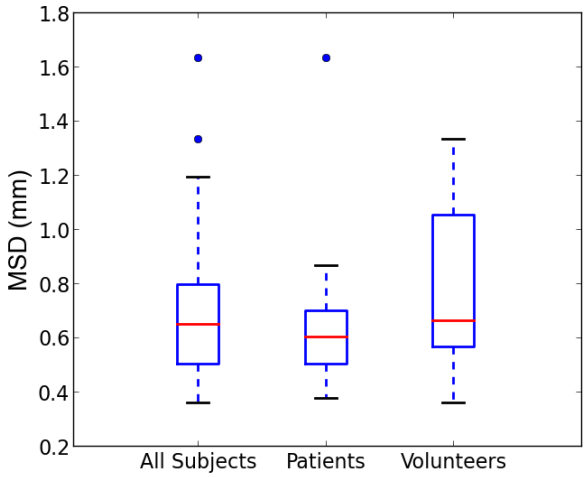

Figure 4.5: Segmentation results obtained in leave-two-out cross-validation. Results are reported for the entire test set, and separately for the patient and volunteer subsets.

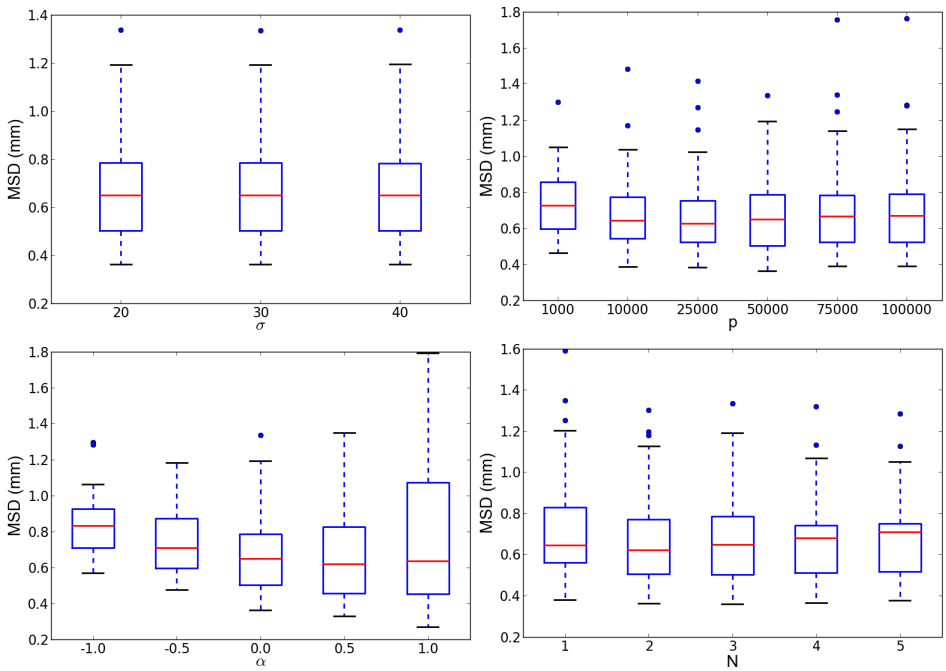

Figure 4.6: Effect of the segmentation parameters on segmentation MSD, when varying a single parameter while the other parameters are fixed at their optimum value. The tested parameters were: the smoothing scaling σ, the weighting parameter α, the edge capacity p, and the number of iterations N.

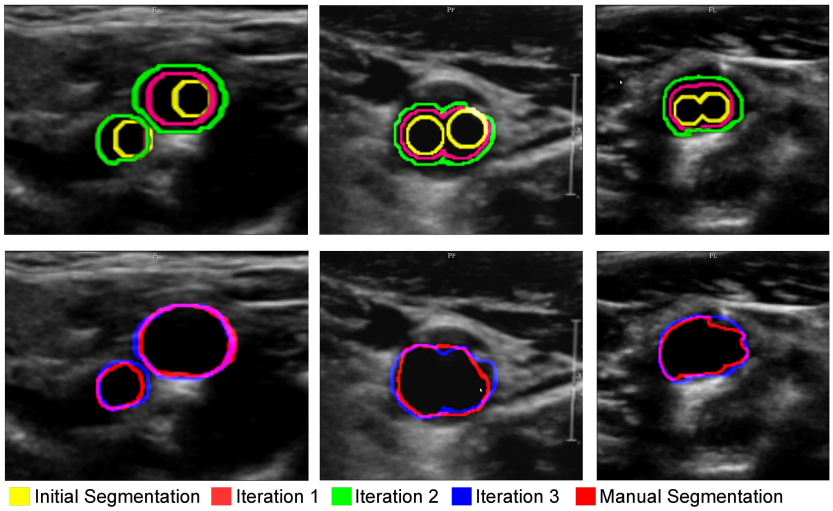

Figure 4.7: Segmentation results on US for iterations $n = 1...3$ of the optimal-surface graph cut segmentation method. Left to right: three example slices.

The results for all subjects obtained with Initial, MAX, IP and GEO are shown in Fig. 4.9. The results of MAX, IP, and GEO are shown both after the rigid and after the nonrigid registration stage. The figure shows that the proposed nonrigid GEO method considerably improves the results compared to Initial alignment. A small improvement compared to IP is observed. The nonrigid MAX method outperforms all other methods, but this was expected. The rigid MAX method (which is less prone to overfitting than nonrigid MAX) scored similar MSD as the proposed nonrigid GEO method.

Table 4.2 provides the results in table form, for the complete dataset (corresponding to Fig. 4.9) and for the volunteer and patient sets separately. For MAX, IP, and GEO, the results of nonrigid registration are shown. The table confirms that GEO outperforms IP on the entire test set, and shows that this is also the case when considering the volunteer set and patient set separately. With a Wilcoxon test on the entire test set, it was confirmed that the difference in MSD values between GEO and IP was statistically significant ($p < 0.01$).

Fig. 4.10 shows a comparison between isosurfaces of the manual segmentations in US images, and the registered MRI lumen segmentation. In Fig. 4.11 the segmentations and registrations contours are shown in planar sections of US and MRI.

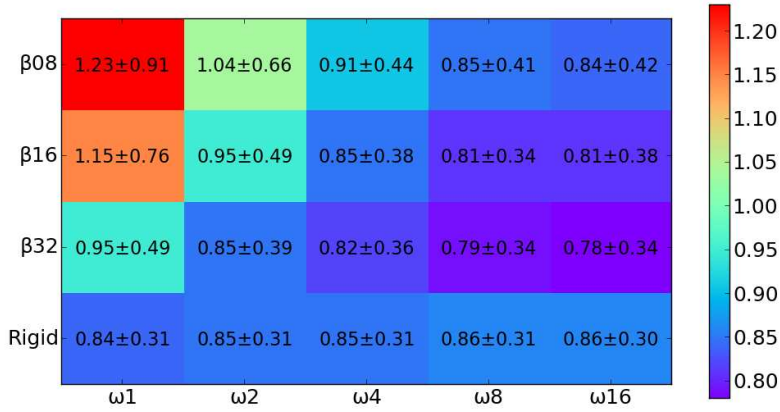

Figure 4.8: Registration results using geometrical features. Rigid and nonrigid registrations obtained with variations of the parameters β and ω. MSD values expressed in mm.

MSD avg.±std. dev. (mm)	All subjects	Volunteers	Patients
Initial	0.92±0.32	0.80±0.17	1.02±0.38
GEO	0.78±0.34	0.65±0.09	0.87±0.42
IP	0.85±0.39	0.72±0.20	0.95±0.46
MAX	0.39±0.53	0.28±0.05	0.48±0.68

Table 4.2: MSD between manual US segmentations and MRI registered segmentations for four different registration methods. The values (in mm) are reported for volunteers, patients and all subjects combined.

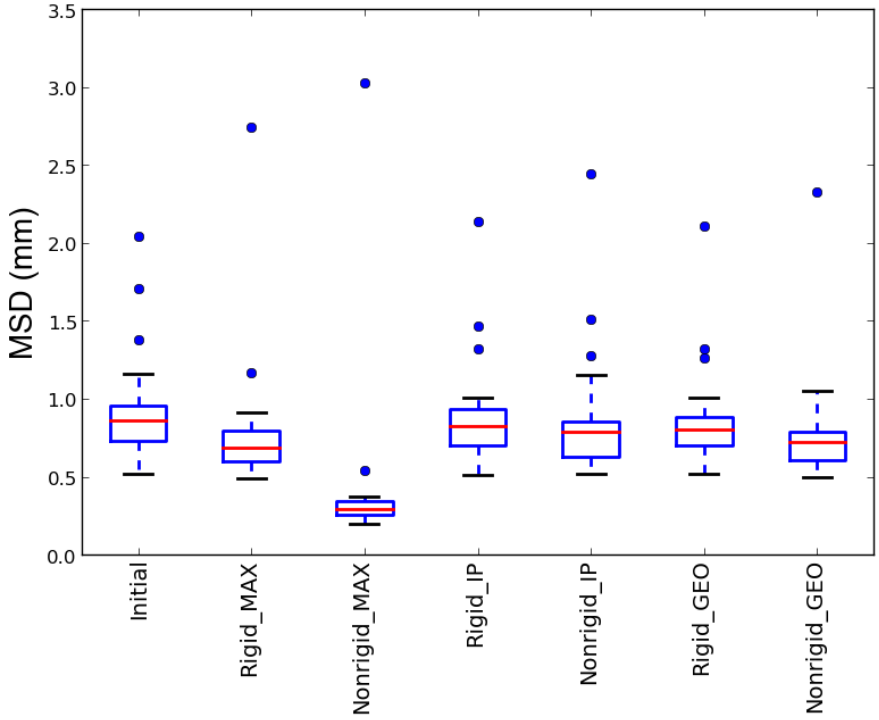

Figure 4.9: Comparison between results obtained with geometrical features based registration (GEO), intensity-and-point based registration (IP) and the maximum achievable accuracy (MAX).

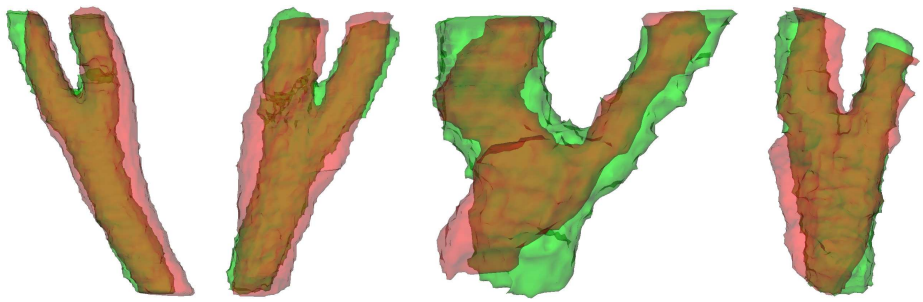

Figure 4.10: Volumetric representation of MRI segmentation registered with GEO (green) and manual US segmentation (red). Figures (a) and (b) represent carotids of volunteers and figures (c) and (d) represent carotids of patients.

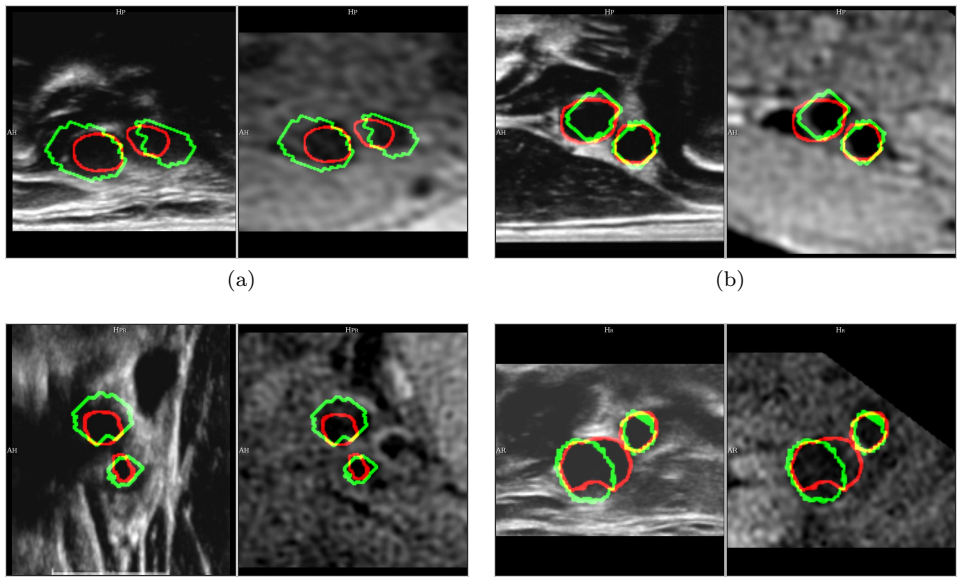

(a) (b)

(c) (d)

Figure 4.11: Side-by-side visualization US image (left) and registered MRI using the geometrical features registration (right). MRI registered segmentations and manual US segmentations are depicted by green and red contours respectively. Figures (a) and (b) represent carotid arteries of volunteers and figures (c) and (d) represent carotid arteries of patients.

4.5 Discussion

In this work, we introduced a method to register US and MRI of the carotid artery using geometrical features. Semi-automatically extracted lumen centerlines and automatic lumen segmentations are used as geometrical features. The method was evaluated in a dataset composed of volunteer and patient data and proved to be robust in the presence of noise, shadows in the US image, differences in subject's neck position between US and MRI, and presence of atherosclerotic plaque. The average MSD was significantly lower than the MSD obtained by a previously proposed method [94].
Although the automated US lumen segmentation method was extensively evaluated and proved to be a robust input to the registration framework, the MSD was in the order of four pixels. This suggests that there is still room for improvement in segmentation accuracy. In the segmentation results, it is possible to observe that the median MSD was lower for patients than volunteers. One possible cause is that the chosen parameters were more suitable for the patient set. Possibly, the development of an image-adaptive selection of parameters, in which the parameters are automatically selected from patterns observed in image intensities or centerline could improve overall performance. Furthermore, the registration results suggest that an improvement in the automatic lumen segmentation will further increase the registration accuracy, since the registration with MAX scored a lower MSD than GEO. However, it is important to notice that the same manual segmentation used for the registration in MAX was used for evaluation, leading to a bias. Manual lumen segmentation is a task open to interpretation, especially in regions where the lumen wall is not visible. Therefore, the maximum achievable registration accuracy (MAX) will probably not be achieved by any automated method.
The proposed method is largely automated but still demands minimal user interaction. For the lumen centerline detection, the user must select a point in each of three branches of the carotid artery in US and MRI data. The difficulty in implementing a fully automated method for identifying the carotid branches is related to the presence of structures with a similar shape and intensity, such as the jugular vein. In future work, it would be interesting to develop a robust algorithm able to identify the carotid branches in US and MRI without the need of manual input; this would fully automate the carotid artery registration.

4.6 Conclusion

This work introduced a method to automatically register US and MR images of the carotid artery. The registration framework is based on geometrical features, namely the artery centerlines and lumen segmentations, which are semi-automatically extracted from the US and MR images. The method requires minimal user interaction. Experiments on 28 carotids from 8 patients and 6 volunteers demonstrate robust performance. Compared to a previously proposed method [94] registration accuracy was improved significantly. The use of automated segmentations combined with centerlines leads to a high registration accuracy, thus paving the way for comprehensive multimodal analysis of atherosclerotic plaque in the carotid artery.

II

2D+t US and CEUS Registration

5

Lumen Segmentation and Motion Estimation in B-mode and Contrast-Enhanced Ultrasound Images of the Carotid Artery in Patients with Atherosclerotic Plaque

Abstract: In standard B-mode ultrasound (BMUS), segmentation of the lumen of atherosclerotic carotid arteries and studying the lumen geometry over time are difficult owing to irregular lumen shapes, noise, artifacts, and echolucent plaques. Contrast enhanced ultrasound (CEUS) improves lumen visualization, but lumen segmentation remains challenging owing to varying intensities, CEUS-specific artifacts and lack of tissue visualization. To overcome these challenges, we propose a novel method using simultaneously acquired BMUS&CEUS image sequences. Initially, the method estimates nonrigid motion (NME) from the image sequences, using intensity-based image registration. The motion-compensated image sequence is then averaged to obtain a single 'epitome' image with improved signal-to-noise ratio. The lumen is segmented from the epitome image through an intensity joint-histogram classification and a graph-based segmentation. NME was validated by comparing displacements with manual annotations in eleven carotids. The average root-mean-square-error (RMSE) was $112 \pm 73\,\mu m$. Segmentation results were validated against manual delineations in the epitome images of two different datasets, respectively containing nine (RMSE $191 \pm 43\,\mu m$) and ten (RMSE $351 \pm 176\,\mu m$) carotids. From the deformation fields, we derived arterial distensibility with values comparable to the literature. The average errors in all experiments were in the inter-observer variability range. To the best of our knowledge, this is the first study exploiting combined BMUS&CEUS images for atherosclerotic carotid lumen segmentation.

Diego D.B. Carvalho*, Zeynettin Akkus*, Stijn C.H. van den Oord, Arend F.L. Schinkel, Antonius F.W. van der Steen, Wiro J. Niessen, Johan G. Bosch, Stefan Klein, "Lumen Segmentation and Motion Estimation in B-Mode and Contrast-Enhanced Ultrasound Images of the Carotid Artery in Patients With Atherosclerotic Plaque", Published In IEEE Transaction on Medical Imaging
**both authors contributed equally to this research*

5.1 Introduction

Stroke is a major healthcare problem and one of the main causes of death and long-term disability worldwide [106]. Several studies have demonstrated that patients with carotid atherosclerotic plaques carry an increased risk of cardiovascular events, such as stroke, transient ischaemic attack, myocardial infarction and even death [106, 107]. Ultrasound has been widely used as a standard tool for inexpensive and non-invasive diagnosis of carotid atherosclerosis [108]. To assess atherosclerosis (formation of plaques in arterial walls may cause narrowing of the lumen), different ultrasound techniques have been used such as standard B-mode ultrasound (BMUS), color Doppler and Contrast-enhanced ultrasound (CEUS) [109]. For the accurate assessment of atherosclerosis, delineation of the lumen-intima contour of the carotid artery is desired.

So far, carotid lumen segmentation has mostly been done based on standard-BMUS images [110–113]. However, carotid lumen segmentation in standard-BMUS images of subjects with atherosclerotic plaques is difficult and can be inaccurate due to irregular lumen shapes, noise in the lumen, artifacts and echolucent plaques, as seen in Fig. 5.1a. Color Doppler (Fig. 5.1b) provides information on blood flow in the lumen, which enables the clinician to detect flow reduction, flow turbulence and occlusion in arteries. While there is no doubt of its usefulness, it is less suitable for vessel lumen segmentation: the border of the color-coded velocity images strongly depends on user-controlled settings of Doppler gain, velocity range and setting of the wall filter, as well as the local direction of flow. CEUS (Fig. 5.1c) is a more useful modality for visualizing the lumen. CEUS suppresses tissue information and provides the luminal shape by detecting ultrasound contrast agent: micrometer-sized gas bubbles which flow within the blood stream. CEUS provides a better delineation of carotid lumen than standard-BMUS [109,114–116]. Compared to color Doppler, CEUS shows the lumen by visualizing the presence of contrast-enhanced blood regardless of flow velocity and direction.

There have been several approaches for detection of the carotid artery contours in standard-BMUS, including deformable contours (snakes), Hough transform, dynamic programming, and classification approaches. The principles, performance, advantages and limitations for these approaches have been summarized in recent surveys [49,117, 118]. Several studies have reported that their lumen segmentation methods have limitations in presence of atherosclerotic plaque [119–121].

Carotid artery lumen segmentation in a time series allows a clinician to characterize the lumen diameter over the cardiac cycle, and hence to assess the arterial wall stiffness. Several studies hypothesized that arterial stiffness parameters indicate early vascular changes that predict the development of major vascular disease. Indices of arterial stiffness that have been proposed include strain [122–124], stress [123, 124], elastic modulus or Young's modulus [122–124], and distensibility coefficient [123–125]. Van Popele measured carotid wall motion by means of a vessel wall movement detector system [126]. The displacement of the arterial wall was obtained by tracking the wall position in a selected M-mode line by using the raw ultrasound (RF) signal. The algorithm is limited as it utilizes only one M-mode line for measuring vessel wall motion and it requires manual user interactions. An automated method for distensibility

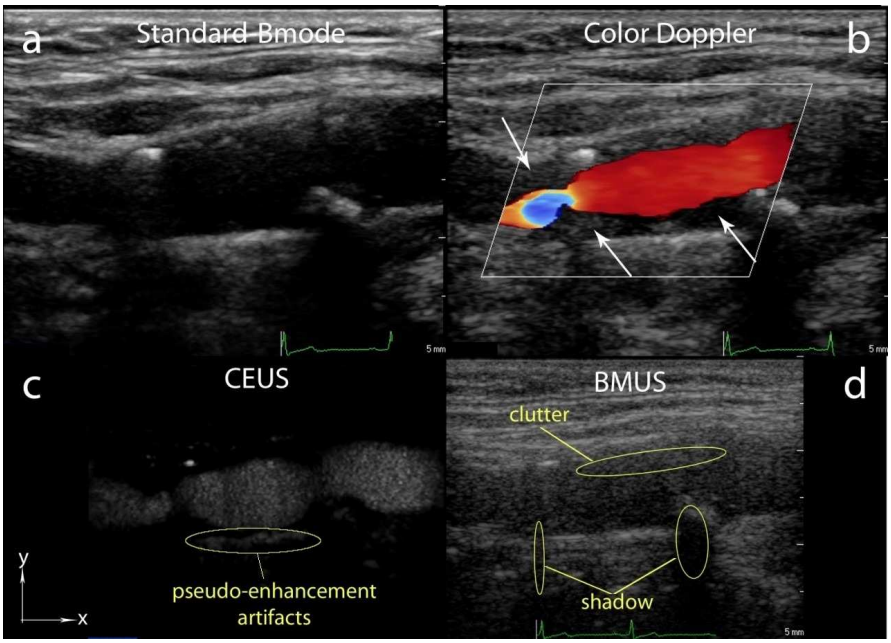

Figure 5.1: An example of a carotid artery image acquired with different ultrasound techniques. Standard BMUS (a), Color Doppler (arrows show echolucent plaques, blue color shows direction change in the flow) (b), Side-by-side CEUS and B-mode images (c-d). CEUS artifacts are indicated (c). Shadow and clutter in BMUS are indicated (d).

measurement in BMUS was presented by Teynor et al. [127]. Their method requires interactive manual corrections for difficult cases with shadow (echo dropouts) or a high level of noise in the BMUS images.

In this study, we present a novel carotid lumen segmentation and motion estimation approach that is suitable for atherosclerotic arteries, less prone to artifacts and more automated than approaches that have appeared in the literature. The method is fully automatic, provided that the image contains just a single branch of the carotid artery. Our method quantifies carotid lumen geometry in subjects with atherosclerotic plaque from simultaneously acquired BMUS and CEUS images. Integrated analysis of BMUS and CEUS provides essential information on the lumen contour in patients with atherosclerotic plaques (see Fig. 5.1). This analysis, however, presents two additional challenges: CEUS-specific imaging artifacts and lower signal-to-noise ratio (SNR) in BMUS: as low signal power is used to avoid the disruption of ultrasound contrast agents in CEUS, these BMUS images have lower SNR compared to a standard-BMUS image. In order to improve the SNR and suppress noise, we compensate motion in the BMUS and CEUS image sequence and average image intensities pixelwise over the complete sequence. This leads to a single integrated BMUS and CEUS image that we refer to as the 'epitome' image, since it is the best possible presentation of the patient's anatomy. Motion compensation is a prerequisite step for obtaining epitome images, as carotid images contain considerable motion, such as probe movement, patient movement, breathing and pulsation. Previous studies on motion estimation in carotid ultrasound mostly focused on rigid registration of multiple local regions based on block matching [128–131]. We propose to use an accurate nonrigid motion estimation (NME) technique.

The constructed epitome image is used in the automated lumen segmentation method. A particular challenge here is the presence of saturation and pseudo-enhancement artifacts [132] in the CEUS image. These artifacts should be suppressed as they could mislead the lumen segmentation. We exploit the joint information of the epitome image to classify artifacts, lumen, and tissue. Following this classification, we use a robust and efficient graph-based technique for carotid lumen segmentation. Finally, we transform the lumen contours extracted from the epitome image back to each time frame by using the deformation pattern estimated with NME in order to obtain the assessment of carotid artery distensibility, or other arterial stiffness measures.

Summarizing the main contribution of our study is twofold. First, we provide nonrigid motion compensation for BMUS and CEUS image sequences. Second, using the combined BMUS and CEUS motion-compensated data, we automatically segment the carotid artery lumen, even in the presence of typical artifacts present in both BMUS and CEUS. To the best of our knowledge this is the first study using combined BMUS and CEUS to improve the segmentation of the lumen of the carotid artery in patients with atherosclerotic plaques.

5.2 Methods

This section is divided in three subsections, describing NME, lumen segmentation and distensibility calculation, respectively. The method steps and their relation are

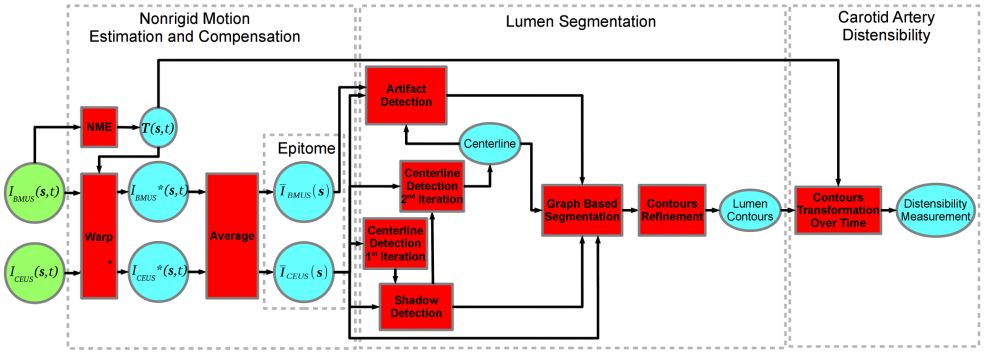

Figure 5.2: Flowchart of the steps of the method. Inputs (green), operations (red) and outputs (blue). $\boldsymbol{T}(\boldsymbol{s},t)$: Transformation obtained from BMUS with NME. $I^*_{BMUS}(\boldsymbol{s},t)$, $I^*_{CEUS}(\boldsymbol{s},t)$: Motion compensated BMUS and CEUS respectively. $\bar{I}_{BMUS}(\boldsymbol{s})$, $\bar{I}_{CEUS}(\boldsymbol{s})$: Epitome images.

shown in the flowchart in Fig. 5.2.

5.2.1 Nonrigid Motion Estimation

Owing to the acquisition procedure, the CEUS and BMUS images cover the same field of view and are intrinsically spatially aligned. Figs. 5.1c and 5.1d show an example of a typical pair of CEUS and BMUS images. The simultaneous BMUS & CEUS imaging leads to two 2D+time (2D+t) image series, $I_{BMUS}(\boldsymbol{s},t)$ and $I_{CEUS}(\boldsymbol{s},t)$, where $\boldsymbol{s}$ is a spatial coordinate (x,y) and t is the time frame index with τ = number of time frames. For the nonrigid motion estimation (NME), we adopted the groupwise registration method of Metz et al [133] and optimized it for our purpose as will be described in Section 5.4.1. The method estimates the nonrigid deformation of the carotid artery over time from the BMUS image sequence, and subsequently compensates this nonrigid motion in both the BMUS and CEUS image sequences. The method is based on the minimization of the pixel intensity variance over time [133]. The CEUS image sequence violates the constant intensity assumption of the NME method: it exhibits high intensity variations among frames due to slow flow-related contrast concentration changes. Therefore, we use the BMUS image for motion estimation, since it presents only minor intensity variations over time. We denote the motion-compensated image sequences as:

$$I^*_{BMUS}(\boldsymbol{s},t) = I_{BMUS}(\boldsymbol{T}(\boldsymbol{s},t),t)$$

$$I^*_{CEUS}(\boldsymbol{s},t) = I_{CEUS}(\boldsymbol{T}(\boldsymbol{s},t),t)$$

where $\boldsymbol{T}(\boldsymbol{s},t)$ is the transformation field obtained in NME. After motion compensation, the resulting sequences can be averaged over time:

$$\bar{I}_{BMUS}(\boldsymbol{s}) = \frac{1}{\tau}\sum_{t=1}^{\tau} I^{*}_{BMUS}(\boldsymbol{s},t)$$

$$\bar{I}_{CEUS}(\boldsymbol{s}) = \frac{1}{\tau}\sum_{t=1}^{\tau} I^{*}_{CEUS}(\boldsymbol{s},t)$$

The average images $\bar{I}_{BMUS}(\boldsymbol{s})$ and $\bar{I}_{CEUS}(\boldsymbol{s})$ have improved-SNR and serve as epitome images. In this way, noise is attenuated and the lumen and plaque structures are more clearly depicted, as can be seen in Fig. 5.3. All further processing of the lumen segmentation is performed on these epitome images. The relations between the transformations and the images are shown in Fig. 5.2.
The groupwise registration method produces a nonrigid motion estimate on the whole image domain, differently from existing techniques for motion estimation in ultrasound [128–130]. The deformations are modeled by a nonrigid 2D+t B-spline transformation, ensuring smoothness (continuous differentiability) both in the spatial and temporal dimensions. An adaptive stochastic gradient descent optimizer [134] is employed to calculate the transformation parameters that minimize a dissimilarity measure based on the variance of the intensities at corresponding spatial locations. In order to improve registration robustness, a multi-resolution strategy is applied: for each resolution, the image is smoothed with a Gaussian filter with spread σ. Important parameters of the method are: 1) the spacing β of the B-spline control points, both spatially (in mm) and temporally (in time frames), 2) the number of resolutions ρ, and 3) the degree of image smoothing σ. In the experiments, a range of settings for these parameters will be evaluated.

5.2.2 Lumen Segmentation

We perform lumen segmentation of the carotid artery on the epitome images $\bar{I}_{BMUS}(\boldsymbol{s})$ and $\bar{I}_{CEUS}(\boldsymbol{s})$. Our segmentation method consists of five steps: centerline estimation, detection of shadowing, detection of artifacts, graph based segmentation and refinement of lumen contours (see Fig. 5.2).

5.2.2.1 Centerline Estimation

We detect the centerline of the carotid artery which appears approximately horizontal (along the x-direction) in the image. As a preprocessing, we apply a 2D Gaussian smoothing filter G to $\bar{I}_{CEUS}(\boldsymbol{s})$ using a vertical spread σ_y that is relatively large with respect to the expected vessel size. This filter has the highest response around the centerline of the lumen. The smoothing in horizontal direction, controlled by σ_x, suppresses the influence of small artifacts (saturation and pseudo-enhancement artifacts)

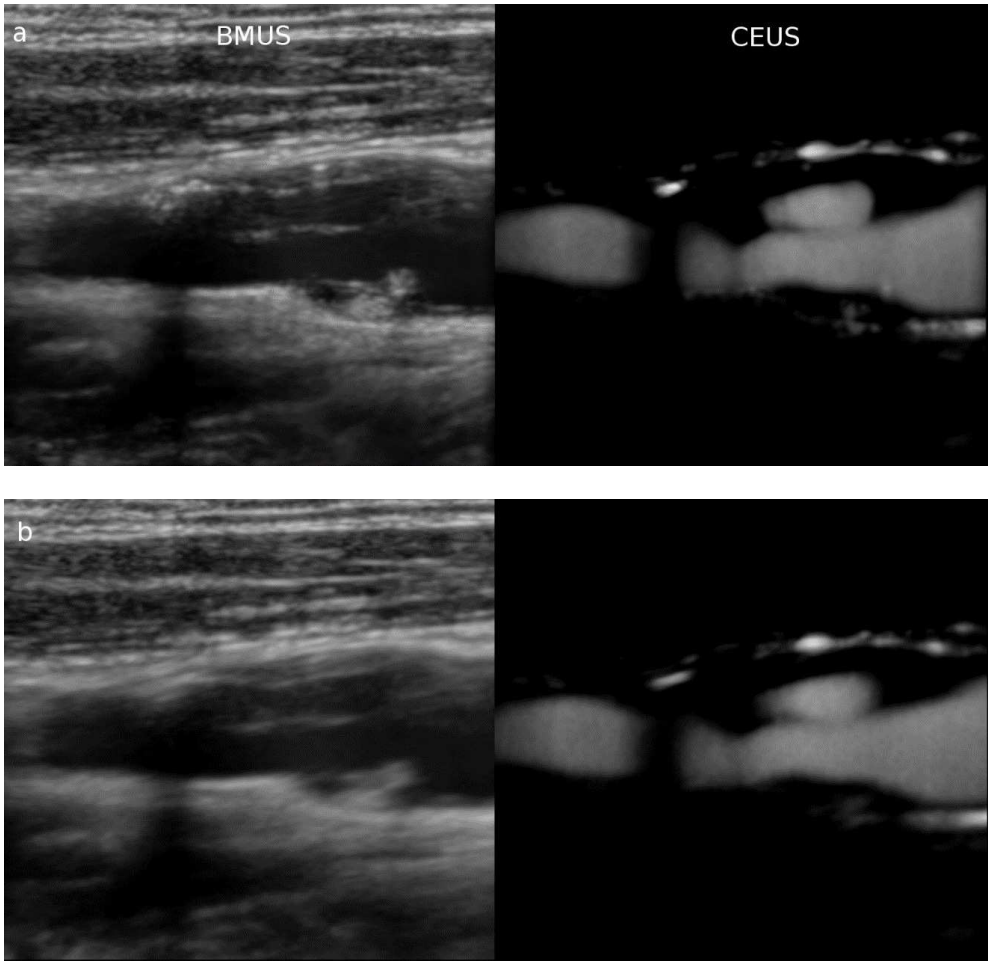

Figure 5.3: Average BMUS and CEUS images (150 frame sequence) with (a) and without (b) motion compensation. Average images without motion compensation have a blurry appearance, while the 'epitome' images after motion compensation are sharper.

near the lumen in the CEUS image. After preprocessing, we detect the centerline of the carotid artery in the CEUS image by finding a minimum cost path, using dynamic programming in the x-direction [131, 135, 136]. We defined the maximum step size in the cost path as one pixel. The dynamic programming procedure uses negated gray scale values of the blurred CEUS epitome as a cost image $c(\boldsymbol{s})$:

$$c(\boldsymbol{s}) = -G * \bar{I}_{CEUS}(\boldsymbol{s}) + k, \text{ where } k = \max_{\mathbf{s}}(G * \bar{I}_{CEUS}(\boldsymbol{s}))$$

The added constant k ensures that $c(\boldsymbol{s}) > 0$ everywhere.

5.2.2.2 Detection of Shadowing

After centerline detection, we check for presence of shadowing, which is caused by strong reflection or attenuation, especially from calcifications. Centerline detection and subsequent lumen segmentation will be affected by shadowed regions due to the low signal in those regions. Therefore, shadowed regions should be identified to avoid their influence in obtaining optimal centerline and lumen contours. To detect the shadowed region we compute the mean intensity in a vertical kernel of height κ_1 around each detected point on the centerline in the CEUS epitome image and fit a linear curve to these intensities. The size of this kernel must be smaller than the expected typical size of the lumen. The points that show an intensity drop of at least 50% in the intensity profile compared to the linear fit are considered to indicate shadow regions. When a shadow region is detected at a certain x-coordinate, all points in the cost image $c(\mathbf{s})$ with that x-coordinate are assigned the same cost value to ensure that this region does no longer affect the centerline extraction. Based on this modified cost image, the centerline is re-estimated.

5.2.2.3 Detection of Artifacts

In order to obtain an accurate lumen segmentation, the pseudo-enhancement artifacts (see Fig. 5.1c) and saturation artifacts in the CEUS image need to be detected, as they may mislead the segmentation procedure. The pseudo-enhancement artifacts in the lower part of the CEUS images are caused by nonlinear distortion of the ultrasound signal when it crosses regions with high concentration of contrast, such as the carotid lumen. As these distorted ultrasound signals will be backscattered from the tissue below the lumen, the tissue cancellation will not be perfect in the far wall, and false contrast will appear in the plaque or tissue region right below the lumen. These artifacts appear bright both in the CEUS and BMUS image, while true contrast corresponds to dark BMUS regions.
The upper part of the lumen in the CEUS image is not affected by the pseudo-enhancement artifacts but it may be contaminated with artifacts due to saturation; signals near the maximum intensity level are clipped. These artefacts are easier to detect as they have distinctive, very high contrast intensity levels (and are also bright in BMUS). To detect these different artifacts in CEUS, we construct a joint histogram of the intensities in $\bar{I}_{BMUS}(\boldsymbol{s})$ and $\bar{I}_{CEUS}(\boldsymbol{s})$ and define a joint-intensity classifier. We

model the joint histogram by a mixture of 2D Gaussians, corresponding to four classes $\psi \in \{B, T, L, A\}$: where B = Background, T = Tissue, L = Lumen, A = Artifacts. As seen in Figs. 5.3 and 5.4a (schematically depicted joint histogram), lumen is bright in CEUS but dark in BMUS. Tissue is bright in BMUS but dark in CEUS. Background (echolucent tissue) is dark in both BMUS and CEUS. Artifacts are bright in CEUS and their corresponding regions in BMUS are bright as well. Each class ψ is modeled by a 2D Gaussian in the joint histogram, with parameters $\theta_\psi = \{\mu^c_\psi, \sigma^c_\psi, \mu^b_\psi, \sigma^b_\psi\}$ where μ^c_ψ and σ^c_ψ are intensity mean and standard deviation in CEUS, and μ^b_ψ and σ^b_ψ are intensity mean and standard deviation in BMUS. Let Θ denote the collection of all parameters θ_ψ. The initialization of parameters θ_B, θ_T and θ_A is based on the typical appearance of intensities in $\bar{I}_{BMUS}(\boldsymbol{s})$ and $\bar{I}_{CEUS}(\boldsymbol{s})$ as discussed above. For the L class, we select the mean and standard deviation of the intensities in a narrow band (size κ_2) around the centerline to initialize θ_L. The Gaussian mixture weights are initialized to a constant value (1/4). These initial parameters are fed into an expectation-maximization algorithm [137,138] to estimate Θ and find the probability $p(\bar{I}(\boldsymbol{s}) \mid \psi(\boldsymbol{s}), \Theta)$ of each observed pair of intensities $\bar{I}(\boldsymbol{s}) = [\bar{I}_{BMUS}(\boldsymbol{s}), \bar{I}_{CEUS}(\boldsymbol{s})]$ given the pixel belongs to the background, tissue, lumen or artifact class. Since the parts of the lumen below and above the centerline contain different type of artifacts, classification is performed separately in the upper and lower arterial wall using two different initializations for the artifact class. Saturation artifacts have high mean intensity and low standard deviation, whereas pseudo-enhancement artifacts have intensity similar to contrast intensity in the lumen and high standard deviation. The probability map for the image is shown in Fig. 5.4b with combined results of two initializations of artifact class for upper and lower parts of the vessel.

5.2.2.4 Graph-based Segmentation

We detect the upper and lower lumen contours with a graph-based minimum cost path approach using dynamic programming. The cost image is based on the epitome $\bar{I}_{CEUS}(\boldsymbol{s})$ and the results from the centerline estimator, the shadow detector, and the artefact segmentation. The method is fully automatic and does not require manual annotation of start- or end-point. The start- and end-points of the lumen contours are defined by the dynamic programming procedure, since the lumen contour is the minimum-cost path connecting the left and right sides of the image.

First, we obtain the y-directional gradient of $\bar{I}_{CEUS}(\boldsymbol{s})$ by applying a Gaussian derivative filter (standard deviation $0.3\,mm$): $\nabla_y \bar{I}_{CEUS}(\boldsymbol{s}) = \nabla_y G * \bar{I}_{CEUS}(\boldsymbol{s})$. The basic cost image $\widetilde{\nabla_y} I_{CEUS}(\boldsymbol{s})$ is defined as the negative gradient image, $\widetilde{\nabla_y} I_{CEUS}(\boldsymbol{s}) = -\nabla_y \bar{I}_{CEUS}(\boldsymbol{s})$, for the upper contour and $\widetilde{\nabla_y} I_{CEUS}(\boldsymbol{s}) = \nabla_y \bar{I}_{CEUS}(\boldsymbol{s})$ for the lower contour. Second, all points in image columns corresponding to shadow regions are assigned the same (arbitrary) cost value to neutralize those regions. Third, saturation and pseudo-enhancement artifacts in the CEUS are suppressed by multiplying $\widetilde{\nabla_y} I_{CEUS}(\boldsymbol{s})$ with the inverse of the posterior probability of the artifact class, $\tilde{p}_A(s)$:

$$\tilde{p}_A(\boldsymbol{s}) = 1 - p(\bar{I}(\boldsymbol{s}) \mid \psi(\boldsymbol{s}) = A, \Theta)$$

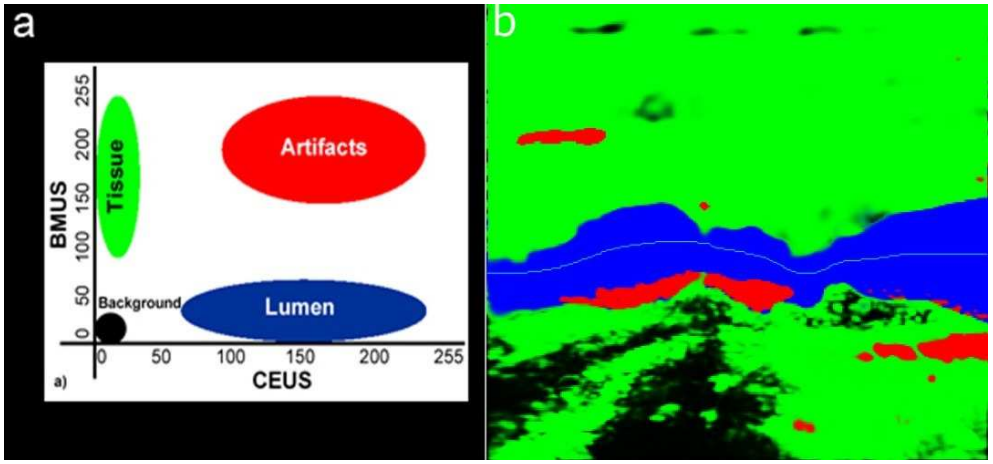

Figure 5.4: a) Schematic depiction of joint histogram of BMUS and CEUS, b) Probability map obtained through the expectation-maximization algorithm. RGB image channels represent: $p(\bar{I}(\mathbf{s}) \mid \psi(\boldsymbol{s}) = B, \Theta) =$ black, $p(\bar{I}(\boldsymbol{s}) \mid \psi(\boldsymbol{s}) = T, \Theta) =$ green, $p(\bar{I}(\boldsymbol{s}) \mid \psi(\boldsymbol{s}) = L, \Theta) =$ blue, $p(\bar{I}(\boldsymbol{s}) \mid \psi(\boldsymbol{s}) = A, \Theta) =$ red.

Fourth, we apply a curve smoothness penalty, linearly proportional to the step in y-direction between adjacent x-positions. Fifth, we multiply the cost with a factor that is linearly proportional to the distance from the centerline to prevent jumps to far layers. The minimum cost path calculation is performed in 'modified' pixel grid coordinates (u, v), where u is the original x-index and v is the y-index relative to the centerline. The cumulative cost C as a function of (u, v) in the dynamic programming framework for detecting the upper and lower lumen contours thus becomes as follows:

$$C(u,v) = \min_{r\in\{-1,0,1\}} [C(u-1, v+r) + \widetilde{\nabla_y} I_{CEUS}(u,v) \cdot \tilde{p}_A(u,v) \cdot \left(1 + \frac{|r|}{\gamma_1}\right) \cdot \left(1 + \frac{|v|}{\gamma_2}\right)] \tag{5.1}$$

The maximum step size of 1 pixel ($max\,|r| = 1$) limits the search space. We introduced two weighting factors γ_1 and γ_2 to control the amount of penalization for the step size $|r|$ and the distance from the centerline $|v|$, respectively.

5.2.2.5 Refinement of Lumen Contours

In the final step of the segmentation algorithm, we resample the image with subpixel precision in a narrow band along the upper and lower contours to follow curves more precisely and obtain smoother contours. In the refinement process, we first follow the local orientation of the contours by fitting a least squares regression line to a κ_3 neighborhood of each point on the contours and find the vectors orthogonal to the fitted regression line for each contour point. Next, we resample a band of size κ_4 along the orthogonal vectors around each contour point with subpixel-precision (one fourth of pixel size, ~25μm), using cubic spline interpolation. In the resampling process, we chose the length of orthogonal vectors as $1\,mm$ inward to the lumen for both of the contours. For the outward direction, for the upper contour we chose $0.5\,mm$ and for the lower contour $0.1\,mm$. The reason for using a shorter κ_4 in the lower contour outward to lumen is to avoid the influence of imperfectly suppressed pseudo-enhancement artifacts. Based on the resampled image, the lumen contour is re-estimated using Eq. (1), omitting in this case the penalty term for the distance to the centerline. Lastly, the refined contours are transformed back to the original coordinate space. An example of the segmentation is shown in Fig. 5.5.

5.2.3 Carotid Artery Distensibility

In order to study the carotid geometry over time, the upper and lower lumen contour points from the epitome images are transformed to each time frame using $\boldsymbol{T}(\boldsymbol{s}, t)$ obtained previously with NME. This is done to compute the distensibility coefficient (DC) of the whole section of the carotid artery wall for each cardiac cycle. To measure the radial distensibility, the motion in a direction orthogonal to the lumen centerline should be estimated (longitudinal distension as for example studied in [139] is not considered in this work). For the measurements, a segment of $1\,cm$ length of artery free from plaque along the x-dimension is manually selected (see Fig. 5.6). Plaque regions should be avoided because there exists no proper definition of distensibility in plaque regions. We propose two methods to calculate the distensibility in this region. In the first method (DC-Line), the distensibility is calculated for a single line orthogonal to the lumen, located in the center of the $1\,cm$ segment. This method resembles the ground truth manual annotation approach described in Section 4.3. In the second method (DC-ROI), all lines inside the $1\,cm$ region of interest are selected, to potentially obtain a more robust measurement by averaging the DC over these lines. The local orientation of the centerline is estimated by fitting a least square regression line to a κ_3 neighborhood of each point on the artery centerline. Subsequently, intersection points of each orthogonal vector with the upper and lower lumen contour over time are detected. The R-peaks of ECG signal are automatically extracted from the ECG annotation in the BMUS images. Pulse pressure difference ΔP is calculated by subtracting diastolic pulse pressure from systolic pulse pressure. The systolic diameter SD, diastolic diameter DD, and distensibility coefficient $DC = 2(SD - DD)/(DD\Delta P)$ [125] are calculated for each cardiac cycle (and averaged over all lines within the $1\,cm$ segment in case of the DC-ROI approach). The resulting DC values are averaged over multiple cardiac cycles to obtain a single robust value

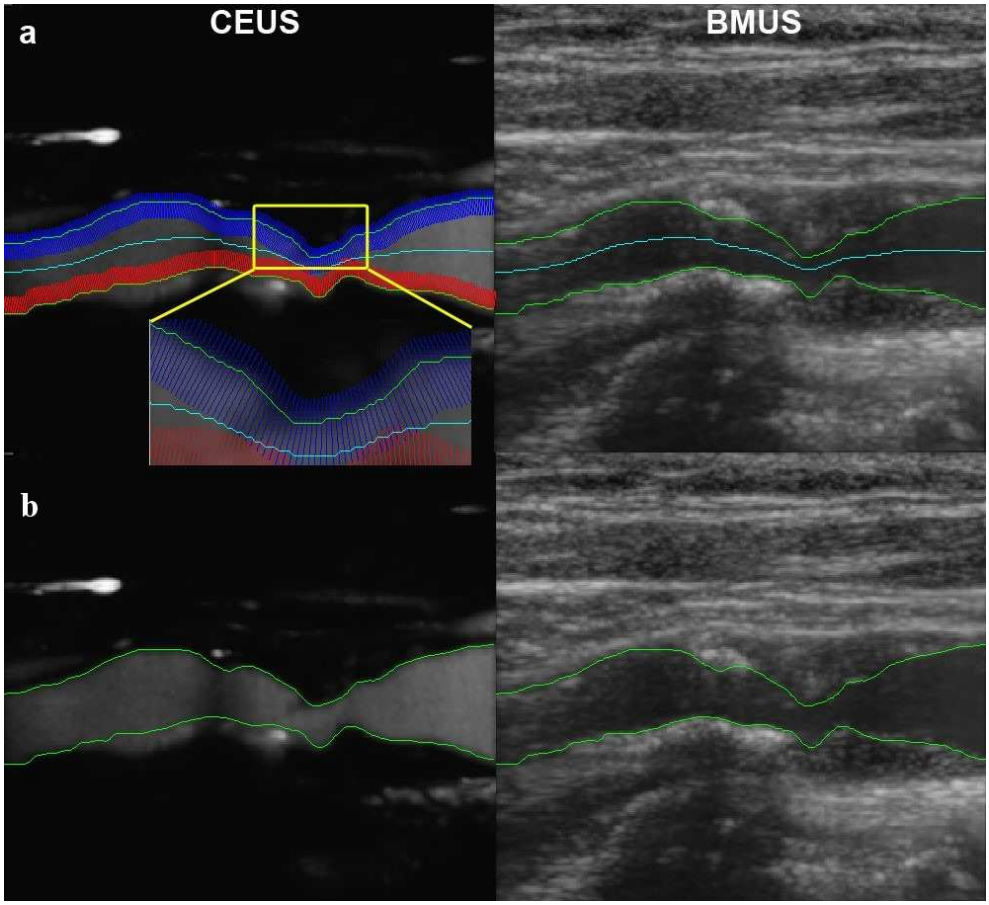

Figure 5.5: Example carotid artery lumen segmentation. a) Visualization of the resampling process, showing the orthogonal vectors to the contours as red and blue lines for the lower and upper contour respectively. b) Resulting contours estimated with subpixel-precision (one fourth of pixel size, ~ 25μm). Note the pseudo-enhancement artefacts in the far wall, which are correctly kept out of the lumen by the segmentation.

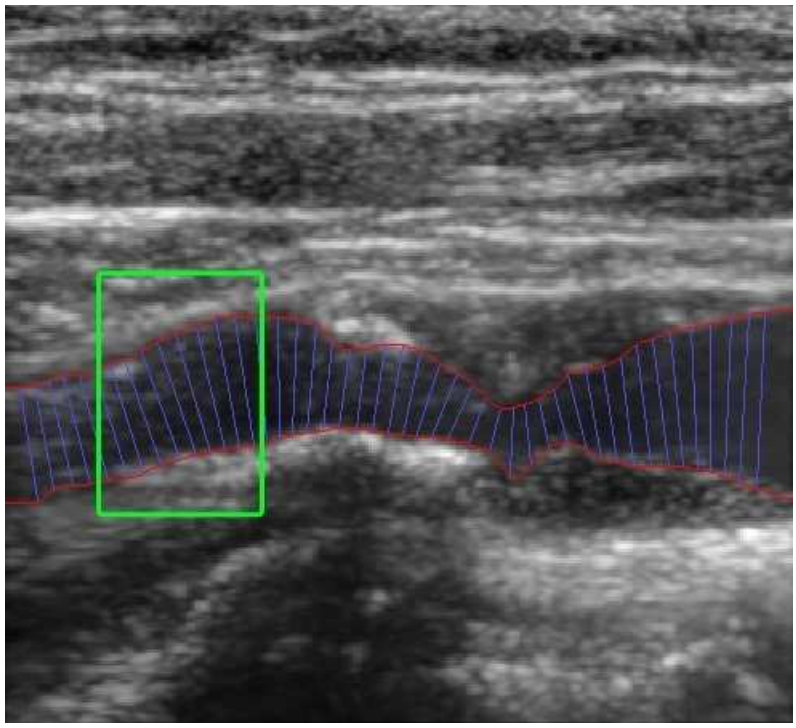

Figure 5.6: Region of interest (1 cm width) for distensibility assessment highlighted in green. The perpendicular lines to the centerline are drawn in blue.

for the distensibility coefficient of the artery.

5.3 Data

5.3.1 Data Acquisition

Simultaneous, side-by-side CEUS and BMUS images were acquired at ~20Hz frame rate using a Philips iU22 system (Philips Medical Systems, Bothell, USA) with an L9-3 linear probe. Simultaneously acquired CEUS and BMUS are saved and retrieved as a DICOM file for offline post processing. Systolic and diastolic blood pressures were measured for each patient before the ultrasound examination. The BMUS&CEUS examination of the carotid arteries were performed using a standardized image acquisition protocol. The protocol was based on the American Society of Echocardiography consensus statement [140]. Pulse pressure of each patient was recorded before examinations. CEUS was performed using intravenous administration of 0.5mL bolus of SonoVue ultrasound contrast agent (Bracco S.p.A., Milan, Italy). For the CEUS examination, power modulation imaging and a mechanical index of 0.06-0.08 were

used. For each 0.5mL bolus of SonoVue injection, a 20 seconds image sequence was recorded.

5.3.2 Patient Population and Study Protocol

All subjects were scanned in the Erasmus MC, University Medical Center Rotterdam in the scope of the PARISk project. The study protocol was approved by the ethical committee at Erasmus MC, and all study participants provided informed consent. The subjects were selected randomly, as a subset from the database of the PARISk project, and were grouped in datasets I and II. The datasets contain subjects with different classifications of degree of stenosis [141]. Dataset I consists of 11 carotid arteries with mild to moderate stenosis from 9 patients. The images of this dataset have an average pixel spacing of $95 \pm 24 \mu m$. This dataset was used in a previous study [131] and this allowed us to compare our NME results to the LRST motion estimation technique presented in that work. A subset of 9 carotid arteries in dataset I was used in a second experiment of NME, and for the evaluation of segmentation and distensibility. We refer to this subset as dataset I'. Two carotid arteries were excluded from dataset I because they were zoomed images and the far walls of the arteries were missing in the field of view. Dataset II consists of 10 carotid arteries with moderate to severe stenosis from 8 patients and the pixel spacing of the images in this dataset is $102 \pm 11 \mu m$. Dataset II was used to investigate the generalizability of the segmentation. This dataset was not used in any way during development and optimization of the method.

5.4 Experiments and Validation

5.4.1 Motion Estimation

5.4.1.1 Tracking of a Point in the Plaque

First, we evaluated the NME method on the 11 carotid artery images in dataset I, for points in the plaque region. Validation of the motion estimation accuracy was performed by comparing automated to manual tracking. In each image sequence, $\tau = 150$ time frames per carotid were tracked by $J = 3$ observers (GK, SO, ZA). A point on the plaque $\boldsymbol{p}^j(t)$ was selected by an observer j who manually tracked the motion in each time frame. The displacements tracked by each observer on each frame are denoted by: $\boldsymbol{d}^t(t) = \boldsymbol{p}^t(t) - \boldsymbol{p}^j(0)$. We established as the ground truth $\boldsymbol{d}^*(t)$ the average of the displacements for all observers on each time frame: $\boldsymbol{d}^*(t) = \frac{1}{J} \sum_{j=1}^{J} \boldsymbol{d}^j(t)$. In order to automatically obtain the displacement of $\boldsymbol{p}^j(0)$ across the subsequent time frames, we apply a composition of the forward and inverse transformation (as explained in [133]): $\tilde{\boldsymbol{T}}(\mathbf{s}, t) = \boldsymbol{T}(\boldsymbol{T}^{-1}(\boldsymbol{s}, 0), t)$. We denote the resulting displacements obtained with this transformation as $\boldsymbol{q}^j(t)$, i.e.: $\boldsymbol{q}^j(t) = \tilde{\boldsymbol{T}}(\boldsymbol{p}^j(0), t) - \boldsymbol{p}^j(0)$. This is done to directly compare the displacement pattern between trackings, irrespective of the absolute start position $\boldsymbol{p}^j(0)$, which was slightly different across observers. All automated trackings $\boldsymbol{q}^j(t)$ were compared against the ground truth ($\boldsymbol{d}^*(t)$), and

we computed the longitudinal error $e_x^j(t)$, radial error $e_y^j(t)$, and Euclidean error $e_{Euclid}^j(t)$ for each time frame:

$$e_x^j(t) = q_x^t(t) - d_x^*(t)$$

$$e_y^j(t) = q_y^t(t) - d_y^*(t)$$

$$e_{Euclid}^j(t) = \sqrt{e_x^j(t)^2 + e_y^j(t)^2}$$

We calculated the root mean square error (RMSE) over time for each carotid artery and for each observer j. The errors were averaged over j to obtain a single measure per image sequence:

$$\varepsilon_x = \frac{1}{J} \sum_{j=1}^{J} \sqrt{\frac{1}{\tau} \sum_{t=1}^{\tau} e_x^j(t)^2}$$

$$\varepsilon_y = \frac{1}{J} \sum_{j=1}^{J} \sqrt{\frac{1}{\tau} \sum_{t=1}^{\tau} e_y^j(t)^2}$$

$$\varepsilon_{Euclid} = \frac{1}{J} \sum_{j=1}^{J} \sqrt{\frac{1}{\tau} \sum_{t=1}^{\tau} e_{Euclid}^j(t)^2}$$

To quantify the interobserver variability, we also computed RMSE for each observer with respect to the ground truth.
The NME method was evaluated with different settings for the B-spline control point spacing β, the number of resolutions ρ (employed in the multi-resolution strategy used by NME), and the degree of image smoothing σ. For β we investigated a range of $1.25\,mm$ to $20\,mm$ for the spatial dimension of the grid spacing, and a range of 3 to 12 frames for the temporal dimension. For the number of resolutions, we tested $\rho = 3$ and $\rho = 5$. For the degree of smoothing, we evaluated $\sigma = 0.5$, $\sigma = 1$, and $\sigma = 2$ voxels. In total, 42 different configurations were tested and the optimal configuration was selected. The best configuration was compared with results obtained by each observer and with the LRST method proposed in [131], which is a conventional speckle tracking technique for obtaining a local motion estimate in ultrasound images. A statistical analysis among groups was performed with repeated ANOVA test. For all the statistical tests in this work, we considered the significance level as $p < 0.05$.

5.4.1.2 Tracking of Points in the Arterial Wall

In this experiment, we evaluated NME on different locations on the wall of the carotid artery. For this purpose, we divided the carotid artery into three segments. A point on the wall in each segment was selected and tracked by two observers (DC, ZA) in 100 frames for the 9 carotid arteries in dataset I'. In these experiments we used the optimal parameters defined in the previous experiment and the same evaluation methodology. We performed independent t-tests to evaluate the statistical significance between the NME and the difference between observers for ε_x, ε_y and ε_{Euclid}.

5.4.2 Lumen Segmentation

Validation of automatic lumen contour extraction was achieved by comparing to manual lumen segmentations of two independent observers (DC, ZA) in the nine carotid arteries of dataset I' and the ten carotid arteries of dataset II. The evaluation was performed in the epitome images for both datasets, and in five randomly selected time frames $t \in \{11, 18, 37, 74, 135\}$ in the images of dataset I'. The average of the manual segmentations of the two observers was considered as the ground truth. The differences between automated and manual segmentation were expressed as RMSE. The RMSE between two observers was considered as interobserver variability. An alternative definition for interobserver variability would have been to compute the average RMSE between observer and the ground truth, but since the ground truth is based on exactly these two observers, this would give a too optimistic estimate of interobserver variability.

For the artifact detection step, we initialized the parameters of the classes of the Gaussian mixture model based on typical appearance of intensities in BMUS and CEUS images of dataset I' as follows: $\theta_B = \{\mu_B^c, \sigma_B^c, \mu_B^b, \sigma_B^b\} = \{10, 6, 10, 6\}$ (background), $\theta_T = \{10, 10, 150, 30\}$ (tissue). For the artifact class we used different initializations for the upper ($\theta_A = \{200, 10, 200, 10\}$) and lower part ($\theta_A = \{120, 20, 150, 10\}$). The exact initialization values for each class are not critical as the expectation-maximization method uses these values only as a starting point for optimization. We used the following values to define the narrow bands: $\kappa_1 = 2\,mm$ (for shadow detection), $\kappa_2 = 1\,mm$ (for initialization of the lumen class in the Gaussian mixture model). κ_1 and κ_2 were selected as a narrow band around the centerline to ensure the selection of pixels inside of the lumen in case of high stenosis. The value of κ_2 is smaller because it is used for initializing the intensity distribution parameters of the lumen class; therefore it is important that only structures that belong to the lumen are selected. For the lumen contour refinement step, we chose $\kappa_3 = 5\,mm$ which is large enough to follow the typically observed local curvature of the initial detected contours. In Equation 1 for the penalty weighting factors we chose $\gamma_1 = 10$, which means 10% additional cost for a step, and $\gamma_2 = 1000$, which means 1% additional cost for each $1\,mm$ (10 pixels) away from the centerline. The lumen segmentation results were statistically analyzed using independent t-tests.

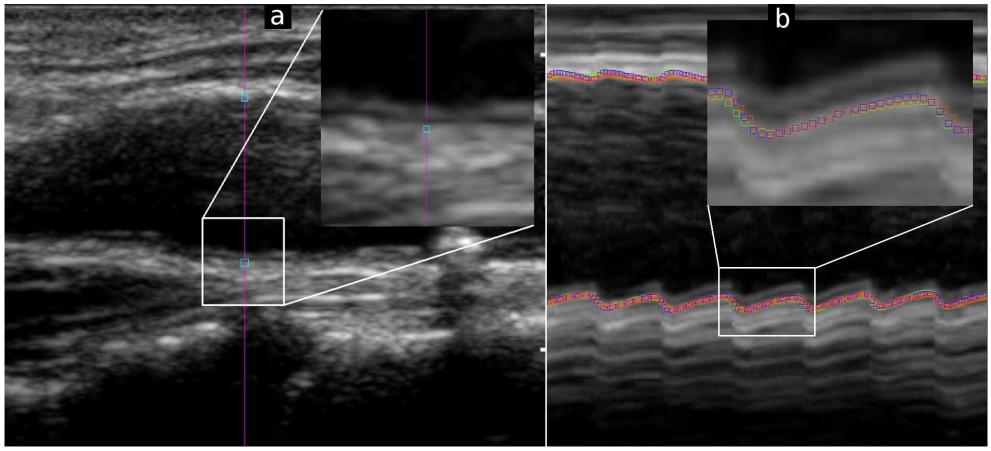

Figure 5.7: Selected line (pink) in the BMUS image (a) and the line profile across 150 times frames (b). The annotations marked by the observers are represented by green and blue points; the automated tracking is displayed in red.

5.4.3 Carotid Artery Distensibility

The distensibility measurements for *DC*-Line and *DC*-ROI were evaluated on the nine carotid arteries in dataset I' by comparing to manual measurements. For the manual *DC* measurement, we selected a line profile (Fig. 5.7a) approximately orthogonal to the centerline in the BMUS, and extracted it over 150 time frames (~7 seconds, ~7 cardiac cycles) in order to obtain a virtual representation of M-mode ultrasound (see Fig. 5.7b). Two observers (DC and ZA) traced the displacement of one point on the near and far wall of the artery in the virtual M-mode, while also inspecting the positions of the traced points on the BMUS images. Based on these annotations, we calculated *DC* for each cardiac cycle of the image sequence, and averaged the results over all cardiac cycles. The results obtained by the two observers, *DC*-Line and *DC*-ROI were compared against the ground truth with independent t-tests. Finally, to show the potential of the method for deriving more advanced arterial stiffness parameters, we show plots of the diameter evolution over time for a healthy section and a plaque section in each carotid artery.

5.5 Results

5.5.1 Nonrigid Motion Estimation

The results of the experiment evaluating the displacement of a point in the plaque are shown in Tab. 5.1, where the registration errors for NME vs. ground truth, the inter-observer variabilities (observers vs. ground truth), and the errors of the LRST

	NME	Obs. 1	Obs.2	Obs. 3	LRST
ε_x	99±74	74±21	93±82	64±70	87±32
ε_y	47±18	38±13	39±2	37±7	48±11
ε_{Euclid}	112±73	86±27	102±77	76±70	102±29

Table 5.1: Mean ± std. dev. of motion estimation accuracy (ε_x, ε_y and ε_{Euclid}) for NME, the three observers (Obs.) and the LRST method, evaluated in dataset I using a single point in plaque tracked over 150 time frames (all units are in μm).

	NME	Obs. 1 vs. Obs. 2
ε_x	217±112	270±64
ε_y	277±94	99±19
ε_{Euclid}	381±152	290±58

Table 5.2: Mean ± std. dev. of motion estimation accuracy for NME and two observers (Obs.), evaluated in dataset I' for three points selected on different sections of the carotid arteries over 100 time frames (all units are in μm).

method are reported. Fig. 5.8 shows the results for the entire range of registration parameters used to optimize NME. The lowest registration error was obtained with β = 2.5 mm × 2.5 mm × 3 $frames$, σ = 0.5, and ρ = 5. These optimum parameter settings were used for the experiment evaluating the displacements of the three points in the carotid wall, the results of which are shown in Tab. 5.2.

The results from Tab. 5.1 were subjected to an ANOVA test, comparing the error scores of NME, LRST and the observers. No statistical significance was found among groups. The results of Tab. 5.2 were compared with independent t-tests. Significant difference between NME and the interobserver variability was found for ε_y, but not for ε_x and ε_{Euclid}.

5.5.2 Lumen Segmentation

Figure 5.9 shows the carotid artery lumen segmentation results of Fig. 5.1. Tab. 5.3 shows the RMSE between manual segmentations of the two observers (IO = inter-observer variability), and between automated segmentation and the ground truth (AG = Automated vs. ground truth) in datasets I' and II, both for the epitome images and the randomly selected time-frames. In dataset I', the average RMSE for both upper and lower contours was 191±43μm for the epitome images and 234±36μm for the five randomly selected time-frames respectively. In dataset II, the average RMSE was 351±176μm for the epitome images.

Independent t-tests were performed to analyze the results shown in Tab. 5.3. Differences between IO and AG were not significant. The observed differences between upper and lower contour were significant for the epitome images in dataset I', both for IO and AG, and for the five time-frames for AG. Observed differences between dataset I' and II were only significant for AG in the upper lumen contour.

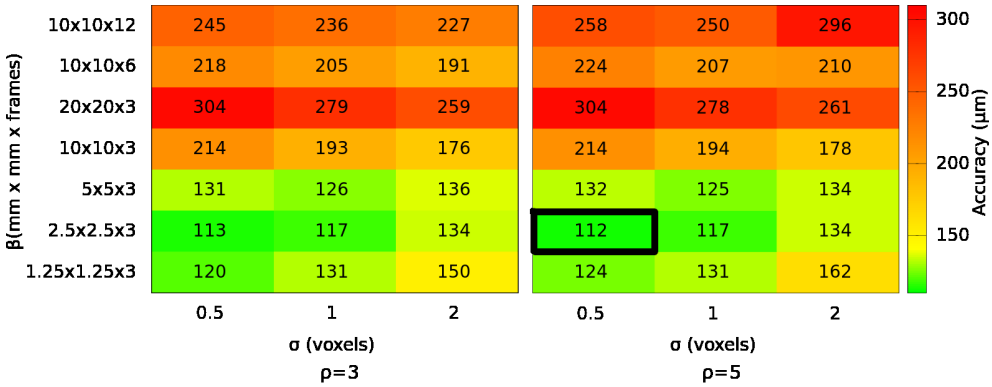

Figure 5.8: Parameter evaluation for motion estimation. For different number of resolutions (ρ = 3 and ρ = 5), degrees of smoothing σ, and spacings of the B-spline control points (β), the NME error ε_{Euclid} is shown. The optimum configuration is indicated by the black box.

	Upper Lumen Contour		Lower Lumen Contour	
	IO	AG	IO	AG
RMSE Dataset I'				
Epitome images	110 ± 50	110 ± 50	220 ± 140	260 ± 70
Five time-frames	190 ± 80	170 ± 60	270 ± 70	290 ± 30
RMSE Dataset II				
Epitome images	226 ± 196	294 ± 100	321 ± 185	408 ± 252

Table 5.3: Mean ± std. dev. RMSE for upper and lower contours in datasets I' and II (all units are in μm).

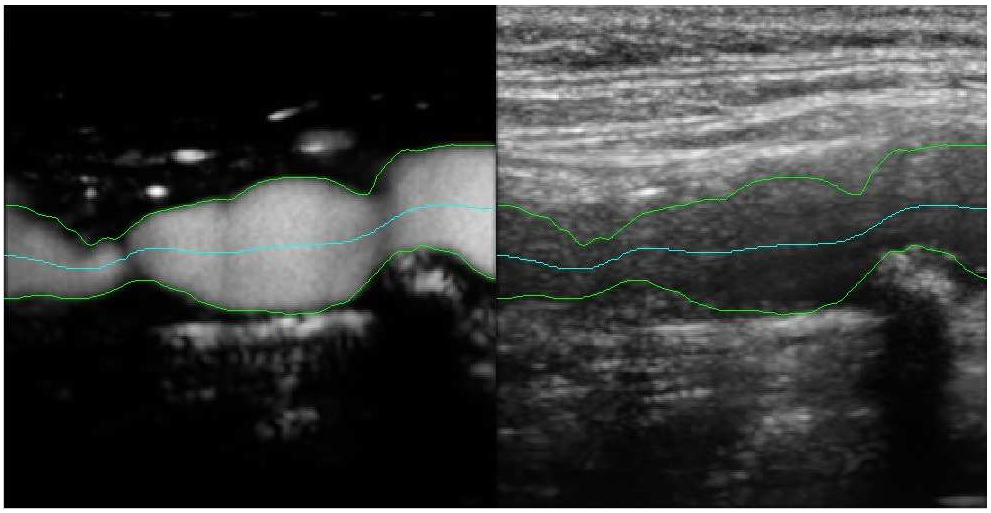

Figure 5.9: Detection of lumen contours for the image shown in Fig. 5.1a, containing speckle noise, reverberation artifacts and echolucent plaque in BMUS.

5.5.3 Distensibility Measurements

Figure 5.10 shows the carotid artery distensibility measurements based on manual and automated measurements, for dataset I'. In general, the automated distensibility results are conformable to the manual distensibility results. Furthermore, our distensibility coefficient results for 9 carotid arteries ($13.1 \pm 4.4[10^{-3}/kPa]$) are in accordance with the results reported in the literature ($10.5 \pm 4.4[10^{-3}/kPa]$) [125]. Whereas DC-Line tends to underestimate the distensibility, compared with the manual measurement, DC-ROI tends to overestimate. No statistically significant differences were found between the ground truth and the values obtained by the observers, DC-Line and DC-ROI.
Figure 5.11 shows plots of the diameter evolution over several cardiac cycles, for a healthy section and a plaque section in each carotid artery.

5.6 Discussion

We presented a lumen segmentation method which uses the combined information of BMUS and CEUS. First, motion compensation was applied to construct epitome images, which are used for segmentation. Subsequently, the segmentation and the nonrigid motion estimate are employed to calculate the arterial distensibility. Carotid artery distensibility is an example application of our proposed method. The method provides reliable segmentation of carotid lumen in subjects with atherosclerotic plaques, which can also be a basis for further processing such as segmentation of

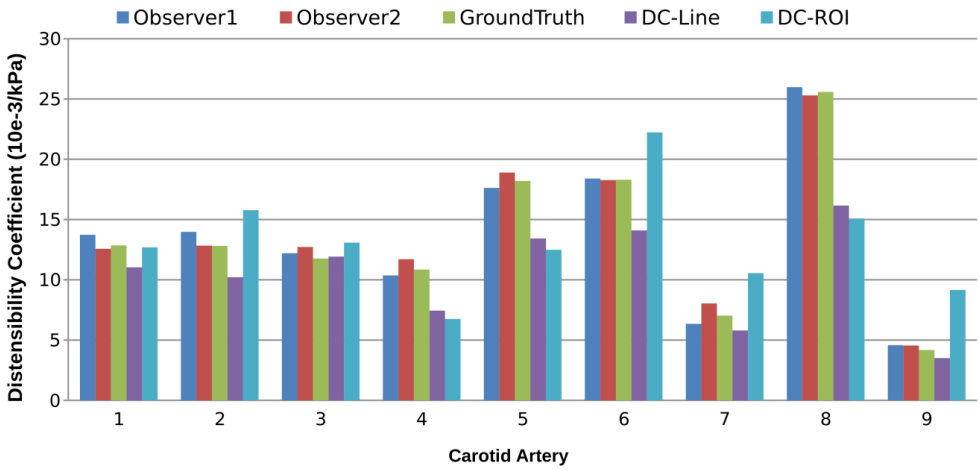

Figure 5.10: Comparison of carotid artery distensibility based on manual and automated measurements (*DC*-Line and *DC*-ROI)

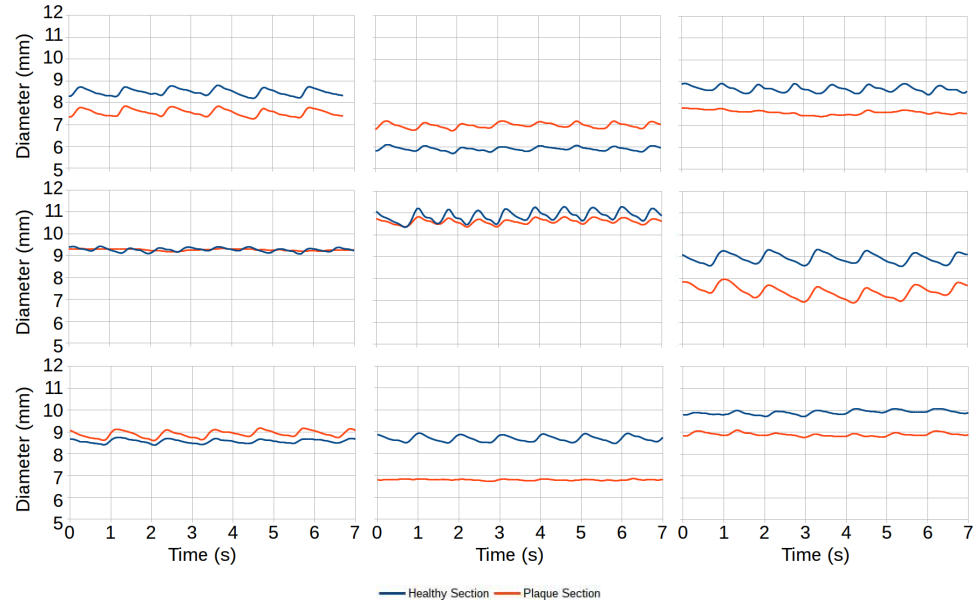

Figure 5.11: Arterial diameters vs. time for the nine patients in healthy and plaque sections. The measurements were performed with *DC-Line*.

plaque, assessment of plaque perfusion, and assessment of plaque vulnerability. Since the method requires contrast agent to be injected, we expect that it will be more likely used in the management of early stage disease with visible plaques than in large-scale screening of at risk populations.

The NME method provides results comparable with LRST, which tracks motion locally, whereas NME performs a nonrigid motion compensation of the entire image. The selection of the design parameters of the NME was performed by evaluating the motion of a point that is clearly visible across the whole sequence, situated within the atherosclerotic plaque. In this experiment, the RMSE between NME and the ground truth was around one pixel. Results acquired with NME are comparable with those obtained by observers and with LRST. However, tracking points situated elsewhere in the arterial wall led to larger errors. Both the interobserver variability and the NME vs. ground truth were around 3 pixels. These errors seem mainly due to the lack of clearly visible structures in the arterial wall, complicating the motion estimation, both manually and automatically, especially in the x-direction.

Our method segments accurately the lumen in images that are contaminated with noise in the lumen, artifacts (e.g. clutter or reverberation), and attenuation in the BMUS part and nonlinear propagation artifacts in the CEUS part. As shown in Tab. 5.3, the errors between automated and ground truth segmentations of dataset I' are in the same order as the error between two observers. This means our method is as good as manual delineation of the lumen contours for dataset I'. The error in the lower lumen contour is higher than the error in the upper contour for epitome images of dataset I'. A possible cause for this is the (remaining) influence of the pseudo-enhancement in the lower contour, which makes segmentation more difficult. Therefore, the interobserver variability for the lower contour is also higher than the variability for the upper contour in dataset I'. As seen in Tab. 5.3, the errors between automated and ground truth segmentations in dataset II are in the same order as the error between two observers. However, the errors in dataset II appear higher than the errors in dataset I' (although the difference was only significant for the automatic segmentation accuracy in the upper contour). This may be caused by the presence of severe stenosis and heavy shadowing due to calcifications in dataset II. The shadowed regions might not only cause larger errors, but they also complicate manual segmentation. As stated before, it has been reported that the lumen segmentation methods using only BMUS have limitations in presence of atherosclerotic plaque [119–121]. The epitome BMUS and CEUS images obtained through NME result in better lumen identification and noise suppression in the atherosclerotic carotids. This provides a clearer separation of the lumen-intima interface, leading to accurate lumen segmentation. To best of our knowledge, our work is the first to use the combination of BMUS and CEUS to segment the lumen, which deals with all the difficulties that have been mentioned in the literature so far for atherosclerotic carotid arteries.

The artifact detection step based on the joint histogram analysis requires a relatively large set of user-defined parameters (Θ). Nevertheless, the exact values are not crucial, since they are used only as initialization parameter for an iterative expectation-maximization approach that further optimizes these joint histogram parameters. The remaining parameters of the lumen segmentation method were defined based on geometrical considerations, taking into account the typical anatomy of the carotid artery,

and based on initial trial-and-error experiments on dataset I. The experimental results for dataset II confirm that the method was not "over-tuned" on dataset I. As seen in Fig. 5.5, the method handles severely stenosed cases.

Our proposed method is also able to measure the carotid artery distensibility coefficient *DC,* and potentially also more advanced measures of arterial stiffness. Two methods for measuring distensibility were investigated: *DC*-Line and *DC*-ROI. In Fig. 5.10, it was shown that the *DC*-ROI method overestimated the *DC* in several carotid arteries, especially case 7 and 9. This is due to the difficulty in selecting a ROI that is fully free from plaque around the selected line. Having a partial inclusion of plaque in the ROI will influence the distensibility results as the stiffness of the wall is not well-defined in plaque regions. Distensibility is used as a measure of local vessel stiffness by calculating circumferential stretching, assuming a circular cross section and a fixed radius. This is by definition not the case in a stenosis, and the resulting number cannot be compared to a normal region next to it. The *DC*-Line method yielded results more similar to the inter-observer variability. The observers' distensibility annotations were performed on the virtual M-Mode, which represents a single intensity profile across time. The observers tend to agree more on tracking the brightest layer across the time frames in this visualization than in the 2D+t visualization, which was employed for the manual annotations in the other experiments. It is important to notice that it is not possible to track a point displacement in all directions on the virtual M-Mode. Inspection of temporal evolution of the arterial diameters (Fig. 5.11) suggests that the diameter variation for some plaques is highly similar to the healthy sections, while for other plaques the diameter variation is lower in the plaque sections than in the healthy sections. Further studies on larger patient groups should investigate the relations to plaque properties and potential associations with clinical outcomes.

Our proposed method is currently implemented for offline postprocessing. The NME takes around 9 minutes on a Intel Xeon CPU E5520. Segmentation of the carotid lumen in the epitome image takes less than a minute. Transforming the detected contours from the epitome image to all time frames takes around 3 minutes. Measuring distensibility for 1 cm length of vessel (about 100 cross-sectional lines) takes less than a minute for a 10 second cine clip.

A distinct advantage of our method is that the operations can be performed without user interaction; we just selected a ROI to perform the distensibility evaluation. As a limitation, our data acquisition was not optimized for the purpose of assessment of arterial distensibility, but optimized for plaque perfusion assessment. This may explain some of the erroneous distensibility results for individual subjects. We showed that our distensibility results are in the same order as presented in the literature. However, these comparisons should be made with care, as stiffness measures may depend on the blood pressure values. Therefore, the current results should not be used yet for a per-subject distensibility assessment. The proposed method for quantifying the lumen geometry over time might also be useful for other applications such as central pressure estimation [142–144].

Our method is fully automatic for a single carotid branch. We only focused on one branch and excluded carotid arteries with bifurcation and cases with jugular vein presence. As a future work, we would like to include automatic vessel detection in

presence of jugular vein and carotid arteries with bifurcation. For these cases, it will be necessary to modify the automated centerline detection stage. Also, we would like to add media-adventitia layer detection, including plaque segmentation.

5.7 Conclusions

We have performed an accurate lumen segmentation of the carotid artery based on combined BMUS and CEUS images. Our segmentation approach enables the user to detect the lumen-intima border of the artery which can hardly be detected in standard BMUS. The extraction of the motion pattern from the image sequence leads to epitome images that facilitate the lumen segmentation, and furthermore, the assessment of the arterial distensibility, or other, more advanced arterial stiffness parameters. The method is automated, an extensive evaluation was performed, and the results are accurate. Therefore, our method could become a valuable tool for the analysis of atherosclerotic carotid arteries.

Acknowledgements

We wish to thank Dr G. L. ten Kate for performing the patient scans.

6

Fully Automated Carotid Plaque Segmentation in Combined B-mode and Contrast Enhanced Ultrasound

Abstract: Carotid plaque segmentation in B-mode ultrasound (BMUS) and contrast-enhanced ultrasound (CEUS) is crucial to the assessment of plaque morphology and composition, which are linked to plaque vulnerability. Segmentation in BMUS is challenging because of noise, artifacts and echo-lucent plaques. CEUS allows better delineation of the lumen but contains artifacts and lacks tissue information. We describe a method that exploits the combined information from simultaneously acquired BMUS and CEUS images. Our method consists of nonrigid motion estimation, vessel detection, lumen–intima segmentation and media–adventitia segmentation. The evaluation was performed in training (n = 20 carotids) and test (n = 28) data sets by comparison with manually obtained ground truth. The average root-mean-square errors in the training and test data sets were comparable for media–adventitia (411 ± 224 and $393 \pm 239\,\mu m$) and for lumen–intima (362 ± 192 and $388 \pm 200\,\mu m$), and were comparable to inter-observer variability. To the best of our knowledge, this is the first method to perform fully automatic carotid plaque segmentation using combined BMUS and CEUS.

Based upon: Zeynettin Akkus*, **Diego D.B. Carvalho***, Stijn C.H. van den Oord, Arend F.L. Schinkel, Wiro J. Niessen, Nico de Jong, Antonius F.W. van der Steen, Stefan Klein, Johan G. Bosch, "Fully Automated Carotid Plaque Segmentation in Combined Contrast-Enhanced and B-Mode Ultrasound", published in *Ultrasound in medicine & biology*
**both authors contributed equally to this research*

6.1 Introduction

Cerebrovascular disease ranks as the third leading cause of death worldwide [91]. The carotid arteries are two vessels located at both sides of the neck. They are responsible for providing blood to the brain and muscles of the face. Each carotid starts as a common carotid artery (CCA), which forks into two branches: internal carotid artery (ICA) and external carotid artery (ECA). The incidence of ischemic strokes is highly associated with the rupture of atherosclerotic plaques in the carotid artery [60]. Rupture can cause severe vessel obstruction as a result of distal propagation of a thrombus [92]. The formation of an atherosclerotic plaque occurs because of atherosclerosis, which is a process of inflammation in the arterial wall. To assess the risk of rupture, current clinical practice relies heavily on the degree of stenosis. However, there is an increasing awareness that it is not the size of the plaque, but its composition that is related to risk of rupture. For example, intra-plaque neovascularization (IPN) has been linked to plaque vulnerability in several histopathologic studies [145–147]. Ultrasound has been widely used as a standard tool for inexpensive and non-invasive diagnosis of carotid plaque morphology and composition. Different ultrasound techniques have been used such as standard B-mode ultrasound (BMUS), color Doppler and contrast-enhanced ultrasound (CEUS) [109]. For the accurate assessment of the degree of stenosis and plaque composition, objective and reproducible segmentation of carotid plaques from ultrasound images is a crucial step.

So far, carotid plaque segmentation has been performed mainly on standard BMUS images [121, 148, 149]. However, in standard BMUS images, this is difficult and can be inaccurate because of the noise in the lumen, artifacts, lumen irregularity and echo-lucent plaques. Color Doppler provides an approximate view of blood flow in the lumen, but its result is dependent on user-controlled settings (e.g., Doppler gain, wall filter and velocity range) and local direction of flow. This may overestimate or underestimate the lumen, and thus segmenting plaques from color Doppler images would lead to inaccurate results. CEUS allows better delineation of the carotid lumen than standard BMUS [109, 114, 115]. CEUS provides visualization of the vessel lumen regardless of flow velocity and direction by the use of ultrasound contrast agents. However, CEUS contains specific artifacts and contains no tissue information [132], which make the plaque segmentation difficult.

Some studies have addressed carotid plaque segmentation in longitudinal vessel cross sections visualized with standard BMUS [121, 148, 149]. Loizou et al. [148] described a method based on gray-scale normalization, speckle reduction filtering and snake segmentation. The method compares the accuracy of four snake techniques in 80 patients. The method is automatic and uses color Doppler images to avoid the difficulties in echo-lucent plaque detection in BMUS and to extract the initial snake contour. Several limitations of the study were reported: (i) overlap of color flow with wall or plaque tissue; (ii) lack of information for low-velocity regions; (iii) convergence of snake to false local minima; and (iv) exclusion of echo-lucent and calcified plaques. Loizou et al. [149] described another plaque segmentation method based on snake segmentation, in which the plaque is segmented in different time frames, according to a manual initialization in the first time frame. Destrempes et al. [121] presented a plaque segmentation method that models the intensities of vessel lumen, plaque

and adventitial wall with a mixture of three Nakagami distributions. The mixture parameters were first estimated with an expectation–maximization (EM) algorithm, and this yielded the likelihood of a Bayesian segmentation model. They also obtained the motion fields in the image sequence using an optical flow technique and used it as a prior of the Bayesian model which includes a local geometric smoothness constraint. The method was tested on 93 sequences of 33 patients (in total 8988 images). The method is semi-automatic because it requires manual segmentation of plaque in the first frame.

Because of the noise, artifacts and echo-lucent plaques, the fully automatic segmentation of plaques in BMUS images remains a challenge. Two specific types of plaque (I and V according to the classification of Nicolaides et al. [150] are particularly challenging. Type I plaques are uniformly echo-lucent, making it very difficult to differentiate their intensity from that of the lumen. Type V plaques present with calcified caps that cause shadows.

Contrast-enhanced ultrasound allows delineation of the vessel lumen, but it also enables the detection of IPN. The ultrasound contrast agent enters the plaque neovasculature and is seen as intermittently appearing bright spots. For assessment of IPN from CEUS images, a first step is delineation of the plaque region of interest (ROI). Several studies have used manual delineation, which is subjective and tedious [151–154] . As tissue information is absent in CEUS images, automatic plaque segmentation is extremely difficult. Some studies have addressed plaque segmentation in CEUS images [155, 156]. Hoogi et al. [155] segmented the lumen with an active contour method and fit a parabola to the arterial wall, enabling plaque segmentation in a single frame. A limitation of the method is the fact that media–adventitia is not segmented but estimated by a parabola. Molinari et al. [156] performed automatic segmentation of the plaque and characterization of its tissue in BMUS enhanced with ultrasound contrast agent. The plaque was segmented by a k-means classification algorithm and subsequent application of a deformable model. They reported that use of contrast-enhanced BMUS overcomes the difficulties encountered in segmenting echo-lucent plaques in standard BMUS. However, the method was evaluated on only five echo-lucent plaques. Zhang et al. [157] proposed a method in CEUS images that uses spatiotemporal analysis and snakes. The method uses the spatial correlation of time–intensity curves to detect initial contours of plaques, and then deforms them to refined contours with a gradient vector flow snake. This method requires a user-defined ROI around the plaque in the CEUS image to simplify the segmentation process. In another study, Zhang et al. [158] presented interactive plaque segmentation in CEUS. A mean image with improved signal-to-noise ratio (SNR) was obtained by time-averaging the image sequence, and interactive plaque segmentation was performed in the temporal mean image. The user needs to indicate points on the plaque border and B-spline interpolation of the discrete points is used to get a smooth closed curve. No motion compensation is performed, and the segmentation is fully manual.

Several algorithms have been described that segment intima–media thickness (IMT) in asymptomatic carotids in BMUS. Because they do not consider the presence of atherosclerotic plaques in the carotids, they are not applicable to plaque segmentation. Liang et al. [159] presented a method to detect arterial boundaries in a userselected ROI through multiscale dynamic programming (DP). The cost function is constructed

from a weighted sum of features and geometric characteristics extracted from a manually segmented training set. The method does not segment IMT in the presence of plaque. Cheng and Jiang [160] used a dual dynamic programming (DDP) approach to detect the intima and adventitia layers of the common carotid wall. The method is semiautomatic and requires the manual selection of a ROI containing the layers. Destrempes et al. [111] presented a method that segments the IMT through EM in a manually selected ROI. The EM is initialized using three Nakagami distributions to represent the intima–media layers, the lumen and the adventitia. The method was evaluated on healthy common carotids. Teynor et al. [127] used the DDP method of Zhou et al. [161] in conjunction with manual user interactions to track the systolic and diastolic IMT of asymptomatic carotids in a manually defined ROI. Zhou et al. [161] described a method that merges different techniques to segment the intima–media layer and presents a novel DP approach, dual line detection (DLD). An edge map is created from the output of two edge detectors in different scales. The DLD is applied on local segments of this edge map. In the end, the calculated contours are employed as an input for a snake segmentation model.

Some studies have also investigated automatic carotid vessel detection in BMUS, which could be used as a first step to automate plaque segmentation. Molinari et al. [156] tracked the adventitia layer by using geometric feature extraction, line fitting, and line classification of the CCA. The method is sensitive to inhomogeneities in lumen intensities. Rocha et al. [162] employed DP to automatically extract the lumen axis of the CCA. The proposed methods are limited to the common carotid artery, and thus, multibranch carotid artery detection still remains a challenge.

Previous studies worked on only BMUS or only CEUS, and therefore, they were vulnerable to difficulties associated with these imaging modalities. This limits their performance. BMUS and CEUS present complementary information. In this study, we exploit the combined information from simultaneously acquired BMUS and CEUS images to overcome the difficulties of plaque segmentation in previous studies. An example of side-by-side simultaneously acquired BMUS and CEUS images and a schematic of arterial wall layers are illustrated in Figure 6.1. The advantage of this combination is that CEUS reveals a better delineation of the lumen, whereas BMUS provides the visualization of tissues. Because CEUS does not contain any information about the tissues, the combination with BMUS is necessary to accurately segment the plaque. We propose a novel and fully automatic carotid plaque segmentation method that overcomes the difficulties encountered in the separate use of BMUS and CEUS.

6.2 Methods

In our study, we use simultaneously acquired sideby-side BMUS and CEUS image sequences (a time frame is seen in Fig. 6.2). Simultaneous BMUS and CEUS imaging leads to two 2-D+time (2-D+t) image series, $I_{BMUS}(\mathbf{s}, t)$ and $I_{CEUS}(\mathbf{s}, t)$, where $\mathbf{s}$ is a spatial coordinate (x, y) and t is the time frame index with $t = 1...\tau$ (τ = number of time frames). Our proposed segmentation method for carotid plaques consists of three main steps: non-rigid motion estimation and compensation, automated vessel detection and plaque segmentation. Figure 6.3 is a flowchart of the method.

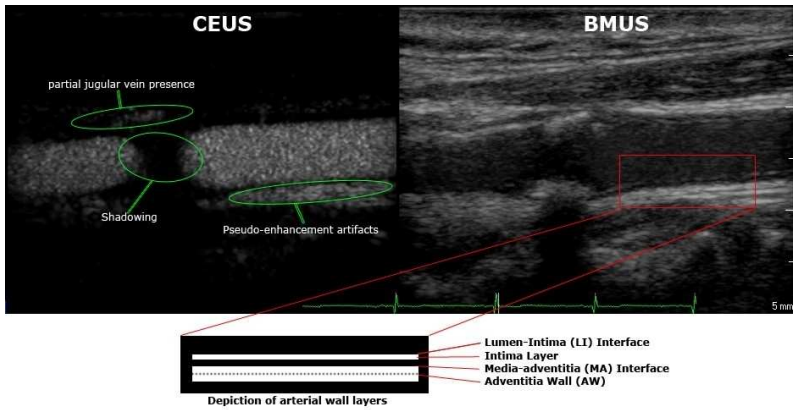

Figure 6.1: Simultaneously acquired BMUS and CEUS images with typical artifacts and schematic depiction of arterial wall layers. BMUS = B-mode ultrasound; CEUS = contrast-enhanced ultrasound.

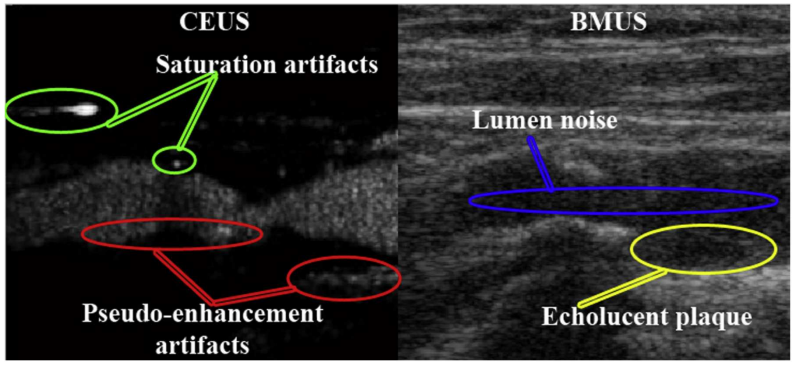

Figure 6.2: Single time frame of simultaneously acquired BMUS and CEUS images indicating the challenges of plaque segmentation in BMUS and CEUS images. BMUS = B-mode ultrasound; CEUS = contrast-enhanced ultrasound.

6.2.1 Non-rigid motion estimation and compensation

In a previous work (Carvalho et al. 2014), we proposed a non-rigid motion compensation method for simultaneously acquired BMUS and CEUS image sequences. As the first step in our plaque segmentation method, we obtain single BMUS and CEUS "epitome" images $\left(\bar{I}_{BMUS}(\mathbf{s}), \bar{I}_{CEUS}(\mathbf{s})\right)$ (Fig. 6.4a, b) with improved SNR by averaging the image intensities of each pixel over time in the motion-compensated BMUS/CEUS image sequences $(I_{BMUS^*}(\mathbf{s},t), I_{CEUS^*}(\mathbf{s},t))$. In the proposed motion compensation method, we estimate the non-rigid deformation $(T(\mathbf{s},t))$ of the carotid over time from the BMUS image sequence and subsequently compensate the motion in both the BMUS and CEUS image sequences. The method performs a groupwise registration of the entire 2-D+t data set. It produces a non-rigid motion estimate on the complete image, differently than existing local motion estimation techniques in ultrasound [128–131]. The deformations are modeled by a nonrigid 2-D+t B-spline transformation, ensuring smoothness in both the spatial and temporal dimensions. An adaptive stochastic gradient descent optimizer [85] is employed to calculate the transformation parameters that minimize a dissimilarity measure based on the variance of the intensities at corresponding spatial locations. The non-rigid motion compensation method is described and evaluated in detail in Carvalho et al. [163], see also Chapter 5. All further processing is performed on the epitome images $\bar{I}_{BMUS}(\mathbf{s})$ and $\bar{I}_{CEUS}(\mathbf{s})$.

6.2.2 Automated vessel detection

Before plaque segmentation, we perform automated detection of vessels in the BMUS and CEUS epitome images. CEUS images provide only perfusion information on vessels, which avoids the confusion of vessel-like anatomic structures in the BMUS images. However, CEUS presents artifacts that might cause false detection. We assume that there is at least one vessel in the image plane as images are acquired for the carotid examination. We further assume the proximal part of the carotid (CCA) is on the right side of the image, according to the standardized scanning protocol. The bifurcation may or may not be within the field of view, and the jugular vein may or may not be visible. Figure 6.4 illustrates the possible scenarios. To identify the arteries of interest (CCA, ICA, ECA), we propose a four-stage algorithm, consisting of: (i) rough lumen identification, (ii) morphologic operations, (iii) vessel profile scanning and (iv) heuristic classification of vessel candidates.

6.2.2.1 Rough lumen identification.

We apply an intensitybased classification in the BMUS and CEUS epitome images to identify true lumen and circumvent artifacts as described in detail in our previous study [164]. On the basis of the typical intensity distribution of classes (background, tissue, lumen and artifacts) in the joint histogram of BMUS and CEUS epitomes, we initialize these classes and feed them into an EM algorithm. This results in a fuzzy segmentation, indicating for each pixel the probability that it is located in a lumen.

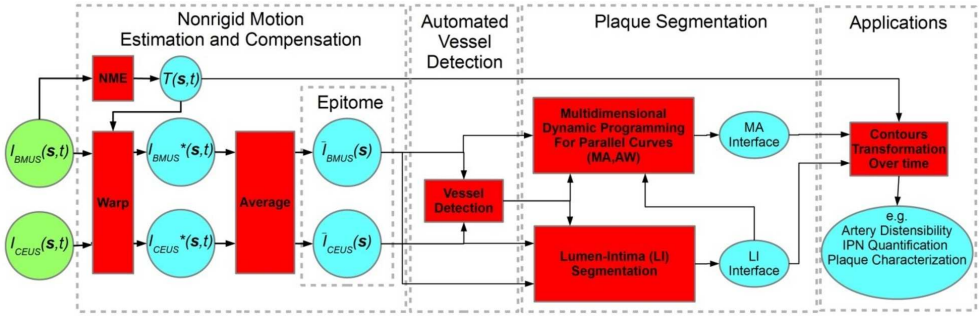

Figure 6.3: Flowchart of the method, comprising inputs (green), operations (red) and outputs (blue). $T(\mathbf{s}, t)$ = transformation obtained from BMUS with NME. $I_{BMUS^*}(\mathbf{s})$ and $I_{CEUS^*}(\mathbf{s})$ = motion-compensated BMUS and CEUS, respectively; $\bar{I}_{BMUS}(\mathbf{s})$ and $\bar{I}_{CEUS}(\mathbf{s})$ = epitome images; $\mathbf{s}$ =spatial position (x, y) within the image; t = time frame index; BMUS = B-mode ultrasound; CEUS = contrast-enhanced ultrasound; MA = media–adventitia; LI = lumen–intima; AW = adventitia wall; NME = non-rigid motion estimation.

6.2.2.2 Morphologic processing.

In this step, morphologic opening using a disk-shaped structuring element with radius 1 mm is applied to remove noise or small objects, such as remaining artifacts in the probabilistic lumen segmentation obtained in the previous step. We assume that after this aggressive morphologic opening, any isolated artifacts have been eliminated from the probabilistic lumen segmentation. Next, we convert this probabilistic segmentation to a binary image using Otsu's global image threshold. Subsequently, we extract the edges from the binary image using a Canny edge detector.

6.2.2.3 Vessel profile scanning.

In this step, we vertically scan the edge map at each x position (i.e., column), from top to bottom, and record each pair of edge points. Assuming that these pairs of edge points represent the boundaries of a vessel, we calculate the center points and connect them to each other from column to column (left to right) based on the closest Euclidean distance. To compensate for missed regions caused by acoustic shadowing or out-of-plane artifacts, we use linear interpolation between detected center points for empty regions.

6.2.2.4 Heuristic classification of vessel candidates.

We classify the detected candidates in a heuristic manner. In the most extreme case, a maximum of three vessels (jugular, internal and external carotid arteries, as seen in Fig. 6.3d) can be seen in the field of view of 3- or 4-cm depth in the standard carotid B-mode ultrasound. The possible combinations of detected vessels are as follows:

1. If only one vessel is detected (see Fig. 6.3a), it is considered the carotid artery.

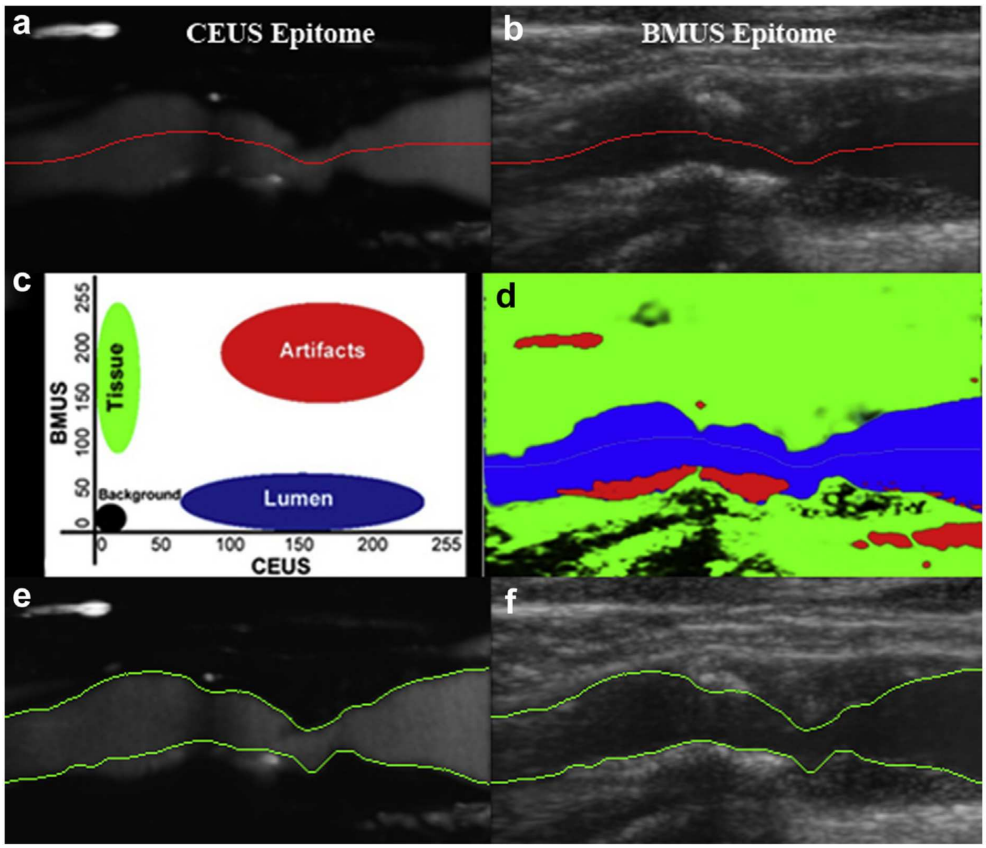

Figure 6.4: Steps in lumen–intima interface detection for the given example in Figure 6.2. (a) CEUS epitome. (b) BMUS epitome. (c) Joint intensity histogram. (d) Result of intensity classification. (e, f) refined lumen–intima interface for (e) CEUS and (f) BMUS. BMUS=B-mode ultrasound; CEUS=contrast-enhanced ultrasound.

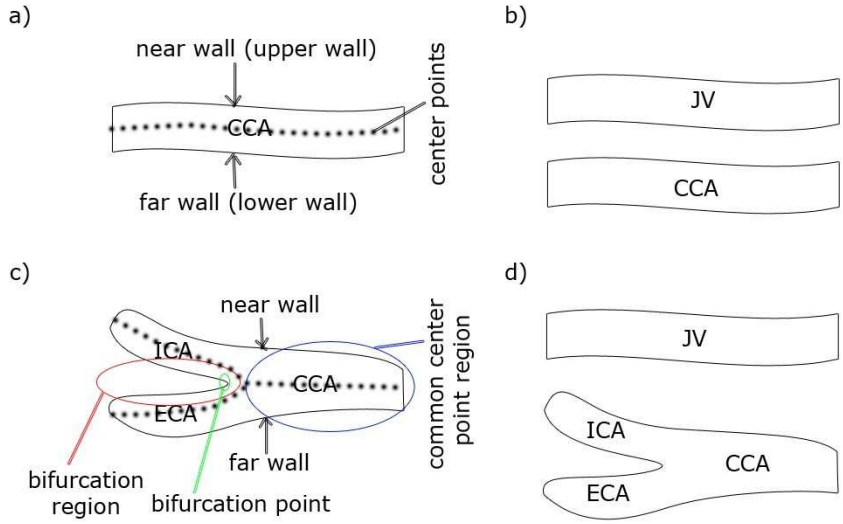

Figure 6.5: Possible scenarios of vessel geometry visible in the ca- rotid ultrasound images. (a) CCA only (a). (b) JV and CCA. (c) Bifurcated carotid artery. (d) JV and bifurcated carotid artery. CCA = common carotid artery; ECA 5 external carotid artery; ICA = internal carotid artery; JV = jugular vein.

2. If two vessels are detected, these may be a jugular vein and a carotid artery (see Fig. 6.3b) or a bifurcated artery (see Fig. 6.3c). To discriminate between these two cases, we analyze the detected center point sets for the two vessels. If they do not have a "common center points region," that is, a part where the centerlines merge, or if this region is less than 5 mm long, we consider these two vessels as separate vessels (jugular and carotid). In this case, the topmost one is the jugular vein and the bottom one is the carotid artery. If the common center points region (see Fig. 6.3c) is at least $5\,mm$ long, we consider it a carotid bifurcation. In this case, the x-position where the centerline undergoes the largest vertical shift indicates the bifurcation point. The upper branch is the ICA.

3. If three vessels are detected (see Fig. 6.3d), we consider the topmost as the jugular vein and both of the others as a bifurcated artery, which consists of internal and external carotid branches.

Having identified the arteries of interest, on the basis of the procedure described above, we proceed with vessel wall segmentation. In the case of a single-branch carotid artery detection (see Fig. 6.3a, b), we segment the lumen– intima (LI) and media–adventitia (MA) interfaces of the near wall (upper wall) and far wall (lower wall) of the artery as described in the following sections. In the case of a bifurcated carotid artery detection (see Fig. 6.3c, d), we segment the LI and MA interfaces of the near wall, the far wall and the bifurcation region (see Fig. 6.3c) of the artery.

6.2.3 Plaque segmentation

To detect the carotid plaques, we sequentially segment LI and MA interfaces of the upper and lower carotid walls and apply the Mannheim consensus [165] for delimitation of the plaque. The Mannheim consensus established the metrics to identify the plaque: "Plaque is defined as a focal structure that encroaches into the arterial lumen by at least $0.5\,mm$ or 50% of the surrounding IMT value or demonstrates a thickness $>1.5\,mm$ as measured from the media–adventitia interface to the intima–lumen interface." In the following sections, we briefly describe LI interface segmentation adopted from our previous work [164] and MA interface segmentation using multi-dimensional dynamic programming (MDP) for parallel curves. The MA interface segmentation is the main focus of this study. The LI and MA interfaces obtained in the epitome images can be warped back to each time frame using the transformation $T(\mathbf{s}, t)$ resulting from the non-rigid motion estimation described under Non-rigid Motion Estimation and Compensation. This allows us to follow plaques over time and also allows possible applications such as arterial distensibility, IPN quantification and plaque characterization.

6.2.3.1 Lumen–intima interface segmentation.

We perform LI interface segmentation of the carotid artery on the epitome images $\bar{I}_{BMUS}(\mathbf{s})$ and $\bar{I}_{CEUS}(\mathbf{s})$. Our LI segmentation method, which is explained in detail in Akkus et al. [164], consists of five steps: centerline estimation, detection of shadowing,

detection of artifacts, graphbased segmentation and refinement of lumen contours. To segment a single-branch carotid artery, we perform the following steps.

First, we estimate the centerline of the carotid artery by applying a 2-D Gaussian smoothing filter to the CEUS epitome image and finding a minimum cost path, using dynamic programming in the x-direction [131, 135]. Second, we detect the shadow regions by fitting a linear curve to the mean intensity profile of a band around the centerline and neutralize these regions by assigning the same cost value. We then re-detect the centerline (Fig. 6.4a, b). Third, we detect the CEUS-specific pseudo-enhancement artifacts [132] and saturation artifacts [151] by using a joint intensity classifier for BMUS and CEUS epitomes and suppress them in the CEUS epitome (Fig. 6.4c, d). Fourth, we detect the upper and lower LI interfaces in the CEUS epitome using dynamic programming. Fifth, we refine the upper and lower LI interfaces by resampling the neighborhood of the interfaces with subpixel precision and applying dynamic programming (Fig. 6.4e, f).

In the case of a carotid bifurcation, we detect two separate centerlines for ICA and ECA. We use the bifurcation point that was obtained in the vessel detection step (see Automated Vessel Detection). Left of that point, we mask the quadrant to the lower left side of the bifurcation point and detect the centerline for the upper branch (ICA) plus the common carotid as explained above for a singlebranch artery. Then we mask the upper left quadrant and detect the second centerline (ECA+CCA). Subsequently, we detect the shadow regions and artifacts as explained above for a single-branch carotid artery. Last, we detect the upper LI interface of the bifurcated artery from the ICA+CCA centerline and the lower LI interface from the ECA+CCA centerline. For the LI interfaces of the bifurcation region, we detect the upper LI interface in the region between the ICA centerline and bifurcation line, and the lower LI interface in the region between the bifurcation line and ECA centerline (Fig. 6.3c).

6.2.3.2 Media–adventitia interface segmentation.

As tissue information is suppressed in CEUS images, it is not possible to segment the MA interface from CEUS images. We therefore segment the MA interface from the simultaneously acquired BMUS epitome image, using MDP for detection of parallel curves [160, 161]. The layers of the arterial wall in a BMUS image are illustrated in Figure 6.1. As seen in Figure 6.1, the MA interface is the transition from the media layer to the adventitia wall, characterized by a strong outward (from lumen) intensity gradient. The adventitia wall is seen in the BMUS image as the brightest part of the vessel wall. We define the centerline of this structure as the adventitia wall (AW) position. The MA interface runs in parallel with the AW and they are assumed to possess the following characteristics: intra-curve smoothness—both the MA interface and AW should be a smooth curve; inter-curve smoothness—the MA interface and AW should be nearly parallel within a specific distance; intima-media (IM) distance—the distance between the MA and LI interfaces is between 0.3 and 1.5 mm [165, 166] in a vessel wall free from plaques and will increase in the case of plaques.

6.2.3.3 Multidimensional dynamic programming for parallel curves.

The objective of MDP for parallel curves is finding two curves that minimize a certain cost function. Let $\bar{I}_{BMUS}(\mathbf{s})$ be of size $X \times Y$. The MA interface and the AW run from left to right (in the x-dimension) and are described by two coordinates y_{MA} and y_{AW} at each x-position, with $1 \leq y_1, y_2 \leq Y$. We find the optimal interfaces by minimizing a dedicated cost function composed of appearance and geometry-related terms. The appearance terms simulate that the MA curve traverses high outward gradient locations and that the AW curve passes through bright regions. The geometry terms favor solutions that satisfy the three above-mentioned characteristics.

The appearance cost of the MA interface (C_{MA}) is calculated by applying a Gaussian derivative filter with standard deviation of $0.3\,mm$, which gives the y-directional gradient of the BMUS epitome image $\widetilde{\nabla_y I}_{BMUS}(\mathbf{s}) = \pm\nabla_y G * \bar{I}_{BMUS}(\mathbf{s})$, where the sign is chosen such that gradients pointing outward from the lumen centerline are positive. The cost of the MA interface passing through coordinate s is then defined as $C_{MA} = 1 - \widetilde{\nabla_y I}_{BMUS}(\mathbf{s}) / \max_s \widetilde{\nabla_y I}_{BMUS}(\mathbf{s})$. The cost representing the AW is defined as $C_{AW} = 1 - \bar{I}_{BMUS}(\mathbf{s}) / \max_s \bar{I}_{BMUS}(\mathbf{s})$. For both C_{MA} and C_{AW}, 0 is the optimal cost. The combined appearance cost is calculated by taking the average: $C(x, y_1, y_2) = (C_{MA}(x, y_1) + C_{AW}(x, y_2))/2$.

Multidimensional dynamic programming is defined by minimizing a cumulative cost function ($\widehat{C}$), which combines the appearance costs with several geometry related terms:

$$\begin{aligned}\widehat{C}(x, y_1, y_2) = \min_{\delta_1, \delta_2 \epsilon \{-1,0,1\}} \quad & \big[\widehat{C}(x-1, y_1-\delta_1, y_2-\delta_2) + C(x, y_1, y_2)\cdot \\ & (1+\alpha_1)^{\delta_1} \cdot (1+\alpha_1)^{\delta_2} + \\ & (1 + \alpha_2 \cdot |(y_1 - y_2) - (\delta_1 - \delta_2)|) + \\ & \alpha_3 \cdot P\,(x, y_1 - y_{LI}\,(x))\big]\end{aligned} \tag{6.1}$$

subject to $d_{min} \leq (y_2 - y_1) \cdot R \leq d_{max}$and $2 \leq x \leq N$, where δ_1 and δ_2 are the step sizes (in pixel units) in the y_1 and y_2 directions, α_1 and α_2 are weights for intra-curve smoothness and inter-curve smoothness, respectively, P is an IMT penalty term, $y_{LI}\,(x)$ is the lumen–intima position, α_3 is a weighting factor for the IMT penalty term, d_{min} and d_{max} are the minimal and maximal distance (in mm) between the MA interface and the AW and R is pixel spacing in millimeters. The MDP procedure for detection of parallel curves subject to the constraint $d_{min} \leq (y_2 - y_1) \cdot R \leq d_{max}$ is illustrated in Figure 6.6.

The minimum and maximum allowed distances (d_{min} and d_{max}) between the MA interface and the AW are considered to be 0.3 and $1.5\,mm$, respectively, based on adventitial wall thickness measurements reported in previous studies (O'Leary and Bots 2010; Skilton et al. 2011) [166, 167]. The IMT penalty term $P\,(x, y_1 - y_{LI}\,(x))$ encodes prior information on the expected distance between MA and LI, $y_1 - y_{LI}\,(x)$, taking into account the possible presence of plaque at position x. The IMT penalty function is defined as a combination of two sigmoid functions and an uncertainty region as seen in Figure 6.7 and the equation

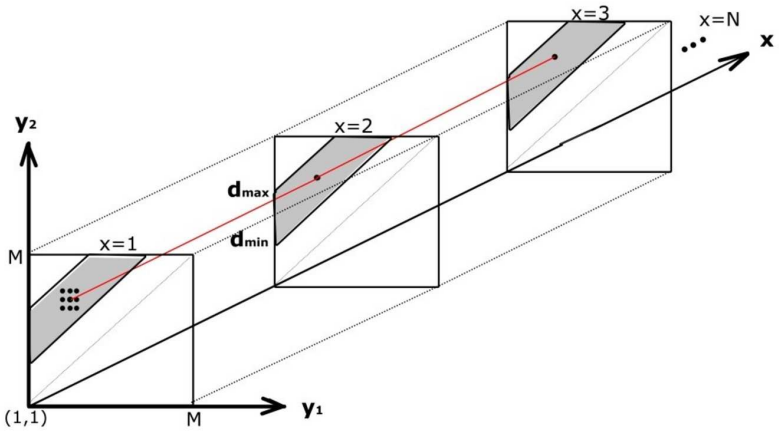

Figure 6.6: Multidimensional dynamic programming for a given image of size $X \times Y$ to detect parallel curves subject to the constraint $d_{min} \leq (y_2 - y_1) \cdot R \leq d_{max}$ (gray region). y_1 and y_2 represent the positions of the two curves, as a function of the x-coordinate. The 3×3 dots indicate the search space $\delta_1, \delta_2 \in \{-1, 0, 1\}$.

$$p(x,d) = \begin{cases} 1 - \tanh\left(\frac{c \cdot d}{\beta_1}\right) & d \in [0, \beta_1] \\ 0 & d \in (\beta_1, \beta_2) \\ 1 - \tanh\left(\frac{c \cdot (\beta_3(x) - d)}{\beta_3(x) - \beta_2(x)}\right) & d \in [\beta_2, \beta_3] \\ 1 & d \in [\beta_3, +\infty] \end{cases} \tag{6.2}$$

where $\beta_1 = 0.3\,mm$ (minimum expected IMT); $\beta_2(x)$ is the maximum expected IMT at position x; $\beta_3(x) = \beta_2(x) + 3.5\,mm$; $c = e^1$(constant which supplies $\tanh(c) \simeq 1$); and

$$\beta_2(x) = 1.5\,mm + p(x) \cdot (D_{max} - D(x)) \cdot \gamma \tag{6.3}$$

where $p(x) \in \{0, 1\}$ indicates the presence of plaque at position x, D_{max} is a representative lumen diameter (80th percentile of all lumen diameters along the artery); $D(x)$ is the local lumen diameter at position x (clipped to D_{max}); and $\gamma = 1.5$ is a factor for outward growth of plaques.

The constant $\beta_1 = 0.3\,mm$ mm was chosen based on minimum IMT values presented in the literature [166, 167]. The point β_2 determines the length of the zero-penalty region, which represents the range of IMT values over which we assume no prior knowledge. Minimum β_2 was chosen $1.5\,mm$ as the maximum expected IMT for a healthy carotid based on presented values *in* the literature [165–167]. The point β_2 is shifted based on local features, indicating the presence of plaque, $p(x)$, as seen in Eqn. 6.3. As features, we consider the shape of the LI interface and the degree of lumen stenosis. We propose two configurations of the method to estimate $p(x)$, both

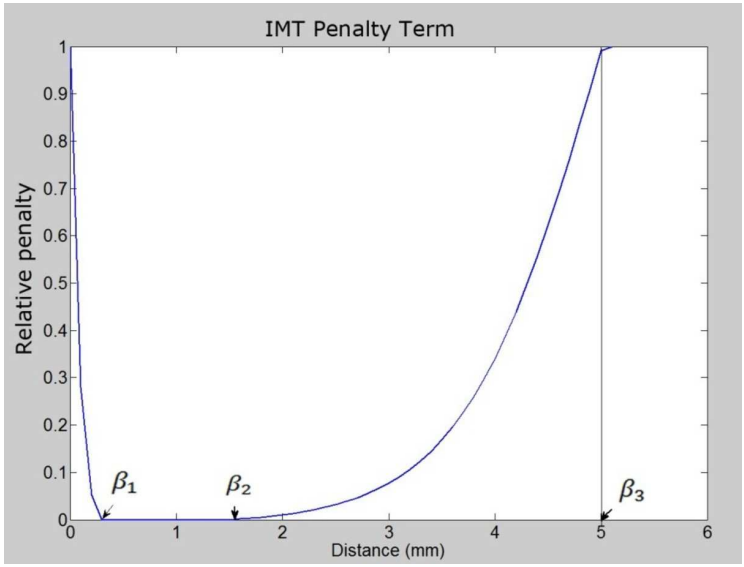

Figure 6.7: Intima–media thickness (IMT) penalty term p for healthy section of artery ($\beta_1 = 0.3\,mm$, $\beta_2 = 1.5\,mm$,$\beta_3 = 5\,mm$).

of which are evaluated in the experiments. Configuration 1 uses only the shape of the LI interface. Configuration 2 uses both the shape of the LI interface and the degree of stenosis. These configurations will be explained in detail in the next subsections. In case $p(x) = 1$, point β_2 is shifted by an amount based on the estimated degree of stenosis $(D_{max} - D(x))$, multiplied by a factor $\gamma = 1.5$ to accommodate 50% outward growth of the plaque. After β_2, we apply an exponentially increasing penalty reaching its maximum at β_3, reflecting the prior knowledge that IMT values this high are less likely.
The reason for choosing β_3 as $3.5\,mm$ further than β_2 was to provide a safety margin to avoid any hard penalty in the case of misidentification. The reason for choosing D_{max} as the 80th percentile of the lumen diameter distribution was to avoid misidentification of the presence of plaque for vessels that do not have a uniform lumen diameter distribution along the vessel (e.g., those that have the carotid bulb and one branch of bifurcation in the image plane). We chose the value of γ based on the maximum plaque development outward from the lumen (50%) observed in our data.

6.2.3.4 Configuration 1

For a healthy carotid artery, the LI interface is expected to be sufficiently smooth to be represented reasonably well by a third-order polynomial fit. Plaque regions, on the other hand, are represented by an "inward bump" of the LI interface. To detect these bumps, we fit a third-order polynomial curve to the LI interface. After the first fit, we discard the contour points at the lumen side of the fit and fit another third-order polynomial curve to the remaining points. This is repeated three times to converge

	Configuration 1 Inter-curve smoothness (α_2)						Configuration 2 Inter-curve smoothness (α_2)					
Intra-curve smoothness (α_1)	0.00	0.05	0.10	0.15	0.20	0.25	0.00	0.05	0.10	0.15	0.20	0.25
Upper												
0	583	502	505	502	502	500	737	734	737	729	733	731
0.05	435	446	435	439	437	440	655	640	649	623	621	622
0.10	482	480	486	478	479	465	549	487	485	488	462	452
0.15	520	522	521	508	483	480	504	502	499	467	471	474
0.20	554	550	541	538	513	515	534	530	517	499	496	499
0.25	566	576	577	575	555	554	549	563	558	535	531	532
Lower												
0	542	537	538	541	540	539	546	542	544	549	546	544
0.05	457	453	447	451	448	450	457	452	446	451	447	449
0.10	460	455	458	458	458	458	456	454	456	459	456	456
0.15	388	393	395	413	413	414	390	395	397	397	416	417
0.20	395	395	401	400	400	402	398	399	400	402	404	405
0.25	404	411	416	421	421	423	407	415	421	421	424	427

Table 6.1: Average root-mean-square errors (μm) for media–adventitia interface segmentation for a range of intra-curve (α_1) smoothness and inter-curve (α_2) smoothness values

	Weighting factor α_3				
	0.25	0.5	1.0	2.0	4.0
Upper	627	604	435	446	473
Lower	440	385	388	392	450
Mean	534	495	411	419	462

Table 6.2: Average root-mean-square errors (μm) between automated segmentation and ground truth for given factors (α_3) of the intima–media thickness penalty curve, using the cost function of configuration 1.

		Include shadow		Exclude Shadow	
	RMSE	Upper	Lower	Upper	Lower
Training data set					
Configuration 1	A vs. G	435 ± 174	388 ± 274	372 ± 116	354 ± 259
Configuration 2	A vs. G	452 ± 145	390 ± 276	399 ± 091	356 ± 262
Inter-observer variability	Z vs. D	242 ± 123	253 ± 192	219 ± 112	174 ± 027
Test data set					
Configuration 1	A vs. G	396 ± 202	390 ± 276	371 ± 181	427 ± 189
Configuration 2	A vs. G	446 ± 215	430 ± 192	429 ± 215	427 ± 190
Inter-observer variability	Z vs. D	210 ± 105	258 ± 163	204 ± 103	242 ± 154

Table 6.3: Average root-mean-square errors (μm) between automated segmentation and ground truth for media–adventitia interface in the training and test data sets. A = automated segmentation; G = ground truth; D = observer D.D.B.C; Z = observer Z.A.; RMSE = Root mean square error.

to an estimate of what the "healthy" LI interface would look like. On the basis of the Mannheim consensus [165] for plaque, if the distance between the fit and the actual LI interface is larger than $0.5\,mm$ for an image column x, that position is considered as a possible plaque region ($p(x) = 1$). The remaining positions are considered healthy sections of the artery ($p(x) = 0$).

6.2.3.5 Configuration 2

In this configuration, we include lumen stenosis as a second feature to detect the presence of plaques, next to the detection of inward bumps as in configuration 1. Regions with lumen diameter $D(x) < (D_{max} - 0.5\,mm)$ are considered as a sign of the presence of plaque, again based on the Mannheim consensus [165]. The plaque indicator variable $p(x)$ is computed by a logical OR operation on the assessments based on inward bump detection and lumen stenosis estimation.

	Include shadow		Exclude Shadow	
	Upper	Lower	Upper	Lower
MA interface				
A vs. G	386 ± 208	606 ± 233	378 ± 211	437 ± 162
Z vs. D*	250 ± 164	233 ± 129	227 ± 148	211 ± 109
LI interface				
A vs. G	369 ± 315	613 ± 385	337 ± 331	338 ± 079
Z vs. D*	445 ± 342	187 ± 106	256 ± 160	149 ± 073

Table 6.4: Average root-mean-square errors (μm) between automated segmentation and ground truth for MA and LI interfaces of bifurcation region (n = 7 bifurcated arteries). MA = media adventitia; LI = lumen–intima; A = automated seg- mentation; G = ground truth; D = observer D.D.B.C; Z = observer Z.A. * Inter-observer variability.

6.3 Data and Experiments

6.3.1 Data acquisition

Simultaneous, side-by-side CEUS and BMUS images were acquired at $20-Hz frame rate using a Philips iU22 system (Philips Medical Systems, Bothell, WA, USA) with an L9-3 linear probe. The standard carotid ultrasound examination and the BMUS/CEUS examination of the carotid arteries were performed. A standardized image acquisition protocol was followed based on the American Society of Echocardiography consensus statement (Stein et al. 2008). CEUS clips were recorded with the dual display mode for simultaneous B-mode ultrasound and CEUS. CEUS was performed using intravenous administration of a 0.5-mL bolus of SonoVue ultrasound contrast agent (Bracco, Milan, Italy). For the CEUS examination, power modulation imaging and a mechanical index of 0.06–0.08 were used. For each 0.5-mL SonoVue bolus injection, we recorded a 20-s image sequence. Both carotid arteries were examined, focusing on the presence of plaques. If plaques were present, the largest plaque area was identified visually in the longitudinal axis of the carotid artery and recorded.

6.3.2 Patient population and study protocol

The study population consisted of 23 symptomatic patients with carotid atherosclerotic disease who had had a stroke, transient ischemic attack or ischemic ocular event and 7 asymptomatic patients who had at least one risk factor (e.g., hypertension, hypercholesterolemia or diabetes) that can cause stroke. Symptomatic patients had moderate to severe carotid stenosis ($\geq 70\%$) as identified by radiologists on computed tomography angiography or carotid duplex ultrasonography. Asymptomatic patients had mild to moderate stenosis ($<70\%$) based on carotid duplex ultrasonography. We included in total 55 carotid arteries in our study: 46 carotid arteries from 23 symptomatic patients and 9 carotid arteries from 7 asymptomatic patients. Seven carotid arteries (all from the symptomatic patients) were excluded because of poor image

	Include shadow		Exclude Shadow	
	Upper	Lower	Upper	Lower
Training data set				
A vs. G	338 ± 187	386 ± 197	280 ± 126	338 ± 187
Z vs. D*	275 ± 114	239 ± 115	249 ± 105	338 ± 188
Test data set				
A vs. G	327 ± 182	449 ± 218	298 ± 155	469 ± 255
Z vs. D*	250 ± 187	266 ± 119	239 ± 179	247 ± 097

Table 6.5: Average root-mean-square errors (μm) between automated segmentation and ground truth for lumen–intima interface in the training and test data sets. A = automated seg- mentation; G = ground truth; D = observer D.D.B.C; Z = observer Z.A. * Inter-observer variability.

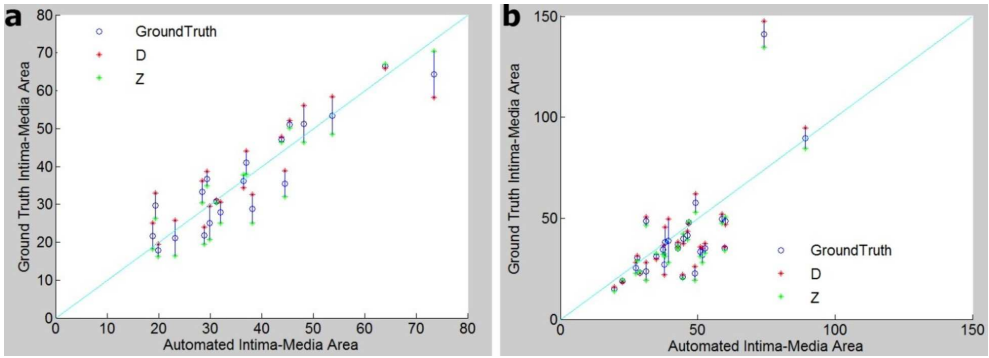

Figure 6.8: Comparison of automated intima–media area with ground truth intima media area (blue circles) for the training data set (a) and test data set (b). Intima–media areas for the different observers are indicated by the red (D.D.B.C.) and green (Z.A.) asterisks.

quality or acoustic shadowing over >50% of image width. Image quality for the whole data set was assessed in advance with the consensus of two observers. For the training set, we included the 9 carotid arteries from the 7 asymptomatic patients that were already used in our previous study [164] for lumen–intima segmentation. We added an additional 11 carotid arteries to the training set that were randomly selected from the 39 carotid arteries from symptomatic patients. The remaining 28 carotid arteries from symptomatic patients were used as the test set to evaluate performance of our segmentation method. Because the study was aimed at the CCA, we had a total of only 7 bifurcated arteries (3 in training data set, 4 in test data set) in the entire data set. The study protocol was approved by the ethics committee at Erasmus MC, University Medical Center, and all study participants provided informed consent.

6.3.3 Evaluation

The performance of automated vessel detection (see Methods) was evaluated on the training and test data sets by comparison with the consensus visual score of two observers (D.D.B.C., Z.A.).
Validation of LI and MA interfaces was achieved by comparing the automated segmentation result with a manual reference standard. The reference standard (ground truth) was obtained as the average of manual annotations of two independent observers (D.D.B.C., Z.A.). Root mean square error (RMSE) was calculated between the automated results and the ground truth in training and test data sets including and excluding shadow regions. First, we evaluated the weights of intra-curve smoothness (α_1) and inter-curve smoothness (α_2) for a range of values ($\alpha_1, \alpha_2 \in \{0, 0.05, 0.1, 0.15, 0.2, 0.25\}$ on the training set by comparison with ground truth. The optimum values of α_1 and α_2 were obtained separately for upper and lower contours. Next, the weighting factor for the IMT penalty term was evaluated for a range of values $\alpha_3 \in \{0.25, 0.5, 1, 2, 4\}$. These evaluations were done for both configurations 1 and 2. After that, the method with optimum values of α_1 , α_2 and α_3 and optimum configuration was evaluated on the test set. In all experiments, cases that had a $RMSE > 1\,mm$ were considered as failures and excluded when computing the mean RMSE over patients.
The area between the automatically detected LI and MA interfaces, the automated IM area A, was compared with the ground truth IM area G, obtained from the manual reference standard, in the training and test data sets. The Dice index $DI = 2 * (A \cap G)/(|A| + |G|))$ was calculated to measure the overlap between A and G.
The results were statistically analyzed using SPSS PASW software for Windows (Version 17.0.2, SPSS, Chicago, IL, USA). To test the association between automated segmentation results and the manual reference standard, the Pearson correlation (r) was used.

6.4 Results

The success rate of automated vessel detection was 96% (46 of 48 cases) compared with the consensus score of two observers. Automated detection failed in two cases in which the jugular vein was only partially present above the carotid artery.
Table 6.1 summarizes the results of the evaluation of intra-curve (α_1) and inter-curve (α_2) smoothness in the training data set, for both configurations 1 and 2. As seen in Table 6.1, the intra-curve smoothness has more influence on the results than the inter-curve smoothness, and the average RMSE is optimal without inter-curve smoothness for the lower wall. Table 6.2 summarizes the results for evaluation of the weighting factor α_3 for the IMT penalty term. On average, α_3 = 1 is the best setting for the IMT penalty term. No substantial difference between configurations 1 and 2 is observed.
In the training data set, there was one failure (RMSE>1 mm) for the lower MA interface of an artery and no failures for the LI interface. In the test data set, there were four lower and three upper MA interface failures for configuration 1, three upper and three lower MA interface failures for configuration 2 and one failure for LI interface. The best settings of α_1 and α_2 given in Table 6.1 for each configuration

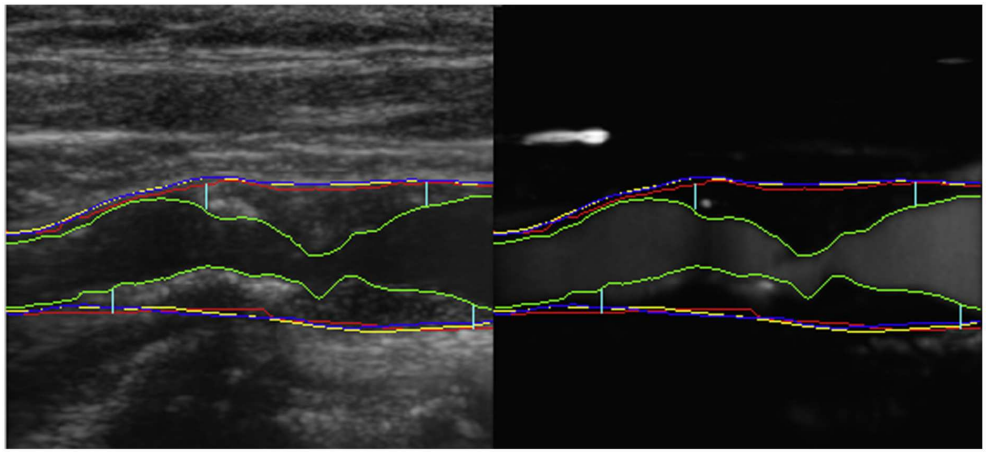

Figure 6.9: Automated segmentation of media–adventitia (red line) and lumen–intima (green line) interfaces in the BMUS (left) and CEUS (right) epitome images. Manual segmentation of the media–adventitia interface by two observers is indicated in blue (D) and yellow (Z). The left and right borders of the plaques are represented by the light blue vertical lines based on Mannheim consensus (intima–media thickness >1.5 mm). BMUS=B-mode ultrasound; CEUS=contrast- enhanced ultrasound; observer = D.D.B.C.; observer Z = Z.A.

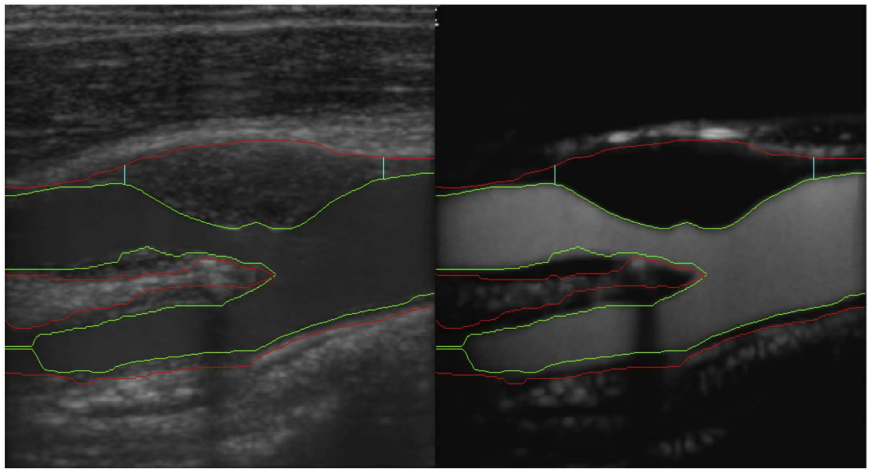

Figure 6.10: Automated segmentation of media–adventitia (red line) and lumen–intima (green line) interfaces for a bifurcated artery in BMUS (left) and CEUS (right) epitome images. Light blue vertical lines represent the left and right borders of plaque based on Mannheim consensus (intima–media thickness >1.5 mm). BMUS = B-mode ultrasound; CEUS = contrast-enhanced ultrasound.

and $\alpha_3 = 1$ was used for the RMSE calculations of MA interface in Tables 6.3 and 6.4. The average RMSE between automated segmentation results and the ground truth and the inter-observer variability are outlined in Table 6.3 for the MA interface of upper and lower contours in the training and test data sets. As it is difficult to obtain the ground truth for shadowed regions, Table 6.3 also summarizes the results when excluding shadowed regions. The average RMSEs between automated segmentation and the ground truth over patients in the training and test data sets for the MA interface were 411 ± 224 and $393 \pm 239\,\mu m$, respectively. The average RMSEs between automated segmentation and the ground truth over patients in the training and test data sets for the LI interface were 362 ± 192 and $388 \pm 200\,\mu m$, respectively. Table 6.5 lists the average RMSEs between automated results and the ground truth for the LI interface in the training and test data sets. In general, the average RMSE between automated MA and LI interface segmentation and manual ground truth is almost double the inter-observer variability apart from the results for the upper LI interface (see Tables 6.3 and 6.5). Table 6.4 summarizes the results for the MA interface using configuration 1 with the best settings and LI interface of the bifurcation region. The RMSEs of segmentation results of the LI and MA interfaces for the lower wall of the bifurcation region, including shadow regions, are almost three times larger than the inter-observer variability.

Figure 6.8 illustrates the comparison of the automated IM area with ground truth IM area in the training and test data sets. In the training data set, automated IM area was found to be significantly correlated with manual ground truth IM area for upper ($r = 0.92, p < 0.01$) and lower ($r = 0.74, p < 0.01$) wall. In the test data set, automated IM area was found to be significantly correlated with manual ground truth for upper ($r = 0.73, p < 0.01$) and lower ($r = 0.71, p < 0.01$) wall. For IM area overlap between automated and ground truth, the average DI was 68% for upper wall and 70% for lower wall in the training data set, and 71% for upper wall and 68% for lower wall in the test data set.

An example of MA and LI segmentation is illustrated in Figure 6.9 for a single-branch artery and in Figure 6.10 for a bifurcated artery.

6.5 Discussion

We have presented a method for carotid plaque segmentation in simultaneously acquired BMUS and CEUS image sequences. The method is fully automatic and robust to noise, artifacts and echo-lucent plaques. In the literature, segmentation of arterial layers in carotid arteries without plaques in BMUS is well established. However, the accurate segmentation of arterial layers in carotid arteries with plaques present poses many additional challenges. Therefore, IMT segmentation techniques are not applicable to carotid arteries with plaques. In the case of echo-lucent plaques, which present the same intensity values as the lumen, it is impossible to make a clear delineation. These limitations were discussed in the work of Loizou et al. [148].

The combination of BMUS and CEUS allows the detection of artifacts and the segmentation of echolucent plaques. CEUS provides a clear definition of the arterial lumen. Despite the advantages brought by the combination of these modalities, the

BMUS in simultaneous BMUS and CEUS possesses a lower SNR compared with standard BMUS. This occurs because a lower transmit signal power is used to avoid the disruption of the contrast agents in CEUS. To handle this issue, we employ non-rigid motion estimation and compensation to obtain an epitome image with improved SNR. As stated before, the methods of Hoogi et al. [155] and Zhang et al. [157, 158] estimated adventitia wall position in CEUS based on the estimated original lumen position, and thus, outward growth of plaques with respect to the lumen was ignored. This might lead to overor underestimation of plaque region and affect further IPN assessment. In our method, we overcome this difficulty by segmenting the media–adventitia interface from the BMUS image. Another advantage of our method compared with other studies [121, 149, 158] is that it does not require any user interaction. Furthermore, our method allows automatic multiplebranch carotid detection, whereas previous studies [111, 156, 162] were limited to one-branch (CCA) detection. Our automatic vessel detection failed in only 2 of 48 cases because of shadowing and partial appearance of the jugular vein on top of the carotid artery. These two vessels were detected as a bifurcated artery, because the geometry was very close to that. As seen in Tables 6.1, 6.3 and 6.5, the results for configurations 1 and 2 are quite similar in both our training and test data sets. That means that including the lumen stenosis to define the presence of plaque (configuration 2) does not result in noticeable improvement. As seen in Table 6.1, inter-curve smoothness does not have as much influence on the results as intracurve smoothness. For evaluation of the weighting of the IMT penalty term, the weight $\alpha_3 = 1$ is found to be optimal in the center of the given range of α_3 values, as seen in Table 6.2. The average RMSE increases with an increase or decrease in the value of α_3. The errors for MA interface detection in the training and test data sets are of the same order, about $400\,\mu m$ (~ 4 pixels), and are almost double the inter-observer variability (see Table 6.3). This might be partly explained by a systematic error between automated and manual segmentation, as seen in Figure 6.7. The automated method and manual observers seem to choose slightly different layers. The exclusion of shadow regions does not improve the results. The errors for the LI interface in the training and test data sets are of the same order and similar to the inter-observer variability after exclusion of shadow regions (see Table 6.5). As seen in Table 6.4, the segmentation results of MA and LI after exclusion of shadow regions in the bifurcation region are comparable to the segmentation results of MA and LI for the near and far wall of the CCA in Tables 6.3 and 6.5. The average RMSEs of MA and LI for the lower wall (far wall), including shadow regions, are almost three times higher than the inter-observer variability. This is because of the shadow regions, especially in the beginning and the end of bifurcation regions, which introduce larger errors as there is no wall information in those regions.

As seen in Figure 6.8(a, b), comparison of automated IM area with manual ground truth IM area is scattered around the identity line ($y = x$) for the training and test data sets apart from a few outliers in the test data set. We found a significant correlation between automated IM area and manual ground truth IM area ($p < 0.01$). Overall, our fully automated method produces results that are close to those of human operators. that are close to those of human operators. We found the DI for area overlap similar to that in the study of Loizou et al. [148] for four snake methods ($DI \in \{67.6\%$ and the study of Destrempes et al. [121] ($DI = 74.6\%$). Compared with plaque segmentation

in CEUS, the accuracy of our method is on the same order as the method of Zhang et al. [157], who reported a mean distance error of $0.40 \pm 0.08\, mm$ for plaque segmentation in CEUS. These results indicate that our fully automated method provides results at least as good as those of previous semiautomatic techniques. Our method was evaluated in the training and test data sets separately. In all the data sets, the accuracy is almost of the same order, testifying to the method's generalizability. One should keep in mind that the used image data and ground truth in these studies can be very different, so a detailed comparison of results is not possible. Because our method is fully automated and reaches results very similar to those of earlier methods, we consider our method successful and accurate.
As a limitation, the BMUS image obtained in simultaneous BMUS and CEUS has low SNR as lower signal power is used to avoid the disruption of the contrast agents in CEUS. To improve the SNR, we obtained the BMUS epitome image by performing temporal averaging. However, this might not be enough for some image sequences because of extensive noise and lack of tissue signal. Improvement of BMUS image quality in simultaneous acquisition would enhance the performance of our method. For example, using plane wave ultrasound imaging instead of a conventional linear line scan could provide an improved-SNR BMUS.
Our method is currently implemented for off-line post-processing. Segmentation of the LI and MA interfaces in the epitome image takes about a minute. Transforming the detected interfaces from the epitome image to all time frames takes several minutes. These computation times were based on an ordinary office computer. Most of our code was written in MATLAB and was not optimized for speed. Writing this in C++ and using a powerful computer will decrease the computation time enormously. The non-rigid motion estimation method was implemented using Elastix, which is coded in C++ and takes several minutes. The most recent development version of Elastix contains several accelerations [168] that will allow us to reduce the computation time even further.

6.6 Conclusion

Our method performs accurate and fully automatic plaque segmentation with multi-branch vessel detection. Using simultaneous BMUS and CEUS provides clear advantages in segmentation of carotid plaques rather than the sole use of BMUS or CEUS. The use of the combined imaging modalities allows the suppression of noise, detection and suppression of artifacts, wall information for plaque segmentation in CEUS images and detection of echo-lucent plaques in BMUS images. This plaque segmentation method is a crucial step for objective and automatic assessment of plaque composition such as IPN quantification. As far as we know, this is the first study exploiting combined information from BMUS and CEUS to automatically segment carotid plaques.

Acknowledgments

We thank G. L. ten Kate for performing the patient scans.

7 Summary and Discussion

This thesis presented techniques to align images of the carotid artery using nonrigid registration. In Part I, image registration was performed on Ultrasound (US) and Magnetic Resonance Imaging (MRI) data, and in Part II on temporal series of B-mode US (BMUS) and Contrast Enhanced US (CEUS). This chapter contains a summary of contributions introduced in this work and points out the possible clinical applications. Subsequently, I discuss open issues and challenges for future work. Finally, a general conclusion is provided.

7.1 Summary of Contributions

In both parts of this thesis, registration is used as a tool to spatially align anatomical characteristics of the carotid artery. Although the common objective is to improve the knowledge concerning the carotid anatomy and composition of atherosclerotic plaques, each part has its specific objectives.

7.1.1 US-MRI Registration of Carotid Artery

Part I (**Chapters 2-4**) covers the registration of volumetric US and MRI data. The images produced by these modalities differ in many aspect, such as intensity characteristics, image resolution, and anatomical position of the patient's neck during scanning which causes differences in carotid artery shape in the images. Furthermore, whereas the MRI data is intrinsically volumetric, the US volume is built from a series of transversal 2D slices. In the experiments of **Chapter 3** it is possible to see that only using image intensities does not lead to accurate registrations. The registration demands descriptive features, details that can be compared and associated, as accurate registrations could not be achieved by direct intensity comparison and sampling techniques.
The necessity of extracting a geometrical feature of the carotid artery was the motivation for **Chapter 2,** where an algorithm based on robust ellipse fitting to track the carotid centerline in transversal US images was introduced. The algorithm requires three manually selected seed points as input, placed in the internal carotid artery

(ICA), external carotid artery (ECA), and common carotid artery (CCA), respectively. The assumption of the algorithm is that a cross-sectional plane of the carotid artery has approximately an elliptical shape. A major difficulty in detecting centerlines is that the arterial wall can be misrepresented in the images. This represents a challenge when identifying the carotid boundaries. In order to overcome this problem, intensities that have a high likelihood to be part of the arterial wall were identified with a ray casting algorithm. From a seed point located in the arterial lumen, a set of rays were traced up to a pixel containing an intensity similar to the arterial wall. In scenarios where the wall was not visible in the image, the ray can reach another structure outside the vessel or the image limits. Subsequently, the endpoints of the rays are pruned according to their distance to the seed point and the remaining rays are used to fit an ellipse. Since the areas where the artery is not visible were not used in the ellipse fitting, the resulting ellipse approximates the shape of the carotid lumen. The center of the ellipse is used as the seed point to reinitiate the algorithm in the next slice. The algorithm ends when the centerline reaches the bifurcation point from the seed points originating in each of the arterial branches. The algorithm was evaluated on 19 carotid arteries and the average error with respect to manually annotated centerlines was $0.82\,mm$. The percentage of points with an error below 2 mm was 92% on average, which confirms the robustness of the approach.

In **Chapter 3**, a technique to perform the registration of US and MRI of the carotid carotid artery was presented. The method makes use of the lumen centerlines extracted from both image modalities. For centerline extraction, three initial seed points are required, which is the only user interaction in the entire registration algorithm. The US centerline is extracted with an improved version of the algorithm presented in **Chapter 2**. In this version, the parameters that control the pruning of rays are based on image-derived statistical values instead of user-configured parameters. The MRI lumen centerlines were extracted by the algorithm of Tang et al. [88]. The centerlines are used in the initial alignment and later in an intensity-and-point based registration metric, which consists of a weighted sum of an intensity dissimilarity metric and the Euclidean distance between centerlines. First a rigid registration is derived, and next a nonrigid registration is performed. Evaluation experiments were first carried out on a training set of five volunteers and three patients (including both left and right carotids). As evaluation measures Dice overlap and mean surface distance (MSD) between manual US lumen segmentations and deformed MRI lumen segmentations were used. On the training set, we evaluated the effect of varying the weights in the metric sum and the degree of deformation of the nonrigid registration, and established their optimum values. Subsequently, with these optimum values, the registration quality was assessed on an independent test set composed of left and right carotid arteries of one volunteer and two patients, resulting in an average MSD of $0.87\,mm$. In the evaluation experiments, we also estimated the maximum achievable registration accuracy, by registering the manually annotated US lumen segmentation with the (semi-automated) MRI lumen segmentation. The results led to better registrations (MSD around $0.2\,mm$) than the intensity-and-point based approach, suggesting that more accurate registrations could be achieved. However, US manual segmentations require intensive user interaction; therefore a method to extract lumen segmentations was needed in order to obtain registrations with minimal user interaction.

Chapter 4 presented a method to perform US-MRI registration purely based on automatically extracted geometrical features. The lumen centerlines and lumen segmentations were used as geometrical features. Registration was performed using a metric composed by a weighted sum of the dissimilarity between segmentations and the distance between centerlines. In order to extract the centerlines, the same methods as mentioned in Chapter 3 were used. To obtain the MRI segmentation, the method of Arias et al. [99] was used. For US lumen segmentation, we used a recently proposed algorithm [98] based on the same principle as [99]. This US lumen segmentation algorithm was extensively evaluated in a data set composed of 28 carotids from 14 subjects (left and right carotids from 8 patients and 6 volunteers). The optimized configuration of design parameters for each subject was selected in a cross-validation analysis. The evaluation of the registration was performed in the 28 carotids, testing various weighting factors (balancing centerline and segmentation information) and degrees of nonrigid deformation. The average and standard deviation MSD over all 28 carotids were $0.78 \pm 0.34\,mm$, which was a significant improvement compared with the method that was presented in Chapter 3.
As a general conclusion of **Part I** of this thesis, the use of geometric features turned out to be crucial for achieving accurate US-MRI registration.

7.1.2 2D+t US and CEUS Registration

Part II (Chapters 5-6) addressed the nonrigid registration of temporal series of simultaneously acquired, therefore naturally registered, side-by-side B-mode US (BMUS) and Contrast Enhanced US (CEUS) 2D images. Since this registration is performed in the temporal and spatial domains it is called 2D+t registration. The images are longitudinal planes of the carotid artery and were used to inspect the lumen and the thickness of arterial layers. As previously noted in this thesis, US images are noisy in comparison to other imaging modalities. A technique to mitigate the effect of noise and intensify the contrast between arterial layers is needed to enable an automated image analysis. During the scanning, the images were acquired at a frequency around 20Hz and a motion pattern is noticeable between consecutive image frames. The origin of the motion can be attributed to the arterial pulsation, slight patient motion, or slight movement by the clinician's hand. Nonrigid registration has proven to be a suitable technique to extract this motion pattern and it was essential to enable the construction of an image with improved signal-to-noise ratio (SNR)s, which facilitated posterior image processing as described in Chapter 5 and 6. The methods presented in these chapters are fully automated and do not require user interaction.
In **Chapter 5** side-by-side BMUS and CEUS images containing a single arterial branch were processed. In order to compensate the motion pattern, a nonrigid registration was performed in the BMUS image and applied to the CEUS image. Epitome images were built by averaging the motion compensated image series, leading to BMUS and CEUS images with improved SNR. From the epitome CEUS, the lumen centerline is estimated and used in a next step to identify image shadows. After removing the shadows, the centerline is again estimated. This centerline was used as input in a stage that roughly separates pseudo-enhancement and saturation artifacts. With the centerline estimated, and shadows and artifacts identified; the joint

histogram of the BMUS and CEUS images was used in a pixel classification step. In this step the pixels are classified into background, tissue, artifacts and lumen. The lumen contours are refined with a dynamic programming algorithm, resulting in a final lumen segmentation. The segmentation results were evaluated against manual annotations of two independent observers in two datasets with the Root Mean Square Error (RMSE) as evaluation measure. The datasets contained subjects with different degrees of stenosis [141]. In a dataset containing nine carotid arteries from individuals with mild to moderate stenosis the average RMSE was $191 \pm 43\,\mu m$, while in another dataset containing ten carotids with moderate to severe stenosis the average RMSE was $351 \pm 176\,\mu m$. In a final experiment, the transformation obtained with the nonrigid registration algorithm was applied to the resulting segmentations in order to estimate the wall distensibility. Distensibility values were comparable to the literature and within the inter-observer variability range.

In **Chapter 6** nonrigid registration was applied with the same purpose as in Chapter 5, but the subsequent image analysis was extended in order to allow fully automated segmentation of the atherosclerotic plaque. Moreover, the method was extended so that it can process images of the carotid showing multiple branches. In order to segment the plaque, a dual dynamic programming method to detect the lumen–intima (LI) and media–adventitia (MA) layers was implemented. The cost of the path is defined by a function of both appearance and geometric features. The method was evaluated against manual annotations in the two layers in a training set composed of 20 carotids and a test set composed of 28 carotids. The average RMSE in the training set was $411 \pm 224\,\mu m$ for MA and $362 \pm 192\,\mu m$ for LI. In the test set the average RMSE was $393 \pm 239\,\mu m$ for MA and $388 \pm 200\,\mu m$ for LI. The results were comparable to the inter-observer variability.

In summary, **Part II** we found that nonrigid registration was essential to obtain the epitome image and allow classification and segmentation of the lumen and arterial wall layers.

7.2 Discussion

In **Part I** nonrigid registration was used to register US and MRI of the carotid artery. In this thesis we used MRI data acquired with proton-density-weighted (PDw) and T2-weighted black blood sequences. For carotid artery plaque analysis, it is common to use a multi-contrast-weighted MRI protocol [169]. In such scenarios, the US image could be registered to a single target MRI sequence, followed by registration of all other MRI sequences to it, using for example the method presented by Van 't Klooster [90]. This would allow fully multimodal, multi-contrast analysis. A similar approach could be followed for novel quantitative MRI protocols like T1 and T2 mapping [170].

We may also look beyond MRI, and consider other modalities like computed tomography (CT) angiography and positron emission tomography (PET) for imaging the carotid artery. Registration of carotid artery CT and MRI data was demonstrated in [171]. Integrated PET-MRI systems allow a simultaneous acquisition of MRI and PET [172], thus eliminating the need for registration step. In a similar way as discussed above for multiple MRI sequences, we may here as well consider using the MRI as a bridge that facilitates registration of US to CT and PET data. The fusion of the

information from all these modalities would provide an important tool for improved carotid plaque risk assessment [16, 33, 34].

The methods presented in Part I are largely automated but still demand minimal user interaction. In order to calculate each centerline, the user must select a point in each of three branches of the carotid artery in US and MRI data. The difficulty in implementing an automated method to identify the carotid branches is related to the presence of structures with a similar shape and intensity, such as the jugular vein. It would be interesting to have a robust algorithm able to identity the carotid branches, without the need of manual inputs; this would fully automate the artery analysis.

Finally, to improve the US-MRI registration, it could be worthwhile to revisit the 3D US acquisition and reconstruction procedure. In our work, we performed freehand US examinations with a 2D probe. Using an electromagnetic tracking system the position of the probe was recorded, allowing retrospective reconstruction of a 3D US volume. In practice this procedure turned out to be rather error-prone, and it may not have led to optimal US image quality. The use of a dedicated 3D US system may improve image quality and diagnostic value [173, 174], and could therefore also lead to improved registration accuracy.

In **Part II** nonrigid registration allowed the creation of epitome images with improved SNR; additionally the carotid motion pattern could be extracted. In Chapter 5, this motion pattern was used to estimated the arterial distensibility by analyzing the lumen boundary motion. A similar procedure could be performed to assess the motion of the atherosclerotic plaque, which was extracted in Chapter 6. It is known that plaque motion may be an indicator of plaque vulnerability, which motivates the development of such tool. The localization of the atherosclerotic plaque also paves the way for developing a tool to automatically quantify the vasa vasorum in CEUS images.

Finally, a natural path to extend this research is to connect the methods and tools developed in **Parts I** and **II** of this thesis: registering 2D BMUS&CEUS imaging with MRI. A promising approach to achieve this goal would be to use 3D US as a bridge. Although 3D US and the 2D BMUS have somewhat different image characteristics, they would be acquired with the patient's neck in the same anatomical position, thus simplifying registration compared to the US-MRI registration. However, the problem is highly ill-posed, since the 2D image provides no guidance in the out-of-plane direction. It is expected that for this challenging registration problem, the noisy US intensities alone may not be sufficient. Similar to Part I, robust geometrical features may prove a useful aid here as well. In parts I and II of this thesis, we already presented techniques to extract centerlines and lumen segmentations in both 3D US and 2D BMUS. These could be used as geometrical features in a 2D-3D US registration. If accomplished, such work would enable a truly multimodal analysis, showing calcifications in CT, plaque components in MRI, volumetric plaque echolucence in 3D US, arterial wall layers in BMUS&CEUS, and vasa vasorum in CEUS. Consequently, a much more detailed picture of the carotid artery would become possible, providing the clinician with a comprehensive picture of all factors that may affect plaque vulnerability.

7.3 Conclusion

Nonrigid registration allowed the correlation of 3D US and MRI, and enabled accurate motion compensation in BMUS&CEUS images. Additionally, this thesis presented algorithms to extract geometrical features from 2D and 3D carotid US imaging, like centerlines, lumen segmentations, and wall segmentations. These features can be used for image registration (Part I), but also as useful features on their own, providing information on degree of stenosis, wall thickening, and plaque location (Part II). The methods described in this work could be used in clinical studies on carotid artery atherosclerosis, and will enable detailed and comprehensive analysis of multimodal imaging data. In the end this may lead to better diagnosis and treatment of patients with atherosclerotic disease.

Samenvatting

Dit proefschrift heeft technieken gepresenteerd om beelden van de halsslagader uit te lijnen met behulp van niet-rigide registratie. In Deel I is beeldregistratie uitgevoerd op Ultrasound (US) en Magnetic Resonance Imaging (MRI) scans, en in Deel II op reeksen van B-mode US (BMUS) en Contrast Enhanced US (CEUS). Dit hoofdstuk geeft een samenvatting van de ontwikkelingen die in dit werk zijn geïntroduceerd.
In beide delen van dit proefschrift wordt registratie gebruikt om ruimtelijke anatomische kenmerken van de halsslagader uit te lijnen, met als gemeenschappelijk einddoel om de kennis over de anatomie van de halsslagader en de samenstelling van atherosclerotische plaques te vergroten. Elk deel van het proefschrift heeft echter zijn eigen specifieke doelstelling.

US-MRI Registratie van de Halsslagader

Deel I (Hoofdstukken 2-4) heeft betrekking op de registratie van volumetrische US en MRI data. De beelden die door deze modaliteiten geproduceerd worden verschillen in vele aspecten, zoals de intensiteitskarakteristieken, beeldresolutie en de anatomische houding van de nek van de patiënt tijdens het scannen, wat verschillende vormen van de halsslagader in het beeld veroorzaaktwaardoor de vorm van de halsslagader enigzins verandert. Bovendien, terwijl de MRI data intrinsiek volumetrisch is, wordt het US volume uit een serie van transversale 2D plakken opgebouwd. In de experimenten van **Hoofdstuk 3** is het mogelijk om te zien dat het gebruik van alleen beeldintensiteiten niet tot nauwkeurige registraties leidt. De registratie vereist meer informatieve kenmerken, details die kunnen worden vergeleken en geassocieerd, omdat nauwkeurige registraties niet kunnen worden bereikt door directe vergelijking van beeldintensiteiten in combinatie met standaard bemonsteringstechnieken.
De noodzaak om robuuste geometrische eigenschappen van de halsslagader te extraheren vormt de motivatie voor het werk beschreven in **Hoofdstuk 2**. In dit hoofdstuk is een algoritme geintroduceerd dat de middellijn van de halsslagader kan traceren in transversale US beelden, door op een robuuste wijze ellipsvormen te passen op de beelden. Het algoritme vereist drie handmatig geselecteerde beginpunten als input,

geplaatst in respectievelijk de interne halsslagader (ICA), de externe halsslagader (ECA), en de gemeenschappelijke halsslagader (CCA). De aanname van het algoritme is dat een doorsnede van de halsslagader bij benadering een elliptische vorm heeft. Een grote uitdaging bij het opsporen van de middellijn is, dat de slagaderwand verkeerd of onduidelijk kan worden weergegeven in de beelden. Dit maakt het lastig om de wand van de halsslagader te identificeren. Om dit probleem te overkomen werden intensiteiten die met een hoge waarschijnlijkheid behoren tot de arteriële wand gedetecteerd met een ray-casting algoritme. Vanuit een beginpunt in het arteriële lumen werden een aantal stralen getraceerd tot op een pixel met een vergelijkbare intensiteit als de slagaderwand. In scenario's waarin de wand niet zichtbaar was in het beeld, kan de straal een andere structuur bereiken buiten het vat of de grenzen van het beeld. Daarom worden vervolgens de eindpunten van de stralen afgekapt op basis van hun afstand tot het beginpunt en de overblijvende stralen worden gebruikt om een ellips te fitten. Omdat de gebieden waar de slagader niet zichtbaar is niet werden gebruikt in de ellips fitting, benadert de resulterende ellips de vorm van het lumen van de halsslagader. Het middelpunt van de ellips wordt door het algoritme gebruikt als het beginpunt om het volgende segment als het beginpunt voor de volgende transversale scan. Het algoritme eindigt als de middellijn het vertakkingspunt bereikt vanuit de beginpunten in elk van de arteriele vertakkingen. Het algoritme werd beoordeeld op 19 halsslagaders en de gemiddelde fout met betrekking tot handmatig geannoteerde middellijnen was $0.82\,mm$. Het percentage punten met een fout onder de $2\,mm$ was 92% gemiddeld, wat de robuustheid van de aanpak bevestigt.

In **Hoofdstuk 3**, werd een techniek gepresenteerd om de registratie van de US en MRI van de halsslagader uit te voeren. De methode maakt gebruik van de lumen middellijnen geëxtraheerd uit beide modaliteiten. Voor de lumen middellijn extractie zijn drie initiële beginpunten vereist, de enige gebruikersinteractie in het gehele registratie algoritme. De US middellijn wordt geëxtraheerd met een verbeterde versie van het algoritme uit Hoofdstuk 2. In deze versie zijn de parameters die het afkappen van de stralen regelen gebaseerd op in het beeld verkregen statistische waarden in plaats van door de gebruiker geconfigureerde parameters. De MRI lumen middellijn wordt geëxtraheerd door het algoritme van Tang et al. De middellijnen worden gebruikt in de initiële uitlijning en later in een intensiteit-en-punt gebaseerde registratiemaat, die bestaat uit een gewogen som van een intensiteitsverschilmetriek en een maat voor de afstand tussen de middellijnen. Eerst wordt een rigide registratie bepaald, waarna een niet-rigide registratie wordt uitgevoerd. De evaluatie experimenten werden eerst uitgevoerd op een training set van vijf vrijwilligers en drie patiënten (met inbegrip van zowel de linker als rechter halsslagader). Als evaluatiemaat metingen werden Dice overlap en gemiddelde oppervlakte afstand (MSD) tussen handmatige US lumensegmentaties en geregistreerde MRI lumensegmentaties gebruikt. Op de trainingsset evalueerden we het effect van het variëren van de gewichten in de metriek en de mate van vervorming tijdens de niet-rigide registratie en vonden hun optimale waarden. Vervolgens, met deze optimale waarden, werd de registratie kwaliteit beoordeeld op een onafhankelijke test set bestaande uit de linker en rechter halsslagader van een vrijwilliger en twee patiënten. Dit resulteerde in een gemiddelde MSD van $0.87\,mm$. We schatten ook de maximaal haalbare nauwkeurigheid van de registratie, door het registreren van de handmatig geannoteerde US lumen segmentatie met de

(semi-automatische) MRI lumen segmentatie. De resultaten leidden tot betere registraties (MSD ongeveer $0.2\,mm$) dan de intensiteit-en-punt gebaseerde benadering,was suggereert dat de automatische registratie nog verder verbeterd kon worden. Echter, handmatige segmentatie van het lumen in US beelden vereist een intensieve interactie van de gebruiker. Om dus nog nauwkeurigere registratie te behalen, met minimale interactie van de gebruiker, was het nodig om lumensegmentaties automatisch te kunnen extraheren.

Hoofdstuk 4 presenteerde een methode om US-MRI registratie uit te voeren puur gebaseerd op automatisch gevonden geometrische kenmerken. De lumen middellijnen en segmentaties werden als geometrische kenmerken gebruikt. Registratie werd uitgevoerd met een metriek die bestaat uit een gewogen som van het verschil tussen segmentaties en de afstand tussen de middellijnen. Om de middellijnen te extraheren werden dezelfde methoden gebruikt als genoemd in Hoofdstuk 3. Om de MRI segmentatie te verkrijgen, werd de methode van Arias et al gebruikt. [99]. Voor US lumen segmentatie gebruikten we een recent voorgesteld algoritme [98] gebaseerd op hetzelfde principe als [99]. Dit US lumen segmentatie-algoritme werd uitgebreid geëvalueerd op een dataset samengesteld uit 28 halsslagaders van 14 proefpersonen (linker en rechter halsslagaders van 8 patiënten en 6 vrijwilligers). De configuratie van instelbare parameters werd voor elke proefpersoon geoptimaliseerd in een kruisvalidatie analyse. De evaluatie van de registratie werd uitgevoerd in de 28 halsslagaders, door verschillende wegingsfactoren (voor de balancering van middellijn- en segmentatie-informatie) en de mate van niet-rigide vervorming te testen. Het gemiddelde en de standaarddeviatie van MSD over alle 28 halsslagaders waren $0.78 \pm 0.34\,mm$. Dit was een aanzienlijke verbetering vergeleken met de methode die werd gepresenteerd in Hoofdstuk 3.

Als algemene conclusie van Deel II van dit proefschrift blijkt het gebruik van geometrische kenmerken van cruciaal belang te zijn voor het bereiken van een accurate US-MRI-registratie.

2D+t US en CEUS Registratie

Deel II (Hoofdstukken 5-6) gaat in op de niet-rigide registratie van een reeks gelijktijdig opgenomen, en dus per definitie geregistreerde, zij-aan-zij B-mode US (BMUS) en Contrast Enhanced US (CEUS) 2D-beelden. Omdat deze registratie als het ware in het tijd- en ruimte-domein wordt uitgevoerd, wordt het 2D+t registratie genoemd. De afbeeldingen zijn longitudinale doorsnedes van de halsslagader en worden gebruikt om de vorm van het lumen en de dikte van de arteriële lagen te inspecteren. Zoals eerder opgemerkt in dit proefschrift, bevatten US beelden veel ruis in vergelijking met andere beeldvormende modaliteiten. Om geautomatiseerde beeldanalyse mogelijk te maken, is een techniek om de ruis te verminderen en het contrast te intensiveren tussen arteriële lagen nodig. Tijdens het scannen werden de beelden opgenomen met een frequentie rond 20 Hz en een bewegingspatroon is merkbaar tussen de opeenvolgende beelden. De oorzaak van deze beweging kan worden toegeschreven aan de arteriële pulsaties, lichte beweging van de patiënt, of een lichte beweging van de hand van de arts. Niet-rigide registratie heeft bewezen een geschikte techniek te zijn om dit bewegingspatroon te extraheren en het was noodzakelijk voor de constructie van een beeld met verbeterde signaal-ruisverhouding (SNR), die latere beeldverwerking vergemakkelijkt zoals beschreven in Hoofdstuk 5 en 6. De methoden in deze hoofdstukken zijn volledig geautomatiseerd en interactie van de gebruiker is niet nodig.

In **Hoofdstuk 5** werden zij-aan-zij BMUS en CEUS afbeeldingen met een slagaderlijke tak verwerkt. Om het bewegingspatroon te compenseren, werd een niet-rigide registratie uitgevoerd in het BMUS beeld en toegepast op het CEUS beeld. Epitoombeelden werden gemaakt door het middelen van de voor beweging gecompenseerde beelden, wat leidt tot BMUS en CEUS beelden met verbeterde SNR.Op basis van het CEUS epitoom wordt de lumen middellijn bepaald, en deze wordt vervolgens gebruikt om schaduwgebieden in het beeld te identificeren. Na het verwijderen van de schaduwen wordt de middellijn opnieuw geschat. Deze middellijn wordt gebruikt als input in een fase die ruwweg de pseudo-enhancement van de verzadigingsartefacten scheidt. Met de middellijn geschat, en schaduwen en artefacten geïdentificeerd, wordt een gecombineerd histogram van de BMUS en CEUS beelden gebruikt in een pixelclassificatiestap. In deze stap worden de pixels ingedeeld in achtergrond, weefsel, artefacten en lumen. De lumencontouren worden verfijnd met behulp van een dynamisch-programmeren methode, wat resulteert in een uiteindelijke lumensegmentatie. De segmentatieresultaten werden getoetst via handmatige annotaties van twee onafhankelijke waarnemers in twee datasets met de Root Mean Square Error (RMSE) als evaluatiemethode. De datasets bevatten proefpersonen met verschillende stenosegraderingen [141]. In een dataset met daarin negen halsslagaders van individuen met een milde tot matige stenose was de gemiddelde RMSE $191 \pm 43\,\mu m$, terwijl in een andere dataset met tien halsslagaders met matige tot ernstige stenose de gemiddelde RMSE $351 \pm 176\,\mu m$ was. Als laatste experiment werd de omzetting verkregen met de niet-rigide registratie toegepast op de resulterende segmentatie voor de schatting van de wand distensibiliteit. Distensibiliteitswaarden waren vergelijkbaar met de literatuur en vielen binnen het bereik van de variabiliteit tussen waarnemers.

In **Hoofdstuk 6** werd niet-rigide registratie toegepast met hetzelfde doel als in Hoofdstuk 5, maar de daaropvolgende beeldanalyse werd uitgebreid om volautomatische segmentatie van de atherosclerotische plaque mogelijk te maken. Bovendien werd de methode uitgebreid, zodat deze overweg kan met beelden van de halsslagader waarin meerdere takken zichtbaar zijn.Om de plaque te segmenteren gebruikten we een duale vorm van de methode van dynamisch programmeren, waarmee de lumen-intima (LI) en media-adventitia (MA) lagen gelijktijdig getraceerd worden. De kosten van hun pad door het beeld worden gegeven door een functie van hun uiterlijke en geometrische eigenschappen. De methode werd geëvalueerd met handmatige annotaties in de twee lagen in een training set bestaande uit 20 halsslagaders en een test set bestaande uit 28 halsslagaders. De gemiddelde RMSE in de training set was $411 \pm 224\,\mu m$ voor MA en $362 \pm 192\,\mu m$ voor LI. In de test set was de gemiddelde RMSE $393 \pm 239\,\mu m$ voor MA en $388 \pm 200\,\mu m$ voor LI. De resultaten waren vergelijkbaar met de variabiliteit tussen waarnemers

Samengevat vonden we in **Deel II** dat de niet-rigide registratie essentieel was om het epitoombeeld te verkrijgen en de classificatie en segmentatie van het lumen en de slagaderwand mogelijk te maken.

Conclusie

Niet-rigide registratie stelde ons in staat om 3D US en MRI beelden met elkaar te correleren, en maakte het mogelijk om nauwkeurig voor beweging te compenseren in BMUS&CEUS beeldreeksen. Daarnaast hebben we in dit proefschrift algoritmes gepresenteerd die uit 2D and 3D US scans geometrische eigenschappen van de halsslagader extraheren, zoals de middellijn en lumen- en wandsegmentaties. Deze geometrische karakteristieken kunnen gebruikt worden voor beeldregistratie (Deel I), maar zijn ook waardevol op zichzelf aangezien ze informatie geven over de stenosegraad, wandverdikking en plaque locatie (Deel II). De methodes beschreven in dit werk zouden gebruikt kunnen worden in klinische studies naar atherosclerose in de halsslagader; multimodale beeldinformatie kan er in meer detail en vollediger mee geanalyseerd worden. Uiteindelijk zou dit kunnen leiden tot een betere diagnose en behandeling van patiënten met atherosclerose.

Bibliography

[1] O. Chestnov et al. *Global status report on noncommunicable diseases 2014.* World Health Organization, 2014.

[2] J. Leal, R. Luengo-Fernández, A. Gray, S. Petersen, and M. Rayner. Economic burden of cardiovascular diseases in the enlarged european union. *European heart journal*, 27(13):1610–1619, 2006.

[3] JC LaRosa, D Hunninghake, D Bush, MH Criqui, GS Getz, AM Gotto Jr, SM Grundy, L Rakita, RM Robertson, and ML Weisfeldt. The cholesterol facts. a summary of the evidence relating dietary fats, serum cholesterol, and coronary heart disease. a joint statement by the american heart association and the national heart, lung, and blood institute. the task force on cholesterol issues, american heart association. *Circulation*, 81(5):1721, 1990.

[4] K.K. Teo, S. Ounpuu, S. Hawken, M.R. Pandey, V. Valentin, D. Hunt, R. Diaz, W. Rashed, R. Freeman, L. Jiang, et al. Tobacco use and risk of myocardial infarction in 52 countries in the interheart study: a case-control study. *The Lancet*, 368(9536):647–658, 2006.

[5] N.R. Cook, J.A. Cutler, E. Obarzanek, J.E. Buring, K.M. Rexrode, S.K. Kumanyika, L.J. Appel, and P.K. Whelton. Long term effects of dietary sodium reduction on cardiovascular disease outcomes: observational follow-up of the trials of hypertension prevention (TOHP). *BMJ*, 334(7599):885, 2007.

[6] V. Fuster, B. Stein, J.A. Ambrose, L. Badimon, J.J. Badimon, and J.H. Chesebro. Atherosclerotic plaque rupture and thrombosis. evolving concepts. *Circulation*, 82(3 Suppl):II47–59, 1990.

[7] Willem E. Hellings, Wouter Peeters, Frans L. Moll, Sebastiaan R. Piers, Jessica van Setten, Peter J. Van der Spek, Jean-Paul P. de Vries, Kees A. Seldenrijk,

Peter C. De Bruin, Aryan Vink, Evelyn Velema, Dominique P. de Kleijn, and Gerard Pasterkamp. Composition of carotid atherosclerotic plaque is associated with cardiovascular outcome: a prognostic study. *Circulation*, 121(17):1941–1950, 2010.

[8] P.R. Moreno, K. Purushothaman, M. Sirol, A.P. Levy, and V. Fuster. Neovascularization in human atherosclerosis. *Circulation*, 113(18):2245–2252, 2006.

[9] Scandinavian Simvastatin Survival Study Group et al. Randomised trial of cholesterol lowering in 4444 patients with coronary heart disease: the scandinavian simvastatin survival study (4s). *The Lancet*, 344(8934):1383–1389, 1994.

[10] Epidemiological Studies Unit. Efficacy and safety of cholesterol-lowering treatment: prospective meta-analysis of data from 90 056 participants in 14 randomised trials of statins. *Lancet*, 366(9493):1267–1278, 2005.

[11] A. Poli, E. Tremoli, A. Colombo, M. Sirtori, P. Pignoli, and R. Paoletti. Ultrasonographic measurement of the common carotid artery wall thickness in hypercholesterolemic patients a new model for the quantitation and follow-up of preclinical atherosclerosis in living human subjects. *Atherosclerosis*, 70(3):253–261, 1988.

[12] R. Salonen and J.T. Salonen. Progression of carotid atherosclerosis and its determinants: a population-based ultrasonography study. *Atherosclerosis*, 81(1):33–40, 1990.

[13] H.J.M. Barnett, H.E. Meldrum, and M. Eliasziw. The appropriate use of carotid endarterectomy. *Canadian Medical Association Journal*, 166(9):1169–1179, 2002.

[14] Mayberg M.R., Wilson S., Yatsu F., and et al. Carotid endarterectomy and prevention of cerebral ischemia in symptomatic carotid stenosis. *JAMA*, 266(23):3289–3294, 1991.

[15] S.A.M. Nashef, F. Roques, P. Michel, E. Gauducheau, S. Lemeshow, R. Salamon, EuroSCORE Study Group, et al. European system for cardiac operative risk evaluation (euroscore). *European Journal of Cardio-Thoracic Surgery*, 16(1):9–13, 1999.

[16] R.M. Kwee, R.J. Van Oostenbrugge, L. Hofstra, G.J. Teule, J.M.A. van Engelshoven, W.H. Mess, and M.E. Kooi. Identifying vulnerable carotid plaques by noninvasive imaging. *Neurology*, 70(24 Part 2):2401–2409, 2008.

[17] D. Vancraeynest, A. Pasquet, V. Roelants, B.L. Gerber, and J.J. Vanoverschelde. Imaging the vulnerable plaque. *Journal of the American College of Cardiology*, 57(20):1961–1979, 2011.

[18] R. L Wilensky, H.K. Song, and V.A. Ferrari. Role of magnetic resonance and intravascular magnetic resonance in the detection of vulnerable plaques. *Journal of the American College of Cardiology*, 47(8s1):C48–C56, 2006.

[19] C. Yuan, K. W Beach, L. H. Smith, and T.S. Hatsukami. Measurement of atherosclerotic carotid plaque size in vivo using high resolution magnetic resonance imaging. *Circulation*, 98(24):2666–2671, 1998.

[20] G.M. LaMuraglia, J.F. Southern, V. Fuster, H.L. Kantor, et al. Magnetic resonance images lipid, fibrous, calcified, hemorrhagic, and thrombotic components of human atherosclerosis in vivo. *Circulation*, 94(5):932–938, 1996.

[21] I. Wendelhag, T. Gustavsson, M. Suurküla, G. Berglund, and J. Wikstrand. Ultrasound measurement of wall thickness in the carotid artery: fundamental principles and description of a computerized analysing system. *Clinical physiology*, 11(6):565–577, 1991.

[22] P. Prati, A. Tosetto, M. Casaroli, A. Bignamini, L. Canciani, N. Bornstein, G. Prati, and P.J. Touboul. Carotid plaque morphology improves stroke risk prediction: usefulness of a new ultrasonographic score. *Cerebrovascular diseases*, 31(3):300–304, 2011.

[23] Aaron Fenster, Donal B Downey, and H Neale Cardinal. Three-dimensional ultrasound imaging. *Physics in medicine and biology*, 46(5):R67, 2001.

[24] S.E. Salcudean, G.S. Bell, P.D. Lawrence, A. Marko, and M. Jameson. Robotically assisted medical ultrasound, July 30 2002. US Patent 6,425,865.

[25] A. Gee, R. Prager, G. Treece, C. Cash, and L. Berman. Processing and visualizing three-dimensional ultrasound data. *Br J Radiol*, 77(suppl_2):S186–193, 2004.

[26] O.V. Solberg, F. Lindseth, H. Torp, R.E. Blake, and T.A.N. Hernes. Freehand 3d ultrasound reconstruction algorithms-a review. *Ultrasound in medicine & biology*, 33(7):991–1009, 2007.

[27] A. Fenster, A. Landry, D.B. Downey, R.A. Hegele, and J.D. Spence. 3d ultrasound imaging of the carotid arteries. *Current Drug Targets-Cardiovascular & Hematological Disorders*, 4(2):161–175, 2004.

[28] P. Pignoli, E. Tremoli, A. Poli, P. Oreste, and R. Paoletti. Intimal plus medial thickness of the arterial wall: a direct measurement with ultrasound imaging. *Circulation*, 74(6):1399–1406, 1986.

[29] A. Iannuzzi, T. Wilcosky, M. Mercuri, P. Rubba, F.A. Bryan, and M.G. Bond. Ultrasonographic correlates of carotid atherosclerosis in transient ischemic attack and stroke. *Stroke*, 26(4):614–619, 1995.

[30] S. Meairs and M. Hennerici. Four-dimensional ultrasonographic characterization of plaque surface motion in patients with symptomatic and asymptomatic carotid artery stenosis. *Stroke*, 30(9):1807–1813, 1999.

[31] Daniel Staub, Mita B Patel, Anjan Tibrewala, David Ludden, Mahala Johnson, Paul Espinosa, Blai Coll, Kurt A Jaeger, and Steven B Feinstein. Vasa vasorum and plaque neovascularization on contrast-enhanced carotid ultrasound imaging correlates with cardiovascular disease and past cardiovascular events. *Stroke*, 41(1):41–47, 2010.

[32] L Gerrit, Eric JG Sijbrands, Roelf Valkema, J Folkert, Steven B Feinstein, Antonius FW Van der Steen, Mat JAP Daemen, and Arend FL Schinkel. Molecular imaging of inflammation and intraplaque vasa vasorum: A step forward to identification of vulnerable plaques? *Journal of nuclear cardiology*, 17(5):897–912, 2010.

[33] J. Golledge, D.A. Siew, et al. Identifying the carotid 'high risk' plaque: is it still a riddle wrapped up in an enigma? *European Journal of Vascular and Endovascular Surgery*, 35(1):2, 2008.

[34] J.A. Chalela. Evaluating the carotid plaque: going beyond stenosis. *Cerebrovascular Diseases*, 27(Suppl. 1):19–24, 2009.

[35] C.R. Maurer and J.M. Fitzpatrick. A review of medical image registration. *Interactive image-guided neurosurgery*, 17, 1993.

[36] D.L.G. Hill, P.G. Batchelor, M. Holden, and D.J. Hawkes. Medical image registration. *Physics in medicine and biology*, 46(3):R1, 2001.

[37] J.B.A. Maintz and M.A. Viergever. A survey of medical image registration. *Medical image analysis*, 2(1):1–36, 1998.

[38] B. Zitova and J. Flusser. Image registration methods: a survey. *Image and vision computing*, 21(11):977–1000, 2003.

[39] William R Crum, Thomas Hartkens, and DLG Hill. Non-rigid image registration: theory and practice. *The British Journal of Radiology*, 2014.

[40] M. J. McCarthy, I. M. Loftus, M. M. Thompson, L. Jones, N. J. M. London, P. R. F. Bell, A. R. Naylor, and N. P. J. Brindle. Angiogenesis and the atherosclerotic carotid plaque: An association between symptomatology and plaque morphology,. *Journal of Vascular Surgery*, 30(2):261–268, 1999.

[41] Rui Rocha, Aurélio Campilho, Jorge Silva, Elsa Azevedo, and Rosa Santos. Segmentation of the carotid intima-media region in B-mode ultrasound images. *Image and Vision Computing*, 28(4), 2010.

[42] L. Antiga and D. A. Steinman. Robust and Objective Decomposition and Mapping of Bifurcating Vessels. *IEEE Transactions on Medical Imaging*, 23(6):704–713, June 2004.

[43] S. R. Aylward and E. Bullitt. Initialization, noise, singularities, and scale in height ridge traversal for tubular object centerline extraction. *IEEE Transactions on Medical Imaging*, 21(2):61–75, February 2002.

[44] S. Bouix, K. Siddiqi, and A. Tannenbaum. Flux driven automatic centerline extraction. *Medical Image Analysis*, 9(3):209–221, 2005.

[45] Thomas Pock, Reinhard Beichel, and Horst Bischof. A novel robust tube detection filter for 3D centerline extraction. In Heikki Kalviainen, Jussi Parkkinen, and Arto Kaarna, editors, *Image Analysis*, volume 3540 of *Lecture Notes in Computer Science*, chapter 49, pages 55–94. Springer Berlin / Heidelberg, Berlin, Heidelberg, 2005.

[46] Ming Wan, Zhengrong Liang, Qi Ke, Lichan Hong, I. Bitter, and A. Kaufman. Automatic centerline extraction for virtual colonoscopy. *IEEE Transactions on Medical Imaging*, 21(12):1450–1460, December 2002.

[47] M. Schaap, C.T. Metz, T. van Walsum, A.G. van der Giessen, A.C. Weustink, N.R.A. Mollet, C. Bauer, H. Bogunović, C. Castro, X. Deng, E. Dikici, T. O'Donnell, M. Frenay, O. Friman, M. Hernández Hoyos, P.H. Kitslaar, K. Krissian, C. Kühnel, M. A. Luengo-Oroz, M. Orkisz, Ö Smedby, M. Styner, A. Szymczak, H. Tek, C. Wang, S. K. Warfield, S. Zambal, Y. Zhang, G. P. Krestin, and W.J. Niessen. Standardized evaluation methodology and reference database for evaluating coronary artery centerline extraction algorithms. *Medical Image Analysis*, 13/5:701–714, 2009.

[48] K. Hameeteman, M.A. Zuluaga, M. Freiman, L. Joskowicz, O Cuisenaire, L. Florez Valencia, M.A. Gulsun, K. Krissian, J. Mille, W.C.K. Wong, M. Orkisz, H. Tek, M. Hernandez Hoyos, F. Benmansour, A.C.S. Chung, S. Rozie, M.J. van Gils, L. van den Borne, J. Sosna, P. Berman, N. Cohen, P. Douek, I. Sánchez, M. Aissat, M. Schaap, C.T. Metz, G. P. Krestin, A van der Lugt, W.J. Niessen, and T. van Walsum. Evaluation framework for carotid bifurcation lumen segmentation and stenosis grading. *Medical Image Analysis*, 2011.

[49] J Alison Noble and Djamal Boukerroui. Ultrasound image segmentation: a survey. *Medical Imaging, IEEE Transactions on*, 25(8):987–1010, 2006.

[50] P. Abolmaesumi and M. R. Sirouspour. An Interacting Multiple Model Probabilistic Data Association Filter for Cavity Boundary Extraction From Ultrasound Images. *IEEE Transactions on Medical Imaging*, 23(6):772–784, June 2004.

[51] Spyretta Golemati, John Stoitsis, Emmanouil G. Sifakis, Thomas Balkizas, and Konstantina S. Nikita. Using the Hough transform to segment ultrasound images of longitudinal and transverse sections of the carotid artery. *Ultrasound in medicine & biology*, 33(12):1918–1932, December 2007.

[52] Steven Hammer, Adam Jeays, Paul L. Allan, Rod Hose, David Barber, William J. Easson, and Peter R. Hoskins. Acquisition of 3-D arterial geometries and integration with computational fluid dynamics. *Ultrasound in medicine & biology*, 35(12):2069–2083, December 2009.

[53] D. Wang, R. Klatzky, N. Amesur, and G. Stetten. Carotid artery and jugular vein tracking and differentiation using spatiotemporal analysis. In Rasmus Larsen, Mads Nielsen, and Jon Sporring, editors, *Medical Image Computing and Computer-Assisted Intervention MICCAI 2006*, volume 4190 of *Lecture Notes in Computer Science*, chapter 80, pages 654–661. Springer Berlin / Heidelberg, Berlin, Heidelberg, 2006.

[54] D. C. Wang, R. Klatzky, B. Wu, G. Weller, A. R. Sampson, and G. D. Stetten. Fully automated common carotid artery and internal jugular vein identification and tracking using B-mode ultrasound. *IEEE transactions on bio-medical engineering*, 56(6):1691–1699, June 2009.

[55] Gary R. Bradski and Vadim Pisarevsky. Intel's Computer Vision Library: Applications in Calibration, Stereo, Segmentation, Tracking, Gesture, Face and Object Recognition. *Computer Vision and Pattern Recognition, IEEE Computer Society Conference on*, 2:2796+, 2000.

[56] M. Piccinelli, A. Veneziani, D. A. Steinman, A. Remuzzi, and L. Antiga. A Framework for Geometric Analysis of Vascular Structures: Application to Cerebral Aneurysms. *IEEE Transactions on Medical Imaging*, 28(8):1141–1155, August 2009.

[57] Sang-Wook W. Lee, Luca Antiga, J. David Spence, and David A. Steinman. Geometry of the carotid bifurcation predicts its exposure to disturbed flow. *Stroke; a journal of cerebral circulation*, 39(8):2341–2347, August 2008.

[58] E. Falk, P.K. Shah, and V. Fuster. Coronary plaque disruption. *Circulation*, 92(3):657–671, 1995.

[59] J David Spence and Robert A Hegele. Noninvasive phenotypes of atherosclerosis similar windows but different views. *Stroke*, 35(3):649–653, 2004.

[60] S. Carr, A. Farb, W.H. Pearce, R. Virmani, J.S. Yao, et al. Atherosclerotic plaque rupture in symptomatic carotid artery stenosis. *Journal of Vascular Surgery*, 23(5):755, 1996.

[61] T Saam, MS Ferguson, VL Yarnykh, N Takaya, D Xu, NL Polissar, TS Hatsukami, and C Yuan. Quantitative evaluation of carotid plaque composition by in vivo mri. *Arteriosclerosis, Thrombosis, and Vascular Biology*, 25(1):234–239, 2005.

[62] T.S. Hatsukami, R. Ross, N.L. Polissar, and C. Yuan. Visualization of fibrous cap thickness and rupture in human atherosclerotic carotid plaque in vivo with high-resolution magnetic resonance imaging. *Circulation*, 102(9):959–964, 2000.

[63] P. J. Slomka, J. Mandel, D. Downey, and A. Fenster. Evaluation of voxel-based registration of 3-D power Doppler ultrasound and 3-D magnetic resonance angiographic images of carotid arteries. *Ultrasound in Medicine & Biology*, 27(7):945–955, 2001.

[64] N. D. Nanayakkara, B. Chiu, A. Samani, J. D. Spence, J. Samarabandu, and A. Fenster. A 'twisting and bending' model-based nonrigid image registration technique for 3-D ultrasound carotid images. *IEEE Transactions on Medical Imaging*, 27(10):1378–1388, 2008.

[65] N. D. Nanayakkara, B. Chiu, A. Samani, J. D. Spence, J. Samarabandu, G. Parraga, and A. Fenster. Nonrigid registration of three-dimensional ultrasound and magnetic resonance images of the carotid arteries. *Medical Physics*, 36(2):373–385, 2009.

[66] B. Chiu, V. Shamdasani, R. Entrekin, C. Yuan, and W.S. Kerwin. Characterization of carotid plaques on 3-dimensional ultrasound imaging by registration with multicontrast magnetic resonance imaging. *Journal of Ultrasound in Medicine*, 31(10):1567–1580, 2012.

[67] P. J. Besl and N. D. McKay. A Method for Registration of 3-D Shapes. *IEEE Transactions on Pattern Analysis and Machine Intelligence*, 14:239–256, 1992.

[68] G. P. Penney, J. M. Blackall, M. S. Hamady, T. Sabharwal, A. Adam, and D. J. Hawkes. Registration of freehand 3D ultrasound and magnetic resonance liver images. *Medical Image Analysis*, 8(1):81–91, 2004.

[69] I. Reinertsen, M. Descoteaux, K. Siddiqi, and D. L. Collins. Validation of vessel-based registration for correction of brain shift. *Medical Image Analysis*, 11(4):374 – 388, 2007.

[70] Julien Jomier, Elizabeth Bullitt, Mark Van Horn, Chetna Pathak, and Stephen R Aylward. 3D/2D model-to-image registration applied to TIPS surgery. In *Medical Image Computing and Computer-Assisted Intervention–MICCAI 2006*, pages 662–669. Springer, 2006.

[71] Martin Groher, Darko Zikic, and Nassir Navab. Deformable 2d-3d registration of vascular structures in a one view scenario. *Medical Imaging, IEEE Transactions on*, 28(6):847–860, 2009.

[72] Martin Groher, Maximilian Baust, Darko Zikic, and Nassir Navab. Monocular deformable model-to-image registration of vascular structures. In *Biomedical Image Registration*, pages 37–47. Springer, 2010.

[73] D.D.B. Carvalho, S. Klein, Z. Akkus, G. ten Kate, H. Tang, M. Selwaness, A. Schinkel, J. Bosch, A. van der Lugt, and W. Niessen. Registration of freehand ultrasound and MRI of carotid arteries through combination of point-based and intensity-based algorithms. *Biomedical Image Registration*, pages 131–140, 2012.

[74] H. Tang, T. Van Walsum, R.S. Van Onkelen, S. Klein, R. Hameeteman, M. Schaap, Q.J.A. Van den Bouwhuijsen, J.C.M. Witteman, A. Van der Lugt, L.J. van Vliet, et al. Multispectral MRI centerline tracking in carotid arteries. In *SPIE Medical Imaging*, pages 79621N–79621N–7. International Society for Optics and Photonics, 2011.

[75] D.D.B. Carvalho, S. Klein, Z. Akkus, G.L. ten Kate, A.F.L. Schinkel, J.G. Bosch, A. van der Lugt, and W.J. Niessen. Estimating 3d lumen centerlines of carotid arteries in free-hand acquisition ultrasound. *International Journal of Computer Assisted Radiology and Surgery*, 7(2):207–215, 2012.

[76] M. Gülsün and Hüseyin Tek. Robust vessel tree modeling. In Dimitris Metaxas, Leon Axel, Gabor Fichtinger, and Gábor Székely, editors, *Medical Image Computing and Computer-Assisted Intervention - MICCAI 2008*, volume 5241 of *Lecture Notes in Computer Science*, pages 602–611. Springer Berlin / Heidelberg, 2008.

[77] Michael G Hennerici and Doris Neuerburg-Heusler. *Vascular diagnosis with ultrasound: clinical references with case studies*, volume 1. Thieme, 2005.

[78] Nicholas J Tustison, Brian B Avants, Philip A Cook, Yuanjie Zheng, Alexander Egan, Paul A Yushkevich, and James C Gee. N4ITK: improved N3 bias correction. *IEEE Transactions on Medical Imaging*, 29(6):1310–1320, 2010.

[79] F. Maes, A. Collignon, D. Vandermeulen, G. Marchal, and P. Suetens. Multimodality image registration by maximization of mutual information. *IEEE Transactions on Medical Imaging*, 16(2):187–198, 1997.

[80] P. Viola and W. M. Wells, III. Alignment by maximization of mutual information. *International Journal of Computer Vision*, 24:137–154, 1997.

[81] A. Roche, X. Pennec, G. Malandain, and N. Ayache. Rigid registration of 3-D ultrasound with MR images: a new approach combining intensity and gradient information. *IEEE Transactions on Medical Imaging*, 20(10):1038–1049, October 2001.

[82] B. Jian and B. C. Vemuri. Robust Point Set Registration Using Gaussian Mixture Models. *IEEE Transactions on Robust Point Set Registration Using Gaussian Mixture Models,*, 33(8):1633–1645, 2011.

[83] H. Chui and A. Rangarajan. A new point matching algorithm for non-rigid registration. *Computer Vision and Image Understanding*, 89(2-3):114–141, 2003.

[84] S. Klein, M. Staring, K. Murphy, M. A. Viergever, and J. P. W. Pluim. elastix: a toolbox for intensity-based medical image registration. *IEEE Transactions on Medical Imaging*, 29(1):196–205, 2010.

[85] S. Klein, J. P. W. Pluim, M. Staring, and M. A. Viergever. Adaptive Stochastic Gradient Descent Optimisation for Image Registration. *International Journal of Computer Vision*, 81:227–239, 2009.

[86] P. Thevenaz and M. Unser. Optimization of mutual information for multiresolution image registration. *IEEE Transactions on Image Processing*, 9(12):2083–2099, 2000.

[87] A. Gee, R. Prager, G. Treece, and L. Berman. Engineering a freehand 3D ultrasound system. *Pattern Recognition Letters*, 24(4-5):757–777, 2003.

[88] Hui Tang, Theo van Walsum, Robbert S van Onkelen, Reinhard Hameeteman, Stefan Klein, Michiel Schaap, Fufa L Tori, Quirijn JA van den Bouwhuijsen, Jacqueline Witteman, Aad van der Lugt, et al. Semiautomatic carotid lumen segmentation for quantification of lumen geometry in multispectral MRI. *Medical Image Analysis*, 16(6):1202–1215, 2012.

[89] L. R. Dice. Measures of the amount of ecologic association between species. *Ecology*, 26(3):pp. 297–302, 1945.

[90] Ronald van't Klooster, Marius Staring, Stefan Klein, Robert M Kwee, M Eline Kooi, Johan HC Reiber, Boudewijn PF Lelieveldt, and Rob J van der Geest. Automated registration of multispectral MR vessel wall images of the carotid artery. *Medical physics*, 40(12):121904, 2013.

[91] R. Lozano, M. Naghavi, K. Foreman, S. Lim, K. Shibuya, V. Aboyans, J. Abraham, T. Adair, R. Aggarwal, S.Y. Ahn, et al. Global and regional mortality from 235 causes of death for 20 age groups in 1990 and 2010: a systematic analysis for the global burden of disease study 2010. *The Lancet*, 380(9859):2095–2128, 2013.

[92] J. Golledge, R.M. Greenhalgh, and A.H. Davies. The symptomatic carotid plaque. *Stroke*, 31(3):774–781, 2000.

[93] M.T.B. Truijman, M.E. Kooi, A.C. Dijk, A.A.J. Rotte, A.G. Kolk, M.I. Liem, F.H.B.M. Schreuder, E. Boersma, W.H. Mess, R.J. Oostenbrugge, et al. Plaque At RISK (PARISK): prospective multicenter study to improve diagnosis of high-risk carotid plaques. *International Journal of Stroke*, 9(6):747–754, 2014.

[94] D.D.B. Carvalho, S. Klein, Z. Akkus, A. C van Dijk, H. Tang, M. Selwaness, A.F.L. Schinkel, J.G. Bosch, A. van der Lugt, and W.J. Niessen. Joint intensity-and-point based registration of free-hand B-mode ultrasound and MRI of the carotid artery. *Medical physics*, 41(5):052904, 2014.

[95] E. Ukwatta, J. Awad, D. Buchanan, G. Parraga, and A. Fenster. Three-dimensional semi-automated segmentation of carotid atherosclerosis from three-dimensional ultrasound images. In *SPIE Medical Imaging*, pages 83150O–83150O. International Society for Optics and Photonics, 2012.

[96] M. Hossain, K. AlMuhanna, L. Zhao, B. Lal, and S. Sikdar. Semiautomatic segmentation of atherosclerotic carotid artery lumen using 3d ultrasound imaging. In *SPIE Medical Imaging*, pages 86694A–86694A. International Society for Optics and Photonics, 2013.

[97] Shubao Liu, Dirk Padfield, and Paulo Mendonca. Tracking of carotid arteries in ultrasound images. In *Medical Image Computing and Computer-Assisted Intervention–MICCAI 2013*, pages 526–533. Springer Berlin Heidelberg, 2013.

[98] A. Arias, D.D.B. Carvalho, J. Petersen, A.C. van Dijk, A. van der Lugt, W.J. Niessen, S. Klein, and M. de Bruijne. Carotid artery lumen segmentation in

3d free-hand ultrasound images using surface graph cuts. In *Medical Image Computing and Computer-Assisted Intervention–MICCAI 2013*, pages 542–549. Springer, 2013.

[99] A. Arias, J. Petersen, A. van Engelen, H. Tang, M. Selwaness, J. CM Witteman, A. van der Lugt, W. Niessen, and M. de Bruijne. Carotid artery wall segmentation by coupled surface graph cuts. In *Medical Computer Vision. Recognition Techniques and Applications in Medical Imaging*, pages 38–47. Springer, 2013.

[100] K. Hameeteman, R. van 't Klooster, M Selwaness, A. van der Lugt, J.C.M. Witteman, W.J. Niessen, and S. Klein. Carotid wall volume quantification from magnetic resonance images using deformable model fitting and learning-based correction of systematic errors. *Physics in Medicine and Biology*, 58, 2013.

[101] D. Rueckert, L.I. Sonoda, C. Hayes, D.L.G. Hill, M.O. Leach, and D.J. Hawkes. Nonrigid registration using free-form deformations: application to breast MR images. *Medical Imaging, IEEE Transactions on*, 18(8):712–721, 1999.

[102] X. Wu and D. Chen. Optimal net surface problems with applications. In Peter Widmayer, Stephan Eidenbenz, Francisco Triguero, Rafael Morales, Ricardo Conejo, and Matthew Hennessy, editors, *Automata, Languages and Programming*, volume 2380 of *Lecture Notes in Computer Science*, pages 775–775. Springer Berlin / Heidelberg, 2002.

[103] H. Ishikawa. Exact optimization for markov random fields with convex priors. *Pattern Analysis and Machine Intelligence, IEEE Transactions on*, 25(10):1333–1336, 2003.

[104] Y. Boykov and V. Kolmogorov. An experimental comparison of min-cut/max-flow algorithms for energy minimization in vision. *IEEE Transactions on Pattern Analysis and Machine Intelligence*, 26(9):1124–1137, 2004.

[105] Jens Petersen, Mads Nielsen, Pechin Lo, Lars Haug Nordenmark, Jesper Holst Pedersen, Mathilde Marie Winkler Wille, Asger Dirksen, and Marleen de Bruijne. Optimal surface segmentation using flow lines to quantify airway abnormalities in chronic obstructive pulmonary disease. *Medical Image Analysis*, 18(3):531–541, 2014.

[106] Morteza Naghavi, Peter Libby, Erling Falk, S Ward Casscells, Silvio Litovsky, John Rumberger, Juan Jose Badimon, Christodoulos Stefanadis, Pedro Moreno, Gerard Pasterkamp, et al. From vulnerable plaque to vulnerable patient a call for new definitions and risk assessment strategies: Part I. *Circulation*, 108(14):1664–1672, 2003.

[107] Luigi Giusto Spagnoli, Alessandro Mauriello, Giuseppe Sangiorgi, Stefano Fratoni, Elena Bonanno, Robert S Schwartz, David G Piepgras, Raimondo Pistolese, Arnaldo Ippoliti, and David R Holmes. Extracranial thrombotically active carotid plaque as a risk factor for ischemic stroke. *JAMA*, 292(15):1845–1852, 2004.

[108] G.L. ten Kate, E.J. Sijbrands, Daniel Staub, B. Coll, F.J. ten Cate, S.B. Feinstein, and A.F.L. Schinkel. Noninvasive imaging of the vulnerable atherosclerotic plaque. *Current Problems in Cardiology*, 35(11):556–591, 2010.

[109] Stijn CH van den Oord, Zeynettin Akkus, Jeanine E Roeters van Lennep, Johan G Bosch, Antonius FW van der Steen, Eric JG Sijbrands, and Arend FL Schinkel. Assessment of subclinical atherosclerosis and intraplaque neovascularization using quantitative contrast-enhanced ultrasound in patients with familial hypercholesterolemia. *Atherosclerosis*, 231(1):107–113, 2013.

[110] Silvia Delsanto, Filippo Molinari, Pierangela Giustetto, William Liboni, Sergio Badalamenti, and Jasjit S Suri. Characterization of a completely user-independent algorithm for carotid artery segmentation in 2-d ultrasound images. *Instrumentation and Measurement, IEEE Transactions on*, 56(4):1265–1274, 2007.

[111] François Destrempes, Jean Meunier, Marie-France Giroux, Gilles Soulez, and Guy Cloutier. Segmentation in ultrasonic B-mode images of healthy carotid arteries using mixtures of Nakagami distributions and stochastic optimization. *Medical Imaging, IEEE Transactions on*, 28(2):215–229, 2009.

[112] Christos P Loizou, Constantinos S Pattichis, Andrew N Nicolaides, and Marios Pantziaris. Manual and automated media and intima thickness measurements of the common carotid artery. *Ultrasonics, Ferroelectrics and Frequency Control, IEEE Transactions on*, 56(5):983–994, 2009.

[113] Fei Mao, Jeremy Gill, Donal Downey, and Aaron Fenster. Segmentation of carotid artery in ultrasound images: Method development and evaluation technique. *Medical Physics*, 27(8):1961–1970, 2000.

[114] Claude B Sirlin, Yueh Z Lee, Michael S Girard, Thomas M Peterson, Gregory C Steinbach, Kristine G Baker, and Robert F Mattrey. Contrast-enhanced B-mode US angiography in the assessment of experimental in vivo and in vitro atherosclerotic disease. *Academic Radiology*, 8(2):162–172, 2001.

[115] Yuko Kono, Sean P Pinnell, Claude B Sirlin, Steven R Sparks, Bassem Georgy, Wade Wong, and Robert F Mattrey. Carotid Arteries: Contrast-enhanced US Angiography - Preliminary Clinical Experience 1. *Radiology*, 230(2):561–568, 2004.

[116] Gerrit L ten Kate, Anouk C van Dijk, Stijn CH van den Oord, Burhan Hussain, Hence JM Verhagen, Eric JG Sijbrands, Antonius FW van der Steen, Aad van der Lugt, and Arend FL Schinkel. Usefulness of contrast-enhanced ultrasound for detection of carotid plaque ulceration in patients with symptomatic carotid atherosclerosis. *The American Journal of Cardiology*, 112(2):292–298, 2013.

[117] Filippo Molinari, Guang Zeng, and Jasjit S Suri. A state of the art review on intima–media thickness (IMT) measurement and wall segmentation techniques for carotid ultrasound. *Computer Methods and Programs in Biomedicine*, 100(3):201–221, 2010.

[118] Vaishali Naik, RS Gamad, and PP Bansod. Carotid artery segmentation in ultrasound images and measurement of intima-media thickness. *BioMed Research International*, 2013, 2013.

[119] Tomas Gustavsson, Quan Liang, Inger Wendelhag, and John Wikstrand. A dynamic programming procedure for automated ultrasonic measurement of the carotid artery. In *Computers in Cardiology 1994*, pages 297–300. IEEE, 1994.

[120] Xiangyang Xu, Yuan Zhou, Xinyao Cheng, Enmin Song, and Guokuan Li. Ultrasound intima–media segmentation using hough transform and dual snake model. *Computerized Medical Imaging and Graphics*, 36(3):248–258, 2012.

[121] François Destrempes, Jean Meunier, Marie-France Giroux, Gilles Soulez, and Guy Cloutier. Segmentation of plaques in sequences of ultrasonic B-mode images of carotid arteries based on motion estimation and a Bayesian model. *Biomedical Engineering, IEEE Transactions on*, 58(8):2202–2211, 2011.

[122] Jacques D Barth, David H Blankenhorn, Emily Wickham, June Y Lai, HP Chin, and Robert H Selzer. Quantitative ultrasound pulsation study in human carotid artery disease. *Arteriosclerosis, Thrombosis, and Vascular Biology*, 8(6):778–781, 1988.

[123] Robert H Selzer, Wendy J Mack, Paul L Lee, Helen Kwong-Fu, and Howard N Hodis. Improved common carotid elasticity and intima-media thickness measurements from computer analysis of sequential ultrasound frames. *Atherosclerosis*, 154(1):185–193, 2001.

[124] Elisa Cuadrado Godia, Rishi Madhok, John Pittman, Samuel Trocio, Romel Ramas, Digna Cabral, Ralph L Sacco, and Tatjana Rundek. Carotid artery distensibility a reliability study. *Journal of Ultrasound in Medicine*, 26(9):1157–1165, 2007.

[125] Nicole M van Popele, Diederick E Grobbee, Michiel L Bots, Roland Asmar, Jirar Topouchian, Robert S Reneman, Arnold PG Hoeks, Deidre AM van der Kuip, Albert Hofman, and Jacqueline CM Witteman. Association between arterial stiffness and atherosclerosis The Rotterdam Study. *Stroke*, 32(2):454–460, 2001.

[126] APG Hoeks, PJ Brands, FAM Smeets, and RS Reneman. Assessment of the distensibility of superficial arteries. *Ultrasound in Medicine & Biology*, 16(2):121–128, 1990.

[127] Alexandra Teynor, Seraina Caviezel, Julia Dratva, Nino Künzli, and Arno Schmidt-Trucksäss. An automated, interactive analysis system for ultrasound sequences of the common carotid artery. *Ultrasound in Medicine & Biology*, 38(8):1440–1450, 2012.

[128] Spyretta Golemati, Antonio Sassano, M John Lever, Anil A Bharath, Surinder Dhanjil, and Andrew N Nicolaides. Carotid artery wall motion estimated from B-mode ultrasound using region tracking and block matching. *Ultrasound in Medicine & Biology*, 29(3):387–399, 2003.

[129] KL Chan. Two approaches to motion analysis of the ultrasound image sequence of carotid atheromatous plaque. *Ultrasonics*, 31(2):117–123, 1993.

[130] Zeynettin Akkus and Kumar V Ramnarine. Dynamic assessment of carotid plaque motion. *Ultrasound*, 18(3):140–147, 2010.

[131] Z. Akkus, A. Hoogi, G. Renaud, L. Gerrit, S.C.H. van den Oord, A.F.L. Schinkel, N. de Jong, A.F.W. van der Steen, and J.G. Bosch. Motion compensation method using dynamic programming for quantification of neovascularization in carotid atherosclerotic plaques with contrast enhanced ultrasound (CEUS). In *SPIE Medical Imaging*, pages 83200C–83200C. International Society for Optics and Photonics, 2012.

[132] G.L. ten Kate, G.G.J. Renaud, Z. Akkus, S.C.H. van den Oord, F.J. ten Cate, V. Shamdasani, R.R. Entrekin, E.J.G. Sijbrands, N. de Jong, J.G.s Bosch, et al. Far-wall pseudoenhancement during contrast-enhanced ultrasound of the carotid arteries: Clinical description and in vitro reproduction. *Ultrasound in Medicine & Biology*, 38(4):593–600, 2012.

[133] CT Metz, Stefan Klein, Michiel Schaap, Theo van Walsum, and Wiro J Niessen. Nonrigid registration of dynamic medical imaging data using nD+t B-splines and a groupwise optimization approach. *Medical Image Analysis*, 15(2):238–249, 2011.

[134] Stefan Klein, Josien PW Pluim, Marius Staring, and Max A Viergever. Adaptive stochastic gradient descent optimisation for image registration. *International Journal of Computer Vision*, 81(3):227–239, 2009.

[135] Shelly T Nevo, Marijn Van Stralen, Albert M Vossepoel, Johan HC Reiber, Nico de Jong, Antonius FW van der Steen, and Johan G Bosch. Automated tracking of the mitral valve annulus motion in apical echocardiographic images using multidimensional dynamic programming. *Ultrasound in Medicine & Biology*, 33(9):1389–1399, 2007.

[136] Guillaume Zahnd, Maciej Orkisz, André Sérusclat, Philippe Moulin, and Didier Vray. Simultaneous extraction of carotid artery intima-media interfaces in ultrasound images: assessment of wall thickness temporal variation during the cardiac cycle. *International Journal of Computer Assisted Radiology and Surgery*, 9(4):645–658, 2014.

[137] Z. Akkus, J.G. Bosch, G.V. Sánchez-Ferrero, D.D.B. Carvalho, G. Renaud, S.C.H. van den Oord, L. Gerrit, A. FL Schinkel, N. de Jong, and A.F.W. van der Steen. Statistical segmentation of carotid plaque neovascularization. In *SPIE Medical Imaging*, pages 867506–867506. International Society for Optics and Photonics, 2013.

[138] Todd K Moon. The expectation-maximization algorithm. *Signal Processing Magazine, IEEE*, 13(6):47–60, 1996.

[139] Guillaume Zahnd, Didier Vray, André Sérusclat, Djhianne Alibay, Mark Bartold, Alex Brown, Marion Durand, Lisa M Jamieson, Kostas Kapellas, Louise J Maple-Brown, et al. Longitudinal displacement of the carotid wall and cardiovascular risk factors: associations with aging, adiposity, blood pressure and periodontal disease independent of cross-sectional distensibility and intima-media thickness. *Ultrasound in Medicine & Biology*, 38(10):1705–1715, 2012.

[140] James H Stein, Claudia E Korcarz, R Todd Hurst, Eva Lonn, Christopher B Kendall, Emile R Mohler, Samer S Najjar, Christopher M Rembold, and Wendy S Post. Use of carotid ultrasound to identify subclinical vascular disease and evaluate cardiovascular disease risk: A consensus statement from the american society of echocardiography carotid intima-media thickness task force endorsed by the society for vascular medicine. *Journal of the American Society of Echocardiography*, 21(2):93–111, 2008.

[141] Charles Warlow. Mrc european carotid surgery trial: interim results for symptomatic patients with severe (70-99%) or with mild (0-29%) carotid stenosis. *The Lancet*, 337(8752):1235–1243, 1991.

[142] Brian A Haluska, Leanne Jeffriess, Phillip M Mottram, Stephane G Carlier, and Thomas H Marwick. A new technique for assessing arterial pressure wave forms and central pressure with tissue doppler. *Cardiovascular Ultrasound*, 5(1):6, 2007.

[143] Graf, L Bortolin, A Pascaner, and D Craiem. Comparison of central systolic pressure estimates obtained from ultrasound images and applanation tonometry. *Journal of Physics: Conference Series*, 477(1):012–034, 2013.

[144] Mary J Roman, Richard B Devereux, Jorge R Kizer, Elisa T Lee, James M Galloway, Tauqeer Ali, Jason G Umans, and Barbara V Howard. Central pressure more strongly relates to vascular disease and outcome than does brachial pressure the strong heart study. *Hypertension*, 50(1):197–203, 2007.

[145] W. E Hellings, W. Peeters, F.L. Moll, S.R.D. Piers, J. van Setten, P.J. Van der Spek, J.P.M. de Vries, K. A Seldenrijk, P.C. De Bruin, A. Vink, et al. Composition of carotid atherosclerotic plaque is associated with cardiovascular outcome a prognostic study. *Circulation*, 121(17):1941–1950, 2010.

[146] Johannes A Schaar, James E Muller, Erling Falk, Renu Virmani, Valentin Fuster, Patrick W Serruys, Antonio Colombo, Christodoulos Stefanadis, S Ward Casscells, Pedro R Moreno, et al. Terminology for high-risk and vulnerable coronary artery plaques. *European heart journal*, 25(12):1077–1082, 2004.

[147] Falak Shah, Prakash Balan, Matthew Weinberg, Vijaya Reddy, Rachel Neems, Matthew Feinstein, John Dainauskas, Peter Meyer, Marshall Goldin, and Steven B Feinstein. Contrast-enhanced ultrasound imaging of atherosclerotic

carotid plaque neovascularization: a new surrogate marker of atherosclerosis? *Vascular Medicine*, 12(4):291–297, 2007.

[148] Christos P Loizou, Constantinos S Pattichis, Marios Pantziaris, and Andrew Nicolaides. An integrated system for the segmentation of atherosclerotic carotid plaque. *Information Technology in Biomedicine, IEEE Transactions on*, 11(6):661–667, 2007.

[149] CP Loizou, S Petroudi, CS Pattichis, M Pantziaris, T Kasparis, and A Nicolaides. Segmentation of atherosclerotic carotid plaque in ultrasound video. In *Engineering in Medicine and Biology Society (EMBC), 2012 Annual International Conference of the IEEE*, pages 53–56. IEEE, 2012.

[150] Andrew N Nicolaides, Stavros K Kakkos, Maura Griffin, Michael Sabetai, Surinder Dhanjil, Daffyd J Thomas, George Geroulakos, Niki Georgiou, Susan Francis, Elena Ioannidou, et al. Effect of image normalization on carotid plaque classification and the risk of ipsilateral hemispheric ischemic events: results from the asymptomatic carotid stenosis and risk of stroke study. *Vascular*, 13(4):211–221, 2005.

[151] Zeynettin Akkus, Assaf Hoogi, Guillaume Renaud, Stijn CH van den Oord, L Gerrit, Arend FL Schinkel, Dan Adam, Nico de Jong, Antonius FW van der Steen, and Johan G Bosch. New quantification methods for carotid intra-plaque neovascularization using contrast-enhanced ultrasound. *Ultrasound in medicine & biology*, 40(1):25–36, 2014.

[152] Assaf Hoogi, Zeynettin Akkus, Stijn CH van den Oord, L Gerrit, Arend FL Schinkel, Johan G Bosch, Nico de Jong, Dan Adam, and Antonius FW van der Steen. Quantitative analysis of ultrasound contrast flow behavior in carotid plaque neovasculature. *Ultrasound in medicine & biology*, 38(12):2072–2083, 2012.

[153] Pin-tong Huang, Fu-guang Huang, Chun-peng Zou, Hai-yan Sun, Xin-qiao Tian, Yan Yang, Ji-fei Tang, Peng-lin Yang, and Xiao-tong Wang. Contrast-enhanced sonographic characteristics of neovascularization in carotid atherosclerotic plaques. *Journal of Clinical Ultrasound*, 36(6):346–351, 2008.

[154] Li Xiong, You-Bin Deng, Ying Zhu, Ya-Ni Liu, and Xiao-Jun Bi. Correlation of Carotid Plaque Neovascularization Detected by Using Contrast-enhanced US with Clinical Symptoms. *Radiology*, 251(2):583–589, 2009.

[155] Assaf Hoogi, Dan Adam, Aaron Hoffman, Hedviga Kerner, Shimon Reisner, and Diana Gaitini. Carotid plaque vulnerability: quantification of neovascularization on contrast-enhanced ultrasound with histopathologic correlation. *American Journal of Roentgenology*, 196(2):431–436, 2011.

[156] Filippo Molinari, Guang Zeng, and Jasjit S Suri. An integrated approach to computer-based automated tracing and its validation for 200 common carotid arterial wall ultrasound images a new technique. *Journal of Ultrasound in Medicine*, 29(3):399–418, 2010.

[157] Qi Zhang, Lijing Yang, Chaolun Li, and Wenping Wang. Contrast-enhanced ultrasound image segmentation of atherosclerotic plaques using spatial-temporal analysis and snakes. In *Systems and Informatics (ICSAI), 2012 International Conference on*, pages 1901–1905. IEEE, 2012.

[158] Qi Zhang, Chaolun Li, Hong Han, Lijing Yang, Yuanyuan Wang, and Wenping Wang. Computer-aided quantification of contrast agent spatial distribution within atherosclerotic plaque in contrast-enhanced ultrasound image sequences. *Biomedical Signal Processing and Control*, 13:50–61, 2014.

[159] Quan Liang, Inger Wendelhag, John Wikstrand, and Tomas Gustavsson. A multiscale dynamic programming procedure for boundary detection in ultrasonic artery images. *Medical Imaging, IEEE Transactions on*, 19(2):127–142, 2000.

[160] Da-Chuan Cheng and Xiaoyi Jiang. Detections of arterial wall in sonographic artery images using dual dynamic programming. *Information Technology in Biomedicine, IEEE Transactions on*, 12(6):792–799, 2008.

[161] Yuan Zhou, Xinyao Cheng, Xiangyang Xu, and Enmin Song. Dynamic programming in parallel boundary detection with application to ultrasound intima-media segmentation. *Medical image analysis*, 17(8):892–906, 2013.

[162] Rui Rocha, Jorge Silva, and Aurélio Campilho. Automatic detection of the carotid lumen axis in b-mode ultrasound images. *Computer Methods and Programs in Biomedicine*, 2014.

[163] D.D.B. Carvalho, Z. Akkus, J.G. Bosch, S.C.H. van den Oord, W.J. Niessen, and S. Klein. Nonrigid motion compensation in B-mode and contrast enhanced ultrasound image sequences of the carotid artery. In *SPIE Medical Imaging*, pages 90340N–90340N. International Society for Optics and Photonics, 2014.

[164] Zeynettin Akkus, Diego DB Carvalho, Stefan Klein, Stijn CH van den Oord, Arend FL Schinkel, Nico de Jong, Antonius FW van der Steen, and Johan G Bosch. Atherosclerotic carotid lumen segmentation in combined B-mode and contrast enhanced ultrasound images. In *SPIE Medical Imaging*, pages 903445–903445. International Society for Optics and Photonics, 2014.

[165] P-J Touboul, MG Hennerici, S Meairs, H Adams, P Amarenco, N Bornstein, L Csiba, M Desvarieux, S Ebrahim, M Fatar, et al. Mannheim carotid intima-media thickness consensus (2004–2006). *Cerebrovascular Diseases*, 23(1):75–80, 2006.

[166] Michael R Skilton, Loic Boussel, Fabrice Bonnet, Sophie Bernard, Philippe Charles Douek, Philippe Moulin, and André Serusclat. Carotid intima–media and adventitial thickening: Comparison of new and established ultrasound and magnetic resonance imaging techniques. *Atherosclerosis*, 215(2):405–410, 2011.

[167] Daniel H O'Leary and Michiel L Bots. Imaging of atherosclerosis: carotid intima–media thickness. *European heart journal*, 31(14):1682–1689, 2010.

[168] Wei Sun, Wiro J Niessen, and Stefan Klein. Free-form deformation using lower-order b-spline for nonrigid image registration. In *Medical Image Computing and Computer-Assisted Intervention–MICCAI 2014*, pages 194–201. Springer, 2014.

[169] Chun Yuan, Lee M Mitsumori, Kirk W Beach, and Kenneth R Maravilla. Carotid Atherosclerotic Plaque: Noninvasive MR Characterization and Identification of Vulnerable Lesions. *Radiology*, 221(2):285–299, 2001.

[170] Bram F Coolen, Dirk HJ Poot, Madieke I Liem, Loek P Smits, Shan Gao, Gyula Kotek, Stefan Klein, and Aart J Nederveen. Three-dimensional quantitative T1 and T2 mapping of the carotid artery: Sequence design and in vivo feasibility. *Magnetic Resonance in Medicine*, 2015.

[171] A. van Engelen, W.J. Niessen, S. Klein, H.C. Groen, H.J.M. Verhagen, J.J. Wentzel, A. van der Lugt, and M. de Bruijne. Multi-feature-based plaque characterization in ex vivo MRI trained by registration to 3D histology. *Physics in Medicine and Biology*, 57:241–256, 1 2012.

[172] Rasmus S Ripa, Andreas Knudsen, Anne Mette F Hag, Anne-Mette Lebech, Annika Loft, Sune H Keller, Adam E Hansen, Eric von Benzon, Liselotte Højgaard, and Andreas Kjær. Feasibility of simultaneous pet/mr of the carotid artery: first clinical experience and comparison to pet/ct. *American journal of nuclear medicine and molecular imaging*, 3(4):361, 2013.

[173] Khalid AlMuhanna, Md Murad Hossain, Limin Zhao, Jonathan Fischell, Gregory Kowalewski, Moira Dux, Siddhartha Sikdar, and Brajesh K Lal. Carotid plaque morphometric assessment with three-dimensional ultrasound imaging. *Journal of vascular surgery*, 61(3):690–697, 2015.

[174] Lysa Legault Kingstone, Wael Shabana, Rebecca Thornhill, Megan White, Joanna Lam, and Geoff Currie. Comparison and accuracy of carotid plaque analysis between two-and three-dimensional ultrasound imaging. *Journal of Diagnostic Medical Sonography*, page 8756479314531853, 2014.

PhD Portfolio

PhD period:	2010-2015
Departments:	Radiology & Medical Informatics
Research schools:	ASCI, NIHES

In-depth Courses

Advanced Pattern Recognition (ASCI): 2010
Advanced Morphological Filters (ASCI): 2010
Measuring Features (ASCI): 2011
Presentation Course (Department of Medical Informatics): 2011
Biomedical English Writing and Communication (Erasmus MC) : 2011
Front-End Vision & Multi-Scale Image Analysis (ASCI): 2012
Knowledge Driven Image Segmentation (ASCI): 2012
Principles of Research in Epidemiology (NIHES): 2012
Dutch Courses (Erasmus MC)
- Level A2 2011
- Level B1 2012

International Conferences

SPIE Medical Imaging
San Diego, USA, (oral and poster presentation) 2014
Workshop in Biomedical Image Registration (WBIR)
Nashville, USA, (poster presentation) 2012
European Congress of Radiology
Vienna, Austria, (attendance - help in workshop organization) 2011
International Symposium on Biomedical Imaging (ISBI) 2010
Rotterdam, the Netherlands, (attendance - help in organization)

Other presentations

COEUR PhD day
Rotterdam, the Netherlands 2011
Dutch BME Conference
Egmond aan Zee, the Netherlands 2011
COEUR PhD day
Rotterdam, the Netherlands 2012
Several CTMM Annual Meetings (poster)
Utrecht, the Netherlands 2010-2013
Several Semi-annual Parisk meetings (oral/poster) 2010-2013
BIGR Seminar (2x) 2011-2013
Medical Informatics Research Lunch (2x) 2010-2013
Internal BIGR Vascular Image Processing Meetings 2010-2014
BIGR-LUMC Image Registration Meetings 2013-2014

Publications

Journal Publications

- D.D.B. Carvalho*, Z. Akkus*, S.C.H. van den Oord, A.F.L. Schinkel, A.F.W. van der Steen, W.J. Niessen, J.G. Bosch and S. Klein, "Lumen Segmentation and Motion Estimation in B-mode and Contrast-Enhanced Ultrasound Images of the Carotid Artery in Patients with Atherosclerotic Plaque", *IEEE Transactions on Medical Imaging*, 34.4 (2015): 983-993.
  *both authors contributed equally to this research

- Z. Akkus*, D.D.B. Carvalho*, S.C.H. van den Oord, A.F.L. Schinkel, W.J. Niessen, N. de Jong, A.F.W. van der Steen, S. Klein and J.G. Bosch, "Fully Automated Carotid Plaque Segmentation in Combined Contrast Enhanced and B-mode Ultrasound", *Ultrasound in Medicine and Biology*, 2015 - 41 (2), 517-531.
  *both authors contributed equally to this research

- Diego D.B. Carvalho*, Andrés M.A. Lorza*, Wiro J. Niessen, Marleen de Bruijne, Stefan Klein, "Automated Registration of Free-hand B-mode Ultrasound and MRI of the Carotid Arteries Based on Geometrical Features", submitted
  *both authors contributed equally to this research

- D.D.B. Carvalho, S. Klein, Z. Akkus, A.C. van Dijk, H. Tang, M Selwaness, A.F.L. Schinkel, J.G. Bosch, A. van der Lugt and W.J. Niessen, "Joint Intensity-and-Point Based Registration of Free-hand B-Mode Ultrasound and MRI of the Carotid Artery", *Medical Physics*, 2014 - 41 (5), 052904

- D.D.B. Carvalho, S. Klein, Z. Akkus, G. L. ten Kate, A.F.L. Schinkel, J.G. Bosch, A van der Lugt and W.J. Niessen, "Estimating 3D Lumen Centerlines of Carotid Arteries in Free-hand Acquisition Ultrasound", *International Journal of Computer Assisted Radiology and Surgery,* 7.2 (2012): 207-215.

Conference Papers

- Z. Akkus, N. de Jong, A.F.W. van der Steen, J.G. Bosch, S.C.H. van den Oord, A.F.L. Schinkel, D.D.B. Carvalho, W.J. Niessen and S. Klein, "Fully automated carotid plaque segmentation in combined B-mode and contrast enhanced ultrasound", *Ultrasonics Symposium (IUS), 2014 IEEE International*, 2014 - 911-914

- Z. Akkus, D.D.B. Carvalho, S. Klein, S.C.H. van den Oord, A.F.L. Schinkel, N. de Jong, A.F.W. van der Steen and J.G. Bosch, "Atherosclerotic carotid lumen segmentation in combined B-mode and contrast enhanced ultrasound images", *Proc. SPIE 9034, Medical Imaging 2014: Image Processing* , 2014 - 903445-903445-9

- D.D.B. Carvalho, Z. Akkus, J.G. Bosch, S.C.H. van den Oord, W.J. Niessen and S. Klein, "Nonrigid motion compensation in B-mode and contrast enhanced ultrasound image sequences of the carotid artery", *Proc. SPIE 9034, Medical Imaging 2014: Image Processing*, 2014 - 90340N-90340N-7

- A. Arias Lorza, D.D.B. Carvalho, J. Petersen, A.C. van Dijk, A. van der Lugt, W.J. Niessen, S. Klein and M. de Bruijne, "Carotid artery lumen segmentation in 3D free-hand ultrasound images using surface graph cuts", *MICCAI 2013*, 2013 - 542-549

- Z. Akkus, J.G. Bosch, G.V. Sánchez-Ferrero, D.D.B. Carvalho, G. Renaud, A.F.L. Schinkel, N. de Jong and A.F.W. van der Steen, "Statistical segmentation of carotid plaque neovascularization", *SPIE Medical Imaging*, 2013 - 867506-867506-12

- D.D.B. Carvalho, S. Klein, Z. Akkus, G. L. ten Kate, H. Tang, M Selwaness, A.F.L. Schinkel, J.G. Bosch, A. van der Lugt and W.J. Niessen, "Registration of Free-Hand Ultrasound and MRI of Carotid Arteries through Combination of Point-Based and Intensity-Based Algorithms", *Biomedical Image Registration, 2012* - 131-140

Conference Abstracts

- D.D.B. Carvalho, S. Klein, Q.J.A. van den Bouwhuijsen, A. van der Lugt and W.J. Niessen, "Registration of MRI and US images in cardiovascular imaging", 3rd Dutch conference on Biomedical Engineering, 2011

Acknowledgements

In 2010, I came to the Netherlands to pursue a PhD. This step was only possible due to the support I had received up to this point. At first, I would like to thank my family. My mother and father did not have the opportunity to go to a university as I had. I will be forever grateful that they made an enormous effort granting me not only the chance to study, but mainly, the will to achieve it. This achievement also belongs to them.

Additionally, I would like to thank Prof. Aldo von Wangenheim. After I completed my bachelor degree in Brazil, I had the opportunity to work with Aldo in the Cyclops group at UFSC. Aldo has a broad vision of topics and always instigates his students to go beyond their expectations. I am glad that more and more students from Cyclops are being granted with scholarships to study abroad, and that the group continues providing important telemedicine services to the public health system of Brazil.

Back to 2010. I was very fortunate to join BIGR and to work in the Project Parisk. I would like to thank Prof. Wiro Niessen for kindly accepting me in the group. BIGR has a nice working environment joining together people from all over the world. Wiro has proved his great talent in managing the group, leading to a constant exchange of knowledge between the"BIGR people" and other colleagues from Erasmus MC. Wiro, your guidance during my PhD helped me to plan ahead what would be the next topic to address. Our meetings were extremely useful to define the big picture. In a multi-disciplinary research with many tasks occuring in parallel, this planning was essential to keep the objectives on track.

Stefan, thank you for accepting to be my supervisor. We had many meetings during these past five years, searching for solutions for tracking, registration, or segmentation problems among other challenges. All these very fruitful discussions led to the development of this thesis. Your tenacity, creativity and time availability of working after hours impressed me. You always put a big effort in expressing your opinion about any question, simple or complex. More important than spending your time on it, your commitment reflects the respect for your students and the perseverance

of your work. It was a pleasure working with you. I was the first PhD student you supervised, and I foresee that you have a very promising career ahead. With your potential, you can keep inspiring more people for a long time.
Working in the Parisk project was a big challenge and good chance to learn from experts of diverse fields. During the project, I had the collaboration of many colleagues at Erasmus MC to complete this thesis.
I would like to thank my colleagues from the radiology and cardiology departments: Aad, Anouk, Arend, Mariana, Luit and Stijn. The data acquisition was a crucial part of this thesis, particularly the Ultrasound acquisition with the Flock of Birds (magnetic sensor). It took some attempts to develop a time-efficient acquisition protocol; I am pleased I could count on your help.
I also worked closely with Zeynettin and Hans from the Biomedical Engineering department. Their contribution to the first part of this thesis was essential to overcome the technical problems in calibrating the Flock of Birds. The second part of this thesis was entirely based on two works developed with their cooperation. I would like to thank them both for their determination and persistence in working on such difficult challenges.
During my defense, I will have the presence of my fellow Latin American colleagues as paranymphs. Andrés was my office mate at BIGR. Thanks to daily talks on our research (among other things) and due to overlapping research topics, we started working on a side project that became the third chapter of this thesis. I didn't write any paper with Gerardo, but we had many conversations these years about economics, politics, history and whatever else was happening in the world. I am glad that you both will be next to me during my defense.
In BIGR we have frequent meetings with colleagues that are working on a similar research topic. Generally, these meetings were the first time that ideas or concepts are presented to an audience. The discussion and questions that arose in these meetings were the first "peer review" of an ongoing work and helped to improve it or to make a path correction. I would like to thank all the colleagues that I had contact with in the vascular meetings (R-Vip): Adriënne, Arna, Azadeh, Henk, Hui, Marleen, Reinhard, Ronald, Ruben, Shan and Theo; and in the registration meetings (RAMBO): Jean-Marie, Marius, Yuchuan, Wyke and Wei.
I would like also to thank many of my colleagues from BIGR and the Medical Informatics department which I met during my PhD: Adria, Annegreet, Carolyn, Coert, Daniel, Dirk, Emilie, Erwin, Esben, Esther, Eugene, Fedde, Gijs, Guillaume, Hakim, Hortense, Hua, Ihor, Jyotirmoy, Lejla, Luu, Marcel, Marius, Michiel, Miroslav, Noemí, Nora, Oleh, Osemeke, Pierre, Rahil, René, Renske and Valerio. I had a great time with you going to dinners, concerts, movie nights, jam sessions and the BIGR outings. About BIGR outings, I would also to thank Johan for the help he gave me in Giethoorn.
Despite the fact I left UFSC a long time ago, I am still connected with some friends. After all this time, we still could keep periodical talks to share our life events or try meet live once a year: Alexandre, Anderson, Antonio, Cristiano, Daniel, Darlan, Diego, Eduardo, Fernando, Jean, Maycon, Raphael, Ronan, Simon and Vinicius.
Of course, I missed a lot of things from my country by living abroad. But on the present time, I am more focused on the aspects that I miss in Brazil, than the aspects

I miss from Brazil. Coming to the Netherlands was a life changing experience. I could see the effects of an organized society, interested in the continuous improvement of the quality of life of the citizens.

After the end of my working contract at Erasmus MC, I started working at Fugro Intersite. I am very glad that I have been working with a great team that helped me to adapt to the R&D environment outside academia. It has been very rewarding participating in a group effort which has led to the development of successful products worldwide.

I would also like to thank Sine. We have been in the busiest times of our careers since we had met, but you always did your best to support me. Your presence granted me the emotional stability to keep moving forward in the moments I needed the most.

Completing a PhD thesis is a journey in which some obstacles cannot be predicted and the time to overcome them can be barely estimated. Time is the most valuable thing in life, and how we invest it is up to ourselves. I would like to dedicate this thesis to the memory of my uncle Juvenal Dias, who passed away last year. His generosity was expressed in the time he took to encourage people to surpass their self imposed limitations.

About the author

Diego Dias Bispo Carvalho was born in Curitiba - Brazil in 1982. He completed his bachelor degree in Computer Sciences at UFSC (Florianópolis - Brazil) in 2005.
From 2005 to 2007 he worked on his master thesis at LAPIX - Image Processing and Computer Graphics Laboratory also at UFSC. The topic of his thesis was the to develop a methodology to graphically simulate the deformation of soft tissues in real time. From 2007 to March 2010, Diego worked as the supervisor of the Computer Graphics Laboratory. From June 2009 to February 2010, he also worked as lecturer in the Gaming Development Tech-course at Univali (Florianópolis - Brazil).
In April 2010, he started his PhD studies at the BIGR - Biomedical Imaging Group (Rotterdam - the Netherlands). The objective of his research was to developed methodologies to establish correlations between different medical imaging modalities used to inspect the carotid artery, allowing an improved analysis of carotid arteries in patients with atherosclerosis. The result of this work is described in this thesis.
Since April 2014 he works as a computer vision R&D engineer at Fugro Intersite (Leidscheendam - the Netherlands). His activities are to develop and validate computer vision algorithms used to inspect and position offshore structures.